Technical Report
TR-21-08
December 2022

Evaluation of the permafrost models used in the SR-Site and SR-PSU safety assessments against Greenland GAP-site bedrock temperatures

Juha Hartikainen
Jens-Ove Näslund
Johan Liakka
Lillemor Claesson Liljedahl
Pauli Kolisoja
Reijo Kouhia

SVENSK KÄRNBRÄNSLEHANTERING AB

SWEDISH NUCLEAR FUEL
AND WASTE MANAGEMENT CO

Box 3091, SE-169 03 Solna
Phone +46 8 459 84 00
skb.se

ISSN 1404-0344
SKB TR-21-08
ID 1970978

December 2022

Evaluation of the permafrost models used in the SR-Site and SR-PSU safety assessments against Greenland GAP-site bedrock temperatures

Juha Hartikainen[1], Jens-Ove Näslund[2], Johan Liakka[2],
Lillemor Claesson Liljedahl[2,3], Pauli Kolisoja[1], Reijo Kouhia[1]

1 Tampere University
2 Swedish Nuclear Fuel and Waste Management Company (SKB)
3 DHI Sweden

Keywords: Permafrost model, Evaluation, GAP, SR-Site, SR-PSU, Greenland, Climate.

Preface

This report describes a study aiming at evaluating a numerical permafrost model previously used in SKB safety assessments for the Forsmark site. The evaluation was performed for the site of the Greenland Analogue Project (GAP) in western Greenland. Present-day bedrock temperatures and permafrost depths were simulated along a 15 km profile for a number of cases based on a large array of input data on e.g. palaeoclimate and environmental conditions, and their estimated uncertainties. The simulated, palaeoclimatically corrected, bedrock temperatures were subsequently compared and evaluated against detailed bedrock temperatures measured in a 650 m deep bedrock borehole located at the ice-sheet margin. At the location where the 2D model domain crosses the bedrock borehole, the permafrost thickness is around 350 metres at present.

The results from the model evaluation are relevant for the assessments of long-term repository safety for the planned spent nuclear fuel repository at Forsmark, the existing repository for short-lived low- and intermediate-level waste at Forsmark (SFR), and the planned repository for long-lived low-level waste (SFL). As such, the results from the model evaluation will be used to assess the conclusions drawn from the previous safety assessment permafrost model simulations made for Forsmark.

The study was conducted by Juha Hartikainen (Tampere university), Jens-Ove Näslund (SKB), Johan Liakka (SKB) and Lillemor Claesson Liljedahl (DHI/SKB).

The report manuscript was scientifically reviewed by Dr. Denis Cohen (Dept. of Earth and Environmental Science, New Mexico Institute of Mining and Technology, U.S.), Dr. William Colgan (Geological Survey of Denmark and Greenland, Copenhagen, Denmark), and Dr. Ralf Greve (Institute of Low Temperature Science, Hokkaido University, Japan).

Stockholm, December 2022

Jens-Ove Näslund
Coordinator Climate Research Programme SKB

Abstract

Two versions of a numerical permafrost model were evaluated against measured bedrock temperature data from a 650 m deep bedrock borehole situated at the ice-sheet margin in western Greenland. Model A (without thermal offset) has previously been used in the safety assessments for the spent nuclear fuel repository, whereas Model B (with thermal offset) has been used for the repository for low- and intermediate-level waste (SFR). The permafrost model has in these studies been used for simulations of bedrock temperatures and permafrost development for past and future cold climate periods at the Forsmark site in Sweden with the overall aim to assess post-closure safety for the two repositories.

In the present study, the simulations were made for the Greenland site for the last glacial cycle (from 104 000 years before present up to present-day). The permafrost model was evaluated by comparing the simulated present-day bedrock temperatures with the measured ones. A large number of different input data were used in the permafrost model simulations, originating from different types of measurements made within the study area, other model simulations, interpretations of aerial photographs, and compilations of data from the literature. A large number of sensitivity simulations were carried out to study the effects of these uncertainties.

Taking all identified uncertainties in input data into account, the permafrost model predicted the present-day bedrock temperature for a full 400-metre depth interval (91–491 m below the ground surface) to be within the range −1.4 and +1.6 °C for Model A and −2.2 and +1.3 °C for Model B compared with the observed bedrock temperatures. These uncertainty ranges encompass both input data uncertainties and intrinsic model errors. However, the fact that the uncertainty ranges in the simulated temperature is nearly centred around the measured temperature indicates that any systematic intrinsic model error is small. The results of this model evaluation will, in future safety assessments for the spent nuclear fuel repository and SFR, be used to assess conclusions drawn from results obtained by these two versions of the permafrost model.

Sammanfattning

Två versioner av en numerisk permafrostmodell har utvärderats mot observerade temperaturer från ett 650 m djup bergborrhål beläget vid inlandsisens kant på västra Grönland. Modell A (utan termisk offset) har tidigare använts i säkerhetsanalyser för kärnbränsleförvaret medan Modell B (med termisk offset) har använts för förvaret för låg- och medelaktivt avfall (SFR). Permafrostmodellen har i dessa arbeten använts för simuleringar av berggrundstemperaturer och tillväxt av permafrost för historiska och framtida kalla klimatperioder för Forsmarksplatsen i Sverige med det övergripande målet att bedöma säkerhet efter förslutning för de två förvaren.

I den föreliggande studien har simuleringar gjorts för Grönlandsplatsen för den senaste glaciationscykeln (för perioden från 104 000 år före nu till nutid). Permafrostmodellen utvärderades genom att jämföra simulerade temperaturer i berget mot observerade temperaturer. För studieområdet sammanställdes först en mängd indata för egenskaper hos berg, grundvatten och ytparametrar, inklusive sammanställning av data från litteraturen och från andra modellsimuleringar, vilka sedan användes i simuleringarna av mark- och bergtemperaturer och permafrost/frysdjup. Ett stort antal simuleringar genomfördes för att undersöka känsligheten för osäkerheter i indata och för att studera effekterna av dessa.

Med hänsyn till alla identifierade osäkerheter i indata, predikterade de två versionerna av permafrostmodellen temperaturen i berggrunden över ett 400-meters djupintervall (91–491 m under markytan) att ligga inom intervallet −1,4 till +1,6 °C för Modell A och −2,2 till +1,3 °C för Modell B jämfört med observerade temperaturer. De respektive osäkerhetsintervallen härrör både från osäkerheter i indata och från systematiska modellfel. Det faktum att osäkerheten av den beräknade temperaturen nästan är centrerad kring de uppmätta temperaturerna tyder dock på att de systematiskt inneboende modellfelen är små. Resultaten från denna modellutvärdering kommer att användas för att utvärdera antaganden och slutsatser som tidigare dragits i säkerhetsanalyser, samt kommer dras i framtida säkerhetsanalyser, för kärnbränsleförvaret och SFR för att utvärdera deras säkerhet efter förslutning.

Contents

1 Introduction

Geological repositories for radioactive waste need to be safe to humans and the environment for very long time periods into the future. The safety assessments performed for the planned spent nuclear fuel repository (hereafter denoted SFK) at Forsmark, Sweden, cover a time span of 1 million years, whereas the safety assessments for the existing repository for low- and intermediate-level waste (SFR), also located at Forsmark, cover 100 000 years. Over these vast timescales, the climate at the repository site may vary considerably, from temperate climates with warmer conditions than today, to cold periods with full glacial conditions. Furthermore, periglacial climate conditions may develop at the repository site during times of cold and dry climate, including periods with ice-sheets present elsewhere in Scandinavia. The cold and dry climates during periglacial periods typically lead to the development of permafrost and perennially frozen ground. The permafrost is defined solely by the 0 °C isotherm, whereas the perennially frozen ground depends on the thermo-hydro-chemical state of groundwater and physicochemical properties of rock and soil. The freezing of groundwater, and thereby the amount of perennially frozen ground decreases with increasing groundwater pressure and salinity concentration. In addition, the cooling of the bedrock to sub-freezing temperatures affects a number of processes that may be of importance for post-closure repository safety: i) when (portions of) the groundwater freezes, the groundwater flow pattern is drastically changed since frozen conditions restricts groundwater flow, ii) the groundwater freezing process may result in freeze-out of salts which increases the salinity of the groundwater below the freezing-front, iii) if low enough temperatures were to reach the SFK repository located at an approximate depth of 450 m, a frozen buffer clay and backfill material in the deposition tunnels may start to have detrimental effects on the KBS-3 canister and surrounding host rock respectively, and iv) albeit unlikely, permafrost and frozen conditions within the coming 100 ka could also deteriorate the concrete structures of the SFR repository, with its shallowest parts situated 60 m below the ground surface, hence affecting their permeability.

In the safety assessments for SFK and SFR, numerical 2D permafrost modelling has been used to assess the development of permafrost and bedrock temperatures for different future scenarios that include periods of cold climate conditions (Hartikainen at al. 2010, Brandefelt et al. 2013). The model used for the SFR safety assessment (in the present study denoted Model B) constituted an updated version of the model used for SFK (here denoted Model A), see Brandefelt et al. (2013). The simulations used a large array of site-specific information on surface, bedrock and groundwater characteristics obtained from the Forsmark site investigation programme and from the SKB climate research programme. A large number of sensitivity simulations were performed to account for the uncertainties in input data (Hartikainen et al. 2010).

The main result from the permafrost simulations for SFK is that permafrost depths during typical glacial cycle conditions may reach depth of around 260 m, whereas associated perennially frozen ground depths are around 10 m shallower. When studying maximum possible freezing depths at Forsmark under severe periglacial conditions, other (for this purpose) pessimistically chosen values on surface and sub-surface conditions resulted in modelled permafrost and perennially frozen depths of ~390 and ~360 m, respectively. In the safety assessment for the SFK repository, these results were used together with climatological information (SKB 2010, 2020) to conclude that bedrock temperatures low enough to cause detrimental effects on the canister and surrounding host rock cannot occur even under very pessimistically chosen future climate conditions (SKB 2011).

For the SFR repository, the results from permafrost simulations, together with results of climate model simulations, were used to study the timing of the first possible future period of permafrost growth at Forsmark given pessimistically chosen levels of future greenhouse gas concentrations in the atmosphere (Brandefelt et al. 2013). It was concluded that permafrost and frozen bedrock conditions affecting concrete structures can reach the repository depth after 54 000 years into the future, but not prior to that time. However, in safety assessments for SFR, the concrete barriers have degraded to such an extent within the first 50 000 years that a potential subsequent freezing would no longer significantly influence the hydraulic properties of the concrete. Therefore, it was concluded that freezing of SFR concrete structures does not contribute to the radiological risk posed by the repository (SKB 2014).

In addition to the implementation of the permafrost modelling results for these two repositories, the results have also been used in the planning of a third repository for long-lived low-level radioactive waste (SFL). In this context the results from the above permafrost simulations were used to assess a suitable repository depth in order to avoid freezing during future periglacial periods (SKB 2019).

The permafrost models used in the safety assessments were developed at the Helsinki University of Technology and Aalto University, and they have been used in several studies of permafrost and perennially frozen ground (e.g. Hartikainen 2006, 2012, SKB 2006, Hartikainen et al. 2010, Brandefelt et al. 2013). It has previously been validated against laboratory freezing experiments (Hartikainen et al. 2010, Section 3.6). The results showed that the model performed well in terms of i) the effect of fluid density differences on buoyancy flow (including so-called salt fingering), ii) the effects of pressure and salinity concentration on the freezing temperature of water, and iii) the freezing point of saline water saturated gravel.

The present study concerns an evaluation of the 2D permafrost models used in Hartikainen et al. (2010) and Brandefelt at al. (2013) by comparing simulated bedrock temperatures with observed bedrock temperatures from a site in western Greenland that hosts continuous permafrost today. At this site, the Greenland Analogue Project (GAP), a comprehensive study looking at hydrological processes associated with periglacial and glacial conditions has been performed (Claesson Liljedahl et al. 2016, Harper et al. 2016). One part of the GAP study involved the drilling and instrumentation of three bedrock holes at or close to the margin of the Greenland ice sheet (GrIS). Detailed measurements of bedrock temperatures along the 650 m deep borehole (DH-GAP04) at the ice-sheet margin were made, together with measurements of thermal bedrock properties along the borehole and characterizations of the sub-permafrost ground water chemistry (Claesson Liljedahl et al. 2016, Harper et al. 2016). The temperature measurements from this borehole show that permafrost reaches a depth of 400 m at the site today. Borehole DH-GAP01 was drilled in under a lake to investigate an assumed talik and to observe the hydrogeochemical and physical conditions in such a structure.

The aim of the present study is to investigate how simulated ground surface temperatures, permafrost depths and bedrock temperatures from the permafrost model compare with the observed data on the soil temperature from the soil temperature monitoring (STM) site near the DH-GAP01 drill site (Johansson et al. 2015a) and, on the borehole temperatures from the DH-GAP04 borehole (Claesson Liljedahl et al. 2016). In order to model the present-day bedrock temperatures at the GAP drilling sites, data of material properties of soil cover and bedrock, initial conditions and boundary conditions representative for Weichselian (Last Glacial Period) glacial conditions and Holocene periglacial conditions are required. These data are naturally associated with considerable uncertainties. In this context, a wide range of sensitivity cases are simulated to describe and handle the uncertainties in present-day and historical environmental input data.

The results from this study, in terms of the behaviour of the model when compared with ground-truth temperature observations, will be used to evaluate results and conclusions drawn from previous permafrost simulations with the same models (e.g. Hartikainen et al. 2010, SKB 2010, 2011). Previous modelling results have been used to exclude the possibility of freezing of certain repository structures at repository depth for the SFK repository under certain future climate scenarios at Forsmark (e.g. SKB 2011). In this context, the present evaluation of the permafrost model performance provides useful information to discuss e.g. possible effects of potentially overestimated modelled bedrock temperatures.

2 Site description

2.1 Overview of the study area

Greenland hosts the second largest ice-sheet in the world after the Antarctic ice-sheet. The GrIS covers approximately 1 700 000 km^2, which is roughly 80 % of the area of Greenland (Figure 2-1 and 2-2). The ice-free area, found along the coast, covers approximately 410 000 km^2 (Statistics Greenland 2008).

The Kangerlussuaq region, where the present study, as well as the previous GAP study, are focussed, is situated in south–western Greenland (Figure 2-1). Here, the distance from the coast to the ice-sheet is the largest, approximately 200 km (Fredskild et al. 1989). The position far from the sea and the proximity to the ice-sheet margin influences the local climate (see Section 2.4).

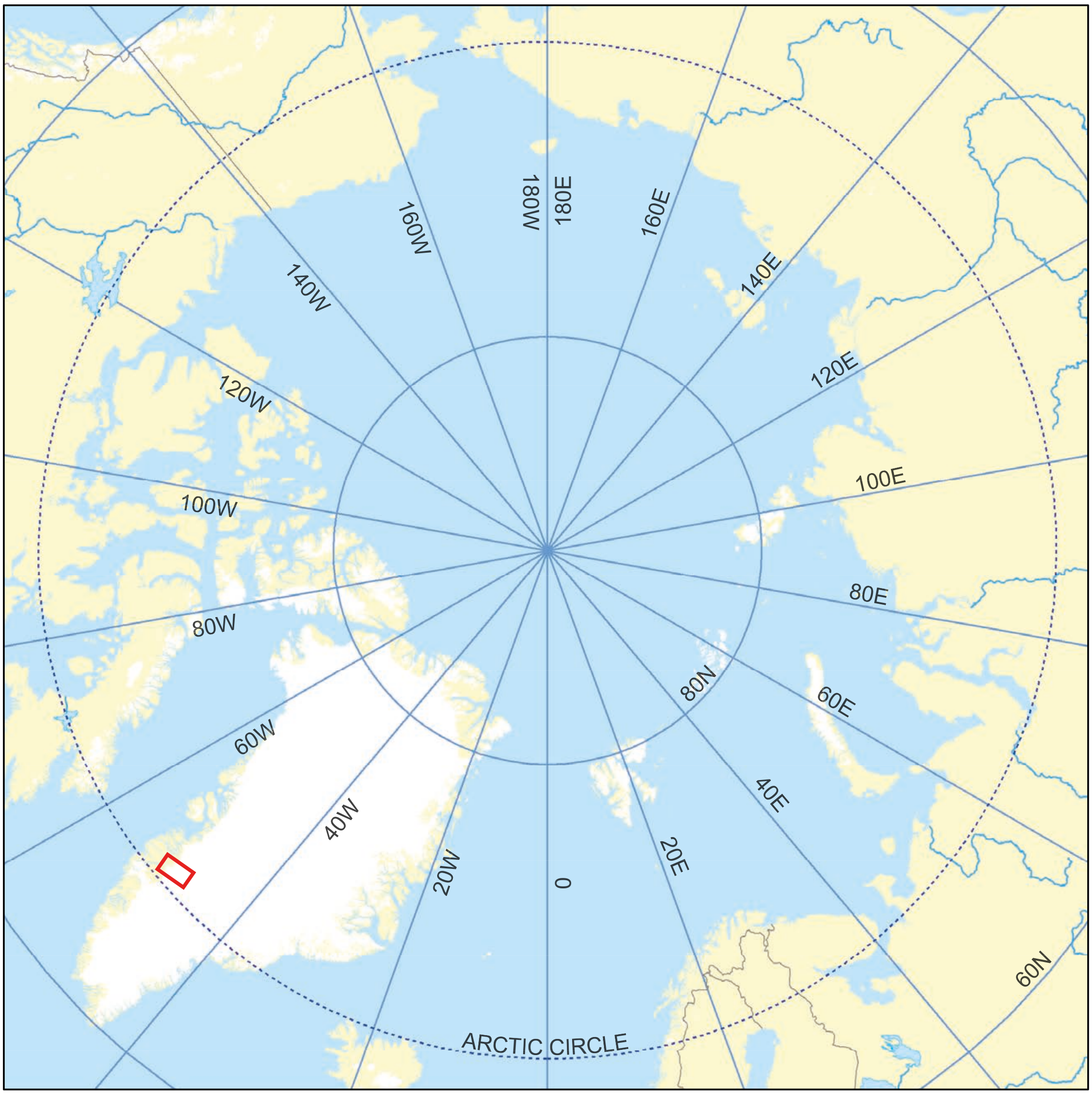

Figure 2-1. Location of the GAP study area in western Greenland (red square). The present study was conducted at the location of the DH-GAP04 bedrock drill site, located within the GAP study area, see Figure 2-3. From Claesson Liljedahl et al. (2016).

The Kangerlussuaq settlement (Figure 2-2), located to the west of the study area (Figure 2-3), has a population of approximately 500 people and is centred around the Kangerlussuaq International Airport (SFJ in Figure 2-3), which is the largest civilian airport in Greenland. In Greenlandic terms it is an easily accessible area with a gravel road leading all the way up to the ice-sheet and Point 660 (access point to the ice-sheet) (Figure 2-3), making the area an international research hub. The gravel road is currently used as an access road to the ice-sheet for tourists, researchers, and locals.

The GAP study area measured approximately 200 km from east to west and 60 km from north to south. Approximately 70 % of the study area is covered by the ice-sheet. There are a large number of lakes in the proglacial area that were studied by the GAP and the present study (Figure 2-3).

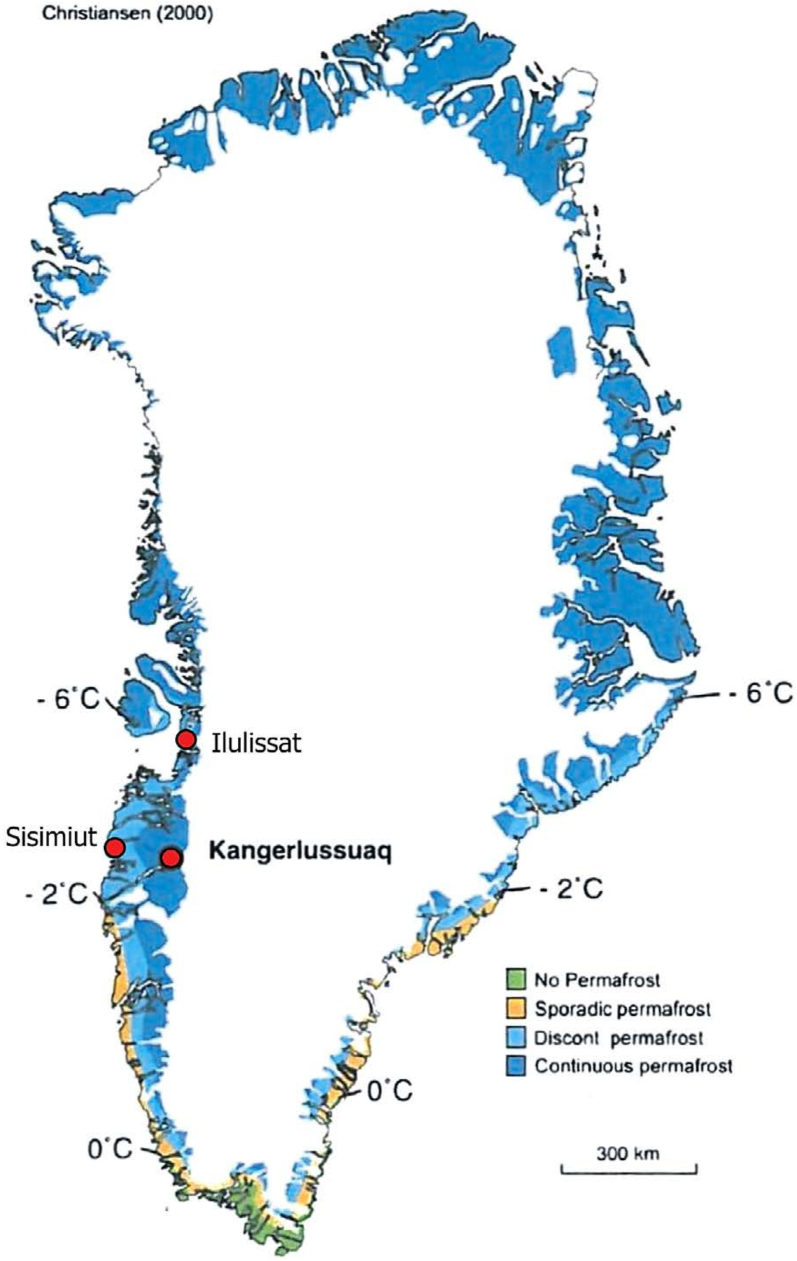

***Figure 2-2.** Location of the Kangerlussuaq, Ilulissat and Sisimiut villages, the extent of the ice-sheet and the permafrost distribution (from Christiansen and Humlum 2000, in Jørgensen and Andreasen 2007). Permafrost information does not apply to the ice-sheet area (white area). Temperature indications show average mean annual ground temperature (MAGT). Figure reprinted with permission from Elsevier.*

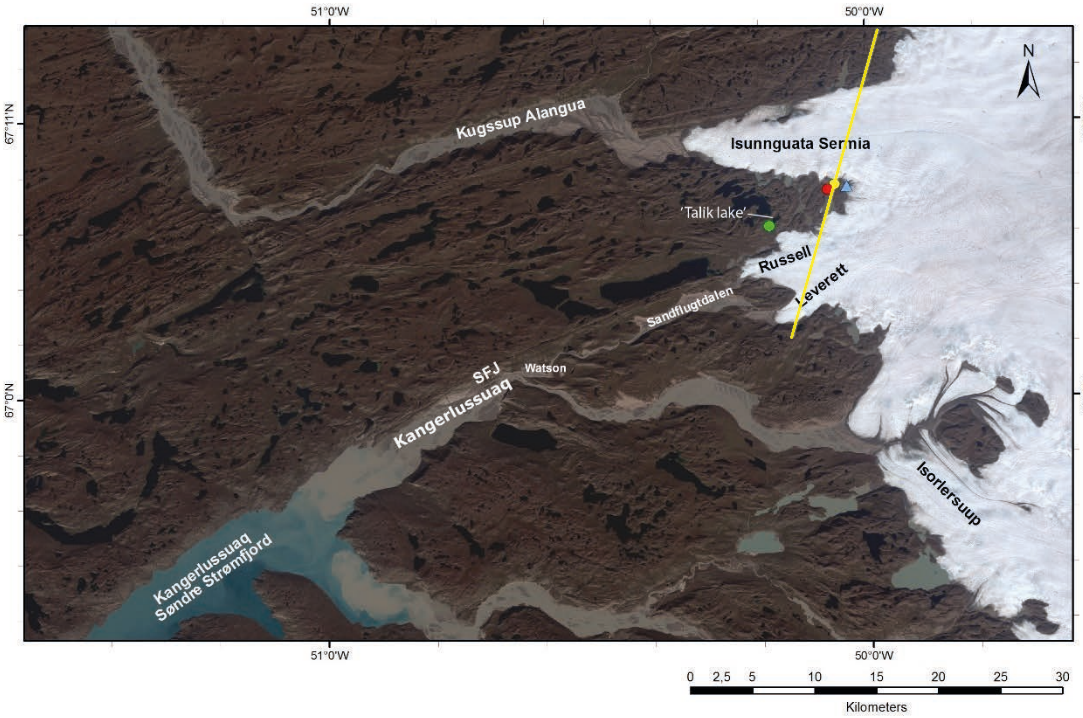

Figure 2-3. *Study area, also comprising part of the previous GAP study area (Claesson Liljedahl et al. 2016). Isunnguata Sermia, Russell, Leverett and Isorlersuup form the major outlet glaciers in the area, whereas Sandflugtdalen and Kugssup Alanqua constitute the major valleys of the present study. Locations of the bedrock boreholes drilled by the GAP are indicated as coloured circles. Green circle = DH-GAP01 (see also Figure 2-6), red circle = DH-GAP03, and yellow circle = DH-GAP04 (see also Figure 2-5). The permafrost modelling performed in the present study was made along a 25 km profile crossing the DH-GAP04 borehole (yellow line), see also Figure 3-1. The proglacial 'Talik lake', KAN-B automatic weather station, and soil temperature monitoring (STM) site (see the text) are all located at the site of the DH-GAP01 borehole (green). The map clearly shows the many proglacial lakes with light grey coloured lakes being glacial meltwater lakes whereas dark lakes are lakes without inflow of glacial meltwater. The northernmost tip of the approximately 170 km long Søndre Strømfjord is shown in the lower left corner. SFJ = Kangerlussuaq International Airport. Blue triangle shows the location of Point 660. Background Landsat image was acquired 23 August 2000. Modified from Claesson Liljedahl et al. (2016).*

2.2 Geological setting

Greenland is dominated by Precambrian shield crystalline rocks, where the oldest areas constitute a basement shield composed of strongly folded gneissic rocks representing the root zone of Archean (3 800–2 550 Ma old) and Proterozoic (2 000–1 750 Ma) orogenic belts. These belts are now merged to form a stable coherent block surrounded by sedimentary basins formed in the Proterozoic, the Cambrian–Silurian period and the Devonian–Neogene period (Fredskild et al. 1989, Henriksen et al. 2000). The Kangerlussuaq area is located in the Precambrian region of south–western Greenland (Henriksen et al. 2000), where bedrock is dominated by gneisses (see Figure 2-5 in Claesson Liljedahl et al. 2016). The area is situated within the southern part of the Nagssugtoqidian Orogen, which consists of an approximately 1 900 to 1 800 Ma old fold belt that formed in a collision zone between two parts of a previously rifted large Archaean continent. The rocks in the Nagssugtoqidian Orogen are predominantly Archaean ortho-gneisses, with minor amounts of amphibolite and metasedimentary rocks that were reworked under high-grade metamorphic conditions in the Palaeo–Proterozoic (van Gool et al. 2002, Garde and Hollis 2010). In addition, occasional intrusions of mafic dykes occur across the study area (Mayborn and Lesher 2006). The primary structures reflect the ductile to semi-ductile nature of the regional deformation, including macroscale folds, a penetrative gneissic fabric and evidence of shearing. The more brittle structures, such as open faults and fractures, are regarded as having been formed in a younger shallow, colder, and hence, more rigid environment.

According to regional lineament studies by Wilson et al. (2006), which focused on the on-shore expression of continental break-up and sea-floor spreading in central West Greenland, five main lineament systems were identified: N–S, NNE–SSW, ENE–WSW, ESE–WNW and NNW–SSE. Based on lineament interpretation and field observations in the GAP study area, over a hundred major deformation zones/large lineaments were identified (Engström et al. 2012). Apart from confirming the five systems identified by Wilson et al. (2006), a sixth sub-horizontal system was identified in the study area (Engström et al. 2012). For more information on the geology of the area, see Claesson Liljedahl et al. (2016).

2.3 Landscape

The landscape in the Kangerlussuaq area is typical of central West Greenland, which is a fiord landscape with numerous long (typically around 25 km), narrow and up to 600 m deep fiords that terminate in U-shaped valleys. Some of these valleys contain outlet glaciers and terraces, whereas others are partially filled with terraces of glaciofluvial and marine sediments (Ten Brink 1975). The latter is true for the valley where Kangerlussuaq is located. The Kangerlussuaq fiord (or Søndre Strømfjord) is approximately 170 km long and between 1 to 6 km wide and receives the majority of the meltwater discharge from the large area south of the Russell Glacier, whereas the majority of the meltwater from the terminus of the Isunnguata Sermia outlet glacier is transported via Kugssup Alangua (Figure 2-3) to the Sisimiut Isortuat fiord, north of Kangerlussuaq.

Meltwater from the Russell and Leverett outlet glaciers drain through the two branches of the Watson River, which merge at the 2–3 km wide Sandflugtdalen floodplain, at the terminus of the Russell Glacier (Figure 2-3). The thickness of the glaciolacustrine and glaciofluvial deposits in this valley is up to 80 m (Storms et al. 2012). Southwest of Sandflugtdalen, the valley narrows, resulting in thinner deposits. Close to Kangerlussuaq, the sediments are typically 30 m thick. The head of the Søndre Strømfjord is filled with terraces of glaciofluvial and marine sediments of Holocene age (Storms et al. 2012).

The highest marine limit, based on the presence of elevated marine clay terraces, is located at an elevation of 40 ± 5 m a.s.l. (Ten Brink 1974). However, since marine clays do not necessarily refer to a palaeo-coastline elevation, this is considered a minimum value on the highest marine limit (Storms et al. 2012). The upward vertical displacement rate of the bedrock during Neoglacial time (i.e. the last 4 000 years of the Holocene) has varied between 20 mm/a (Weidick 1993, 1996) and −5.8 mm/a (Wahr et al. 2001). The vertical subsidence is attributed to the readvance of the ice-sheet during the past 3 000 – 4 000 years (Tarasov and Peltier 2002, Dietrich et al. 2005). Dietrich et al. (2005) report a current subsidence rate of 3.1 mm/a for Kangerlussuaq. Till cover on elevated areas is usually rather thin and heavily eroded by wind, or absent (Claesson Liljedahl et al. 2016). Due to the arid conditions, and the supply of fine-grained sediments, various types of eolian deposits are widespread in the area (Willemse et al. 2003).

For more information on the landscape and Quaternary deposits of the area, see Claesson Liljedahl et al. (2016).

2.4 Climate and permafrost at the GAP and 'Talik lake' sites

The present-day climate in the GAP study area, including the location of the DH-GAP04 borehole site (Figure 2-5), is considered low Arctic continental, with continuous permafrost (Willemse et al. 2003). The region is characterised by a steep climate gradient from the coast to the inland, with mild winters and cool summers with varying weather in the coastal zone and warmer, stable summers but colder winters in the inland zone. The GrIS, reaching an elevation of 3 000 m a.s.l., has a dominant influence on precipitation and winds (Jørgensen and Andreasen 2007).

The Danish Meteorological Institute (DMI) operates a weather station in Kangerlussuaq. Figure 2-4 shows the mean monthly air temperatures from this station for the period 1961–2013 (Cappelen et al. 2001, Cappelen 2012). For detailed temperature information see Appendix A2. The mean annual air temperature (MAAT) at the Kangerlussuaq International Airport average −5.1 °C, ranging from −9.1 to −0.3 °C (temperature record spanning 1977–2011, Cappelen 2012), whereas the mean annual ground temperature (MAGT) close to the airport is approximately −2 °C at 1.25 m below ground surface (van Tatenhove and Olesen 1994). Closer to the ice-sheet margin, at the DH-GAP01 drill site (Figure 2-3) by the 'Talik lake' (or 'Two boat lake', see below) (Figure 2-6), the MAGT for the period 2010–2013 was measured to be −3.0 °C at 1.25 m depth and −2.8 °C at 0.25 m depth (Johansson et al. 2015a). MAAT for the same location (from the KAN_B weather station) and period was −4.2 °C. Sub-zero air temperatures typically prevail at Kangerlussuaq between October to May, with winter temperatures down to −40 °C and summer temperatures up to +20 °C.

The 1961–1990 period is considered to represent a period during which the GrIS was in approximate balance (e.g. van Angelen et al. 2012). After this period, the mass balance of the ice-sheet has become negative (see below). Although the weather naturally fluctuates from year to year, the GAP study was carried out during a period with significantly warmer temperatures than the average for the 1961–1990 period (Figure 2-4).

A clear negative precipitation gradient is present from the coast to the inland. At Sisimiut, situated by the coast approximately 120 km west of Kangerlussuaq (Figure 2-2), the annual mean precipitation is 383 mm (average for 1961–1990). The corresponding value at Kangerlussuaq, approximately 170 km from the coast, measured at the DMI weather station is 173 mm (measured between 1977–2011), i.e. a desert-like annual precipitation (Cappelen 2012). At Kangerlussuaq, 40 % of the annual precipitation falls as snow and 60 % as rain. Mean surface wind speeds are low (less than 5 m/s) in the ice-free regions of the GAP study area. Winds are dominantly easterly at ground level, an effect of thermally-induced katabatic winds from the ice-sheet and airflow channelling in the valleys (van den Broeke and Gallée 1996). The vegetation near the ice-sheet margin consists of dwarf-shrub tundra and steppe, with fell fields present throughout the region (Willemse et al. 2003, Engels and Helmens 2010).

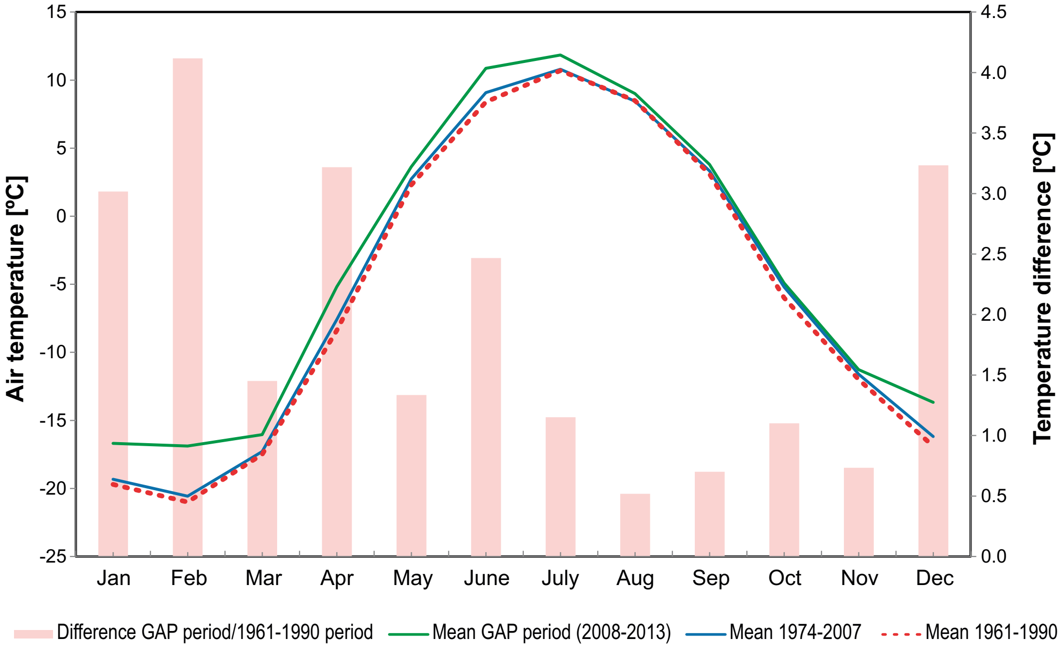

Figure 2-4. *Monthly mean air temperatures from the DMI weather station in Kangerlussuaq for the periods 1961–1990, 1974–2007 and the GAP study period 2008–2013. The 1961–1990 period is considered to represent a period during which the GrIS was in approximate mass balance (e.g. van Angelen et al. 2012). The temperature difference between the GAP period and the 1961–1990 period is shown as coloured bars. From Claesson Liljedahl et al. (2016).*

Kangerlussuaq is located in the southern part of the continuous permafrost zone (Figure 2-2 and Brown et al. 1997). Based on the MAAT and MAGT, permafrost at the Kangerlussuaq airport was previously modelled to be 100–160 m thick (van Tatenhove and Olesen 1994). Close to the ice margin and at higher elevations, such as at the GAP bedrock drill sites (Figure 2-3), the permafrost thickness reaches approximately 350–400 m (Harper et al. 2016). Electromagnetic soundings have shown that a wedge of permafrost extends in under the ice-sheet for a distance of at least 2 km (Ruskeeniemi et al. 2018). This is the case even though the basal ice temperature in the area is observed to be at the pressure melting point (e.g. Claesson Liljedahl et al. 2016, Harper et al. 2016, Harper et al. 2019), see also below. The active layer in the area between Kangerlussuaq and the ice-sheet margin has a thickness of 0.15 to 5 m (van Tatenhove and Olesen 1994). At the 'Talik lake' site (see below and Figure 2-3), the thickness of the active layer is ~ 1 m (Johansson et al. 2015a). Areas with sandy inorganic soils and discontinuous vegetation, such as at the Talik lake site, tend to have warmer soil temperatures and a deeper active layer than organic soils covered with dense vegetation (van Tatenhove and Olesen 1994). Periglacial features such as pingos and ice-wedges are found in the area (e.g. Scholz and Baumann 1997).

Permafrost has a great impact on the hydrological cycle (White et al. 2007). Since extensive permafrost acts as a largely impermeable layer, groundwater recharge and discharge are reduced, and, in areas with continuous permafrost, groundwater recharge and discharge are restricted to taliks, i.e. unfrozen zones in the permafrost (e.g. Kane et al. 2013, Bosson et al. 2012). Taliks are assumed to be abundant in the GAP study area and occur beneath large lakes, rivers and fiords. Through taliks, i.e. taliks extending through the entire thickness of the permafrost, are hypothesised to provide exchange of deep and shallow groundwater, a process that has been investigated and observed within the GAP and GRASP (Greenland Analogue Surface Project) studies, the latter being a SKB-funded project focusing on lake drainage area hydrology and ecosystems (e.g. Johansson et al. 2015a, b).

Figure 2-5. *Left: The DH-GAP04 borehole site. The top of the borehole is located inside the grey container. The borehole is inclined towards the ice-sheet, i.e. into the picture. The slope between the top of borehole location and the ice-sheet margin (see topographic profile in Figure 3-2) is not seen in the left figure since it is hidden by the hill. Right: partly snow-covered slope down towards the margin of the Isunnguata Sermia outlet glacier, looking towards north–east from the borehole location. Local snow accumulation is documented, by time-lapse photography, to happen regularly in the slope down to the ice-sheet margin in this area. Left photo taken September 18 2021, right photo April 19 2012, both by Lillemor Claesson Liljedahl.*

Thermal modelling to evaluate the required size of a water body to retain a through talik was undertaken using circular lakes (SKB 2006). The results from this simplified study showed that a lake radius of 0.6 times the thickness of the surrounding undisturbed permafrost is sufficient for a deep lake to maintain a through talik. Tentative thermal modelling of the 'Talik lake' (Figure 2-3 and 2-6) has shown that through taliks can form through a 300 m deep layer of permafrost in less than 500 years, provided that the lake is wider than about 200 m. Open taliks (i.e. open upwards to the ground surface but confined by frozen bedrock at depth) can form in less than 100 years beneath lakes that are about 100 m wide (Harper et al. 2011, Harper et al. 2016). Considering a permafrost depth of approximately 350 to 400 m (see Section 2.4.5) in the GAP study area, a lake diameter of c 360–420 m is required to maintain through taliks. The GAP study area encompasses several hundreds of proglacial lakes (Figure 2-3 and Claesson Liljedahl et al. 2016). About 20 % of these lakes (6 % of the land surface area) have a diameter larger than 400 m (see Figure 2-7 in Claesson Liljedahl et al. 2016). This suggests that the permafrost in this area is perforated by through taliks, and flow pathways available for exchange of surface water and deep groundwater through the permafrost are abundant.

The 'Talik lake' site

The 'Talik lake' (elsewhere also denoted 'Two boat lake'. Both names are unofficial names) refers to a specific lake/talik system in the proglacial part of the GAP study area (Figure 2-3 and 2-6), was investigated as part of the GAP (Claesson Liljedahl et al. 2016, Harper et al. 2016) and GRASP (e.g. Johansson et al. 2015a, b) studies. The lake is approximately 1 200 m long and 300–400 m wide, and has a surface area of 0.37 km^2. The lake is located at an elevation of 369 m and is situated approximately 800 m from the ice-sheet margin. The area of the catchment is 1.56 km^2. The average and maximum lake water depths are 11.3 m and 29.9 m, respectively (Johansson et al. 2015a). The lake is situated in an area characterised by continuous permafrost, but results from the GAP project have conclusively shown that the lake supports a through talik. Stable isotopic conditions of the talik water indicated ongoing recharging conditions in the talik/lake system (Claesson Liljedahl et al. 2016), whereas modelling results showed that recharge and discharge conditions in the lake/talik system may shift in time and space (Johansson et al. 2015a, b, Vidstrand 2017). The DH-GAP01 borehole is located beside the lake at approximately 20 m distance from the lake shoreline (Figure 2-6). The borehole is angled and extends in under the lake. Temperature profiling in borehole DH-GAP01 shows that the upper c 20 m of the borehole is within permafrost and that unfrozen soil/bedrock conditions exists further down in under the lake. This allows for a hydraulic contact between the lake and the deep groundwater system below the permafrost (Harper et al. 2011).

Figure 2-6. The 'Talik lake' and the location of borehole DH-GAP01 (green dot). The location of the 'Talik lake' and the DH-GAP01 borehole is shown in Figure 2-3. The lake is approximately 1 200 m long and 350 to 400 m wide. The photograph was taken in 2012 by Tobias Lindborg. From Claesson Liljedahl et al. (2016).

Johansson et al. (2015a) summarise the 'Talik lake' catchment characteristics as follows: the catchment area is dominated by glacial till and glaciofluvial deposits which to a large part are overlain by a layer of eolian silt to fine sand. The total depth of eolian sediments and glacial deposits ranges from 7–12 m in the valleys to zero along the hill sides. In the lake, a sediment thickness of up to 1.5 m has been observed (Petrone et al. 2016). It is assumed that the observed depth of glacial deposits in the valleys of the catchment is also present in the lake, i.e. the lake sediments are underlain by approximately 10 m of glacial till. The glacial till was deposited under the ice-sheet and glaciofluvial sediments were deposited mostly in front of the ice margin during deglaciation of the area. Eolian silt to fine sand has periodically been deposited after the area was deglaciated (Willemse et al. 2003).

The catchment hydrology constitutes a precipitation-driven system, with no meltwater inflow from the ice-sheet occurring over the catchment boundary. Vegetation in the catchment is dominated by dwarf-shrub heath. There are no trees in the catchment, and bushes rarely exceed a height of 0.5 m. The poor vegetation results in relatively low transpiration even though the total evapotranspiration in the catchment is relatively high. The only visible stream is at the lake outlet. Due to the low precipitation in the area, the stream at the outlet of the lake is dry during long periods and the summer of 2009 was the last time, as of September 2014, that surface water outflow was observed to occur from the lake (Johansson et al. 2015a, b).

2.5 Characteristics of the Greenland ice-sheet in the GAP study area

The ice-sheet part of the GAP study area includes the Isunnguata Sermia, Russell, Leverett and Isorlersuup outlet glaciers and their catchment areas (see Figure 2-3). The ice thickness in the study area reaches approximately 1 500 m with a mean thickness of approximately 800 m (Lindbäck et al. 2014). However, the ice thickness is highly variable due to the steep and undulating subglacial topography. The ice flow direction in the area is generally directed from east to west, with a mean surface velocity of c 150 m/a (Joughin et al. 2010). The glaciated part of the GAP study area is one of the most studied regions of the GrIS including studies of mass balance (e.g. van de Wal et al. 2012) and ice dynamics (e.g. van de Wal et al. 2008, Bartholomew et al. 2011, Palmer et al. 2011, Sole et al. 2013, Claesson Liljedahl et al. 2016, Harper et al. 2016, 2019). One reason for the research interest in this area is the fact that the land-terminating outlet glaciers here are isolated from marine influences and exhibit changes in ice dynamics that are unrelated to tidewater influences and are directly attributable to surface-melt forcing (Fitzpatrick et al. 2014).

As previously mentioned, the period 1961–1990 is often used as a reference to when the GrIS was considered to be in approximate steady-state, whereas during the past 20 years the mass balance has turned negative (van Angelen et al. 2012). A recent strong warming over the western part of the GrIS is recorded by e.g. weather stations in the GAP study area (van As et al. 2012, van Angelen et al. 2014). The negative mass balance has resulted in a larger melt extent of the GrIS with an associated increased surface runoff and discharge (Hanna et al. 2008, Ettema et al. 2009, Fettweis et al. 2011, van As et al. 2012). Recent studies have also shown, with examples from this part of the ice-sheet, that the sub- and englacial water storage in the ice-sheet is changing with climate (Rennermalm et al. 2013) and hence that the local hydrology may be out of balance at present.

2.6 Deglaciation history of southern West Greenland

The average long-term climate conditions (glacial-, periglacial-, or temperate climate) that have prevailed at the GAP bedrock drill sites are of relevance to for e.g. geochemical-, geothermal- and permafrost analyses. A rough estimate of the average glacial cycle conditions at the GAP site was made by employing a glacial history perspective. The present configuration of the GrIS is to a major extent a result of the warm Holocene interglacial climate conditions. During glacial periods, the ice-sheet is typically significantly larger. For the past ~2.5 Ma, glacial conditions have dominated Earth's climate (e.g. Lisiecki and Raymo 2005). In Northern Hemisphere high- to mid-latitudes, this has resulted in larger ice-sheets than at the present-day. In e.g. Fennoscandia, the typical ice-sheet distribution for at least the past 1 Ma therefore contained significantly more ice than the present, very restricted, mountain glaciation (Porter 1989, Kleman et al. 2008). Also, it is very likely that the average configuration of the GrIS has been larger than the present one for the past million years, since this was the case for both the Fennoscandian and Laurentide ice-sheets at similar latitude (e.g. Porter 1989).

Given that the GAP bedrock boreholes are located in the proglacial marginal area of the present-day ice-sheet, it is likely that the drill sites have been dominated by ice-covered conditions, on average, over the past 1 Ma. During the relatively shorter interstadial and interglacial periods, the drill sites could either have experienced periglacial climate conditions (i.e. with presence of permafrost) or even temperate climate conditions (here defined as a warm climate without presence of permafrost or an ice-sheet). However, on average for the whole 1 Ma period, glacial conditions most probably have dominated.

During the Last Glacial Maximum (LGM), the GrIS was much more extensive than at present and the ice-sheet margin extended offshore, at least onto the continental shelf (Fredskild et al. 1989, Bennike and Björk 2002), see Figure 2-7. At the beginning of the Holocene, the ice margin retreated towards the east to a position close to the modern coastline (Funder and Hansen 1996). Subsequently, due to increasing air temperatures and low annual precipitation (Anderson and Leng 2004, Aebly and Fritz 2009), the ice margin continued to retreat. During the resulting deglaciation, a series of regional moraine systems formed during temporary halts in the retreat. In the GAP study area, such moraine systems have been mapped and dated by Ten Brink and Weidick (1974), van Tatenhove et al. (1996), Forman et al. (2007) and Levy et al. (2012). Deglaciation of the present-day coastal area in south–western Greenland started around 12.3 ka BP, and most of the ice-sheet margin reached its present position between 6.5 and 7 ka BP (Ten Brink and Weidick 1974, van Tatenhove et al. 1996). The retreat was fast and, at ~6 ka BP, the ice margin was behind its present position and remained there until the Little Ice Age (LIA) readvance (van Tatenhove et al. 1996, Forman et al. 2007). It is assumed that the minimum position was reached by 5 ka BP (Weidick 1993). Neoglacial readvance may have started as early as 4800 years BP and culminated about 2 ka BP (van Tatenhove et al. 1996, Forman et al. 2007). The climate subsequently started to warm and around 1 ka BP it was warmer than at present. The ice-sheet advanced again during the LIA, when the ice margin of western Greenland was approximately 1–2 km west from its current position (Csatho et al. 2005). During the LIA, the Isunnguata Sermia ice margin was only 50–200 m beyond its present margin (Forman et al. 2007), with the maximum position reached around 1850 AD. However, the DH-GAP04 drill site (Figure 2-5) has probably not been ice covered during the past 7.1 ka (cf Levy et al. 2018). Forman et al. (2007) reported that the ice-sheet has retreated to its present position over the past 100 years. Thinning of the ice-sheet at elevations below 1500 m a.s.l. has accompanied this retreat (Krabill et al. 2000, Johannessen et al. 2005). Based on current understanding, neither of the GAP bedrock borehole drill sites (see Section 2.4) were ice-covered during the LIA (cf Forman et al. 2007).

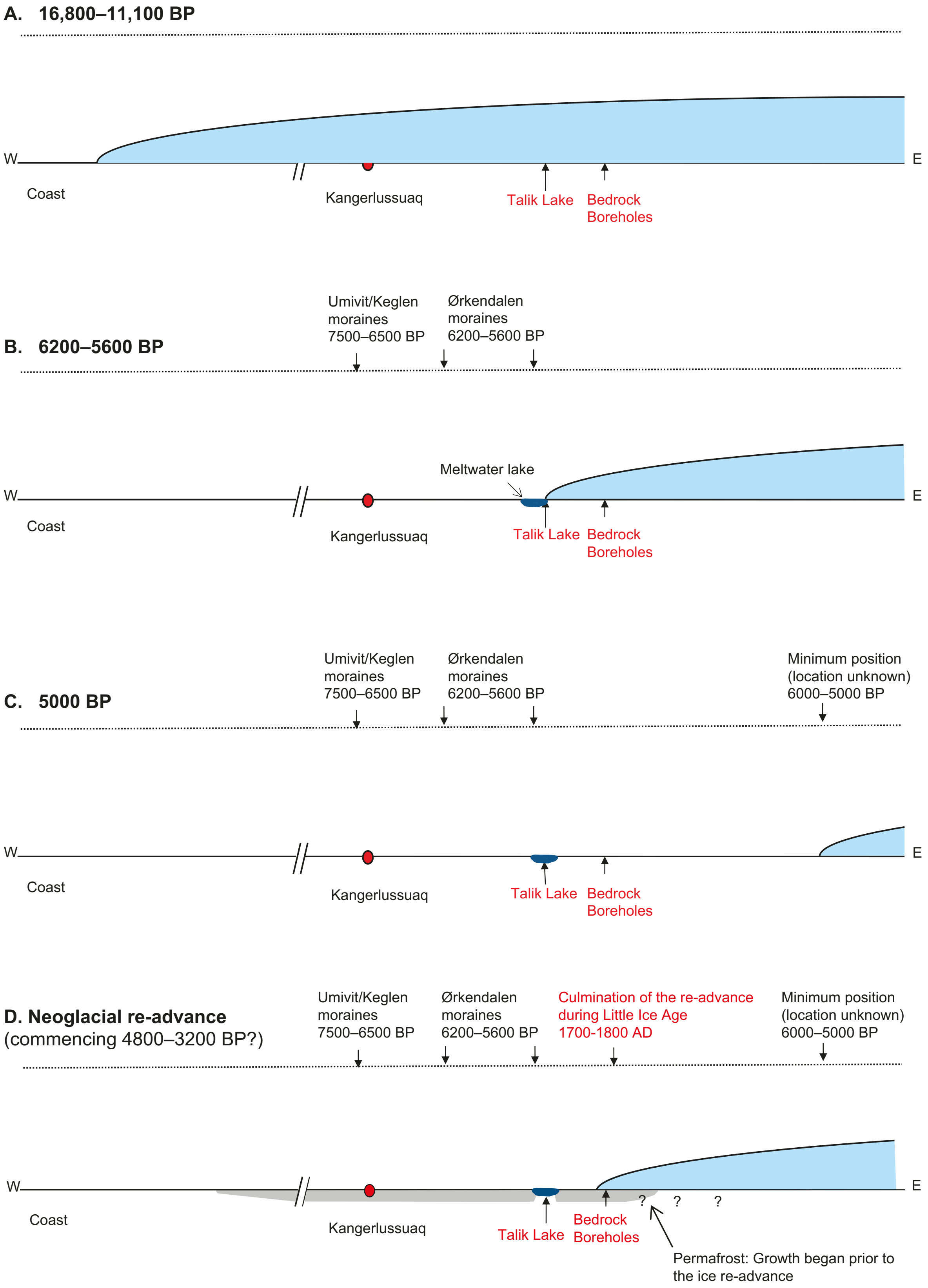

***Figure 2-7.** Cartoon showing the deglaciation history of the Kangerlussuaq area (Figure 2-2 and 2-3) since the Last Glacial Maximum (LGM). Many of the present lakes were likely formed as soon as the area was exposed from the retreating ice-sheet. These lakes were first filled with meltwaters and later turned into non-glacial lakes, implying that the growth of permafrost was prevented under these lakes when the climate started to cool during the neoglacial re-advance. Moraine ages are presented as ^{14}C BP and are from van Tatenhove et al. (1996). From Claesson Liljedahl et al. (2016).*

3 Methods and input data

3.1 Permafrost models

Two versions of the permafrost model are evaluated in the present study, the permafrost models used in Hartikainen et al. (2010) and Brandefelt et al. (2013) employed at the Forsmark site, south central Sweden, referred to as Model A and Model B, respectively. The models compute the time-evolution of i) ground surface, soil and bedrock temperatures, ii) groundwater pressure, and iii) groundwater salinity concentration. The computations make use of a representation of the initial thermal and hydrogeochemical state of the ground and the model domain boundary conditions as well as data on measured thermal and hydraulic properties of the soil and bedrock.

The permafrost models (A and B) consist of two sub-models: a continuum mechanics-based subsurface model for freezing and thawing ground, and a statistical surface model that generates transient thermal and hydraulic upper boundary conditions for the subsurface model. The A and B permafrost models are identical, except that the surface model of Model B also accounts for the thermal offset induced by the seasonal freezing and thawing of the active soil layer (Goodrich 1978).

3.1.1 Subsurface model

The subsurface model is based on the principles of continuum mechanics and theories of mixture and porous medium. It is composed of the balance laws of mass, momentum and energy accompanied by constitutive equations for heat conduction, groundwater flow, transport of dissolved salts, and the phase change between water and ice. The model represents the relevant cryogenic processes of freezing and thawing of ground including heat transfer, density-dependent groundwater flow and salt transport, freezing and melting of pressurised saline groundwater, and the exclusion of salt during freezing. The perennially frozen ground is defined by the equilibrium of Gibb's free energy function between water and ice depending on the temperature, groundwater pressure, salinity concentration and physicochemical properties of rock and soil. Deformations of the soil and bedrock are omitted in the permafrost model. The output consists of time series for mean annual ground temperature (MAGT), groundwater pressure and salinity concentration of groundwater as well as heat diffusion, groundwater flow and diffusion-dispersion of salt in groundwater. The formulation of the model is given in Hartikainen et al. (2010) and the comprehensive thermodynamic derivation is presented in Hartikainen (2018).

3.1.2 Surface models

The surface model renders climate and environmental conditions into transient thermal and hydraulic surface boundary conditions for the subsurface model. To calculate the ground surface temperature for vegetated and barren locations, the air temperature is used together with empirical ratios between the ground surface temperature and air temperature, so-called *n*-factors. These *n*-factors are summarised below and the representative values for the non-glaciated GAP site are determined. A more detailed description is given in Hartikainen et al. (2010).

The mean annual ground surface temperature (MAGST), $\overline{T}_s$, is determined by MAAT, $\overline{T}_a$, the annual air temperature amplitude A_a as well as the freezing and thawing *n*-factors n_{fr} and n_{th} by the following equations

$$\overline{T}_s = a\overline{T}_a + b, \qquad (3\text{-}1)$$

where

$$a = \left[\frac{1}{2} - \frac{1}{\pi}\arcsin\left(\frac{\overline{T}_a}{A_a}\right)\right] n_{fr} + \left[\frac{1}{2} + \frac{1}{\pi}\arcsin\left(\frac{\overline{T}_a}{A_a}\right)\right] n_{th} \qquad (3\text{-}2)$$

and

$$b = \frac{1}{\pi}\cos\left[\arcsin\left(\frac{\overline{T}_a}{A_a}\right)\right](n_{th} - n_{fr})A_a. \qquad (3\text{-}3)$$

The annual air-temperature amplitude is assumed to depend on the prevailing climate, such that it becomes larger (smaller) when MAAT decreases (increases):

$$A_{\mathrm{a}} = \begin{cases} 9\ {}^{\circ}\mathrm{C} - 0.4\bar{T}_{\mathrm{a}}, & \text{High precipitation variant} \\ 10\ {}^{\circ}\mathrm{C} - 0.7\bar{T}_{\mathrm{a}} & \text{Low precipitation variant} \end{cases}, \tag{3-4}$$

where, following Hartikainen et al. (2010), 9 °C and 10 °C are the air temperature amplitudes for the MAAT = 0 °C. The low precipitation variant represents conditions typical for more arid climates, whereas the high precipitation variant represents conditions typical for climates with higher moisture content in the air and more abundant precipitation. These differences imply that the low precipitation variant has a larger amplitude of the seasonal cycle than high precipitation variant.

The *n*-factors are defined by the equations

$$n_{\mathrm{fr}} = \frac{\int_0^{t_{\mathrm{s}-}} T_{\mathrm{s}}(\mathrm{t})\,\mathrm{d}t}{\int_0^{t_{\mathrm{a}-}} T_{\mathrm{a}}(\mathrm{t})\,\mathrm{d}t}\ \forall\, T_{\mathrm{s}} < T_{\mathrm{fr}},\ T_{\mathrm{a}} < 0^{\circ}\ \mathrm{C}, \quad n_{\mathrm{th}} = \frac{\int_0^{t_{\mathrm{s}+}} T_{\mathrm{s}}(\mathrm{t})\,\mathrm{d}t}{\int_0^{t_{\mathrm{a}+}} T_{\mathrm{a}}(\mathrm{t})\,\mathrm{d}t}\ \forall\, T_{\mathrm{s}} \geq T_{\mathrm{fr}},\ T_{\mathrm{a}} \geq 0^{\circ}\ \mathrm{C}\,, \tag{3-5}$$

such that the freezing *n*-factor, n_{fr} is the relation between the annual time integrals of the interannual (daily or monthly) ground surface temperature $T_{\mathrm{s}}(t)$ and the air temperature $T_{\mathrm{a}}(t)$ below the freezing point T_{fr} and 0 °C. The thawing *n*-factor, n_{th} is the relation between the time integrals of the interannual ground surface temperature and the air temperature above T_{fr} and 0 °C, respectively (Lunardini 1978). The negative and positive signs in the integral limits signify the periods of a year t_{y} when the temperatures are below and above these limits.

The *n*-factors have been defined in Hartikainen et al. (2010) for boreal, sub-arctic and arctic climatic zones, and for dry, fresh-moist and wet surface moisture conditions based on field measurements for prevailing climates, vegetation and surface moisture conditions in permafrost regions in North America (Klene et al. 2001, 2008, Karunaratne and Burn 2003, 2004, Kade et al. 2006, Hinkel et al. 2008, Karunaratne et al. 2008). The values for arid climates with low precipitation (Dry variant in Hartikainen et al. 2010) and for damp climates with abundant precipitation (Humid variant in Hartikainen et al. 2010) are represented in Table 3-1 and Table 3-2, respectively. Precipitation acts on the different surface moisture conditions through the *n*-factors by a smaller *n*-factor for higher precipitation.

The representative *n*-factors for the GAP site are interpolated from the prescribed values by mapping the measured five-year (2011–2016) monthly mean summer (June–August) precipitation of 24 mm and winter (December–February) precipitation of 16 mm as measured at the meteorological station (KAN_B) located at the DH-GAP01 site (Johansson 2016) against the precipitation thresholds in Table 3-1 and Table 3-2. The results are presented in Table 3-3. The annual air temperature amplitude shown in the table is computed by using air temperature and precipitation data from the DH-GAP01 site (Johansson et al. 2015a, Johansson 2016).

Table 3-1. Freezing and thawing *n*-factors for arid climates with low precipitation ('Dry variant' in Hartikainen et al. 2010) for boreal, subarctic and arctic climatic zones and dry, fresh-moist and wet surface moisture conditions.

Climatic zone	Air temperature (°C)		Monthly mean precipitation (mm)		*n*-factors			
	MAAT	Amplitude	Winter	Summer		Surface moisture condition		
					TWI	Dry < 10.9	Fresh-moist 10.9–13.2	Wet > 13.2
Boreal	> 0	< 13	10	10	n_{th}	1.4	1.4	1.4
					n_{fr}	0.3	0.3	0.3
Subarctic	−6–0	17–13	1	5	n_{th}	1.0	0.9	0.8
					n_{fr}	0.9	0.8	0.6
Arctic	< −6	> 17	1	5	n_{th}	1.2	0.8	0.7
					n_{fr}	1.0	0.8	0.6

Table 3-2. Freezing and thawing *n*-factors for damp climates with abundant precipitation ('Humid variant' in Hartikainen et al. 2010) for boreal, subarctic and arctic climatic zones and dry, fresh-moist and wet surface moisture conditions.

Climatic zone	Air temperature (°C)		Monthly mean precipitation (mm)		*n*-factors			
	MAAT	Amplitude	Winter	Summer		Surface moisture condition		
					TWI	Dry < 10.9	Fresh-moist 10.9–13.2	Wet > 13.2
Boreal	> 0	< 11	50	60	n_{th}	1.2	1.2	1.2
					n_{fr}	0.2	0.2	0.2
Subarctic	−6 – 0	13–11	40	60	n_{th}	0.8	0.7	0.6
					n_{fr}	0.5	0.4	0.2
Arctic	< −6	> 13	40	60	n_{th}	0.8	0.5	0.4
					n_{fr}	0.7	0.4	0.3

Table 3-3. Freezing and thawing *n*-factors for the GAP site for boreal, subarctic and arctic climatic zones and dry, fresh-moist and wet surface moisture conditions based on the present-day precipitation.

Climatic zone	Air temperature (°C)		*n*-factors			
	MAAT	Amplitude		Surface moisture condition		
			TWI	Dry < 10.9	Fresh-moist 10.9–13.2	Wet > 13.2
Boreal	> 0	< 12	n_{th}	1.34	1.34	1.34
			n_{fr}	0.29	0.29	0.29
Subarctic	−6 – 0	16–12	n_{th}	0.93	0.83	0.73
			n_{fr}	0.75	0.65	0.45
Arctic	< −6	> 16	n_{th}	1.06	0.70	0.60
			n_{fr}	0.88	0.65	0.48

Thermal offset

The thermal offset (TO) is a decrease in MAGT in the active layer, influencing MAGT throughout the bedrock. It is mainly caused by the change in soil thermal conductivity due to seasonal freezing and thawing of the active soil layer (Goodrich 1978). Using the unfrozen and frozen thermal conductivity of soil k, TO can be defined by the double integral

$$\Delta T = -\frac{1}{k(\bar{T}_s)}\frac{1}{t_y}\int_0^{t_y}\int_{\bar{T}_s}^{T_s(t)} k(T)\mathrm{d}T\,\mathrm{d}t\ , \tag{3-6}$$

where the interannual surface temperature $T_s(t)$ is approximated by means of the interannual air temperature T_a and the n-factors such that

$$T_s(t) = \begin{cases} n_{fr}T_a(t),\ T_a < 0 \\ n_{th}T_a(t),\ T_a \geq 0 \end{cases} \tag{3-7}$$

The interannual air temperature, in turn, is defined by the sinusoidal formula

$$T_a(t) = \bar{T}_a + A_a \sin\frac{2\pi t}{t_y}. \tag{3-8}$$

In Model B, used in Brandefelt et al. (2013), TO is implemented to the ground-surface temperature boundary condition such that surface temperature in Equation 3-1 is reduced by the amount of TO. In Model A, used in Hartikainen et al. (2010), zero TO is applied. The other boundary conditions are described in Section 3.3.2.

3.1.3 Numerical method

The numerical method is described in Hartikainen et al. (2010). It is based on the finite element method and adaptive time stepping algorithm. The coupled nonlinear equations are linearised by using the Newton-Raphson method (Mikkola and Hartikainen 2001, 2002), and the resulting linearised equation system is solved iteratively by using the finite element research code by Kouhia (1999).

3.1.4 Model domain and time frame

The 2D model domain encompasses an approximately 26 km long and 10 km deep vertical profile, aligned in the direction of the inclined DH-GAP04 bedrock borehole (Claesson Liljedahl et al. 2016) and is thereby oriented in a NNE–SSW direction (Figure 3-1). Note that, in order to cover the full widths of the two adjacent outlet glaciers, the model domain is about 9 km longer than that the 15 km long profile used for the Forsmark simulations in Hartikainen et al. (2010) and Brandefelt et al. (2013). This difference is however of no importance for the resulting bedrock temperatures used in the model evaluation.

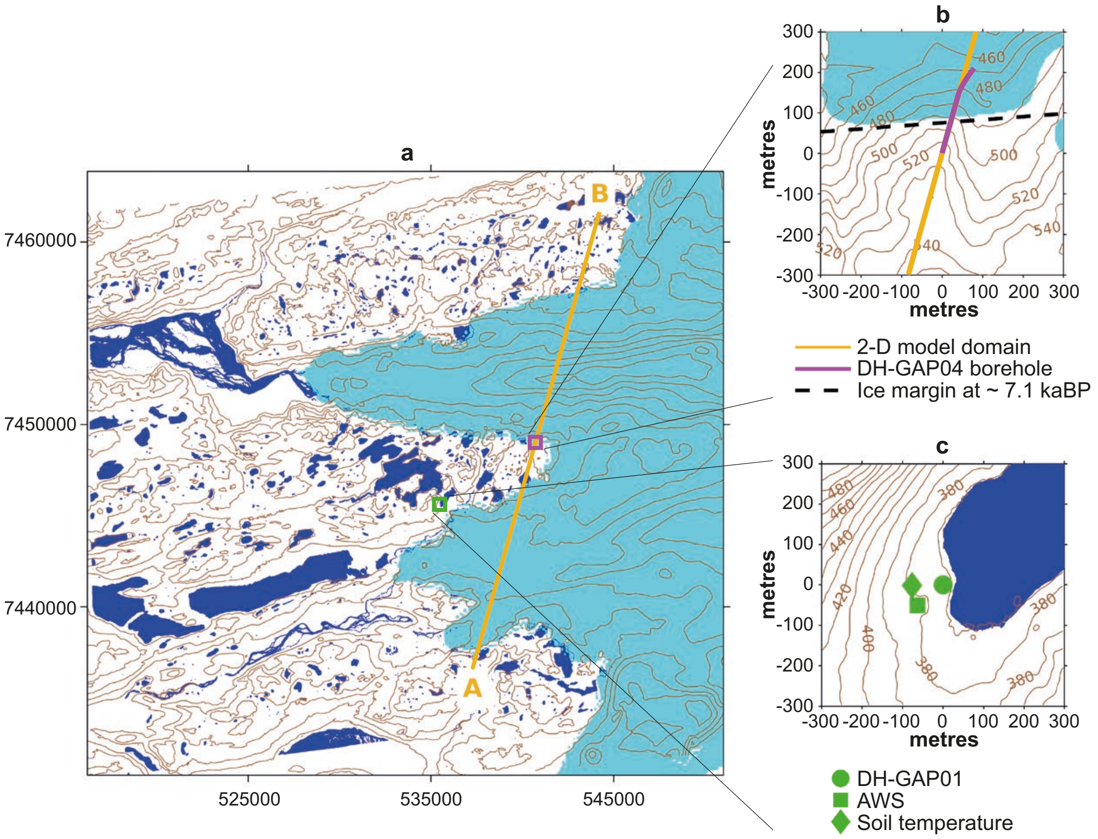

Figure 3-1. a) location of the 2D permafrost model domain (yellow line), the soil temperature measurement (STM) site (green square) and the DH-GAP04 drill site (pink square) on the map of the GAP site. Lakes are shown in blue and the ice-sheet in cyan. b) map view of the DH-GAP04 bedrock borehole (magenta line), inclined to NE, in the same direction as the 2D model domain. c) location of the STM site (green diamond), AWS (KAN_B) (green square) and DH-GAP01 bedrock borehole (green circle) close to the 'Talik lake' (blue). Contour lines (brown) in all panels depict the topography of the ground surface, also below the ice-sheet. Location of the ice margin around 7.1 ka BP is based on the results by Levy et al. (2018).

The model domain consists of a soil layer and bedrock (Figure 3-2). At the DH-GAP04 site (Figure 2-5), the soil thickness in the soil model (Appendix A3) is typically around 20 m except locations close to the ice-sheet margin, where the soil thickness may be up to 60 m. The upper part of the bedrock is divided into seven 100-m thick layers with prescribed material properties based on site data (Section 3.2). For the lower part of the bedrock, with no site data, average material properties of the site data are assigned.

In addition, the soil temperatures measured at the STM site is used for the evaluation of the surface models. It is located close to the DH-GAP01 borehole and the 'Talik lake' (Figure 2-3 and 3-1).

The modelled time frame covers the last glacial cycle, with simulations starting at 104 ka BP and ending at the present day. For the study area, the timing of ice-sheet coverage in the area during this period has been deduced from ice-sheet modelling (see further Section 3.2.1); this comprises a period of ice-sheet coverage between 104 and 7 ka BP, an ice-free period between 7 and 0.5 ka BP and a readvance of the GrIS during approximately the last 1 000 years BP to the present position.

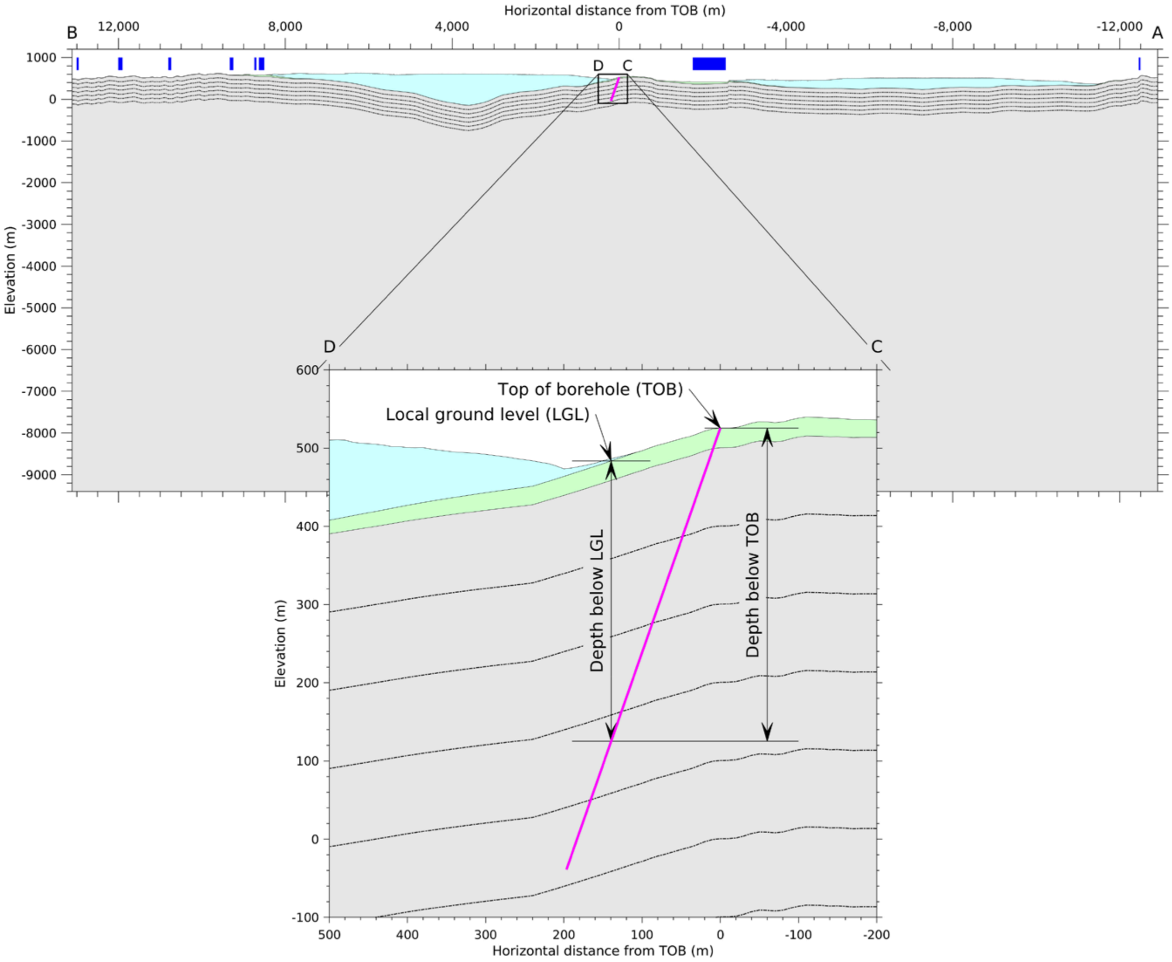

Figure 3-2. *Vertical extent of the 2D model domain. The bedrock is shown in grey, the soil layer in green and the ice-sheet in cyan. The seven 100-m thick rock layers are depicted by black lines. The DH-GAP04 bedrock borehole is shown in magenta. The blue bars above the model domain show the location of lakes. The two depth measures, depth below the local ground level (LGL) and depth below top of borehole (TOB), are used for presenting results along the borehole. Note that the reference location for the depth below local ground level (LGL) varies along the length of the borehole, i.e. the measure gives the local depth below the sloping ground surface along all parts of the borehole. Also note that the soil layer is too thick in the model, see the text.*

3.2 Input data

The input data consist of basal ice temperature, basal ice condition and ice-sheet thickness for the glacial conditions, Middle and Late Holocene air temperature, topographic wetness index describing the surface moisture conditions, water bodies as well as thermal and hydrological properties of bedrock and soil cover, geothermal heat flow and initial salinity concentration of groundwater. The data are based on field measurements, modelling results and reviewed literature, see below.

3.2.1 Surface properties and conditions

Glacial conditions

Time series of basal ice temperature and ice-sheet thickness of the last glacial cycle, shown in Figure 3-3, are derived from two simulations of the GrIS using the thermomechanical ice-sheet model SICOPOLIS. For a description of the SICOPOLIS model, see Greve (1997) and Greve et al. (2011). The simulations are hereafter referred to as the *reference* and *sensitivity* SICOPOLIS simulations, and they use different representations of the geothermal heat flow as boundary condition (Appendix A1). The results from the SICOPOLIS simulations indicate that the site is ice-covered for the entire glacial cycle except for a short period between 7 ka BP and present-day (Figure 3-3). The last readvance of the GrIS is estimated to have taken place between 1 800 and 200 years BP (Willemse et al. 2003, Young and Briner 2015, Levy et al. 2018). Using the results by Levy et al. (2018), we estimate that approximately the first third of the angled DH-GAP04 borehole projection to the surface has been ice free since 7.1 ka BP (Figure 3-1), whereas the middle third was exposed later than 200 years BP. During the readvance the ice-sheet is assumed to reach the position, surface elevation and thickness of the present-day ice-sheet (Claesson Liljedahl et al. 2016, Harper et al. 2016). The basal ice temperature data are used to construct the initial surface boundary conditions during the ice-covered periods of the last glacial cycle.

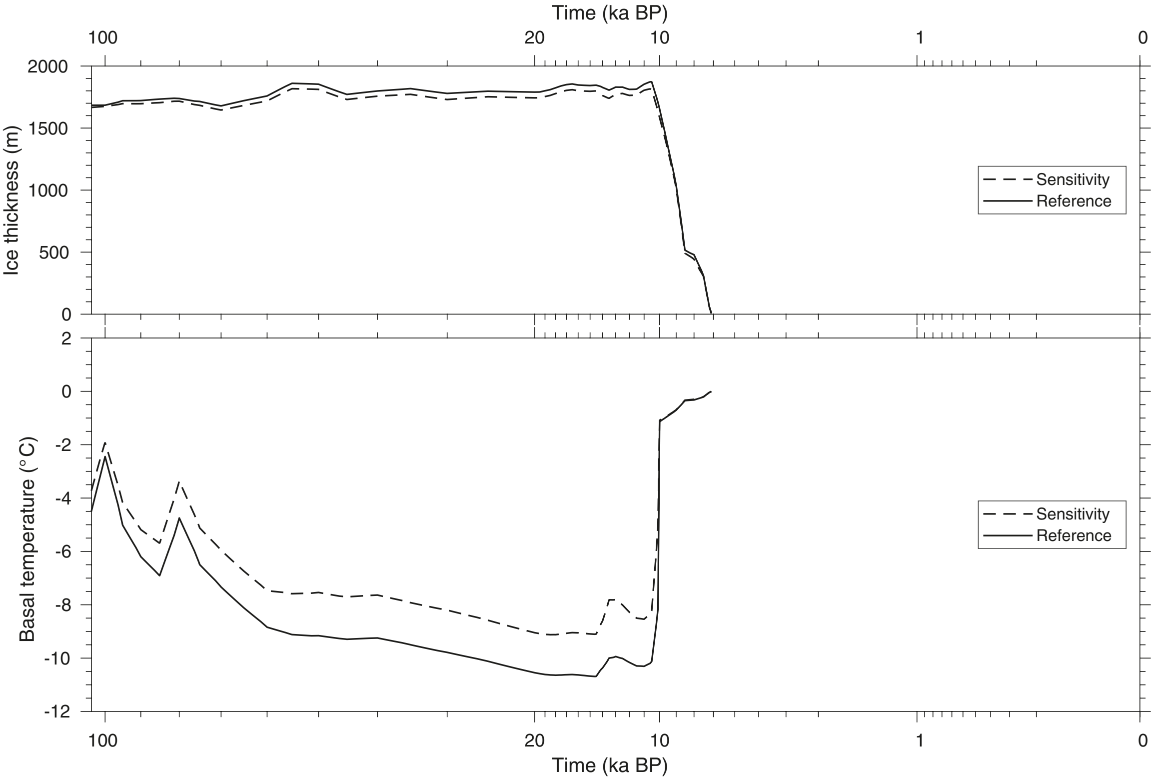

Figure 3-3. *Evolution of ice thickness and basal temperature over the DH-GAP04 borehole for the reference and sensitivity SICOPOLIS simulations (using different geothermal heat flow) during the glacial period (104–7 ka BP). For the time axis the exponential scale* $t^{1/3}$ *is used.*

There is a large uncertainty associated with the last glacial cycle air temperature used as forcing in the SICOPOLIS simulations (see Appendix A1). The air temperature reconstructions introduced for the last 7 ka in the next section indicate a warmer climate and thereby higher air temperature than that used in the SICOPOLIS simulations for the same period (Figure 3-4). Higher air temperatures than used in the simulations can result in increased basal temperatures, and thus higher MAGT.

Air temperature and precipitation over the last 7 ka

The air temperature input data are used to construct the ground surface temperature for the last 7 ka (approximately corresponding the Middle and Late Holocene) for vegetated and barren conditions, i.e. corresponding to the ice-free period between 7 ka BP and present-day in Figure 3-3. In this study, two air temperature reconstructions are used (Vinther et al. 2009, Kobashi et al. 2017), described in detail in Appendix A2.1. The resulting air temperatures (100-year averages) for the DH-GAP01 site are presented in Figure 3-4.

Based on the MAAT from the Kangerlussuaq and KAN_B (DH-GAP01 drill site) weather station (Appendix A2.1) and on the 1.6 m air temperature data from the STM sites at the DH-GAP01 and DH-GAP03 drill sites (Appendix A2.3), the annual lapse rate (vertical component of air temperature gradient) can vary between −0.9 and −1.5 °C km^{-1} at the GAP site. This implies that the present-day air temperature at the DH-GAP04 site can be 0.2–0.3 °C lower than that at the DH-GAP01 site. Along the 2D model domain with the bed elevation variation between −145 and 620 m and the −1.5 °C km^{-1} lapse rate, the air temperature can vary from +0.8 to −0.4 °C from the air temperature at the DH-GAP01 drill site at the 380 m elevation. However, without information on the present-day and Middle and Late Holocene local climate at the DH-GAP04 site, in combination with limited information on the lapse rate at the GAP site, the air temperature reconstructions constructed for the DH-GAP01 site is used for the 2D model domain.

The Holocene precipitation is poorly constrained. Records provide strong evidence for greatly reduced effective moisture during the Middle Holocene (7.1–5 ka BP) relative to the present day, whereas the Late Holocene precipitation remains vague (Briner et al. 2016). Nevertheless, the low and high precipitation variants with 40 and 280 mm annual precipitations, respectively, are assumed to provide a suitable precipitation range for the last 7 ka.

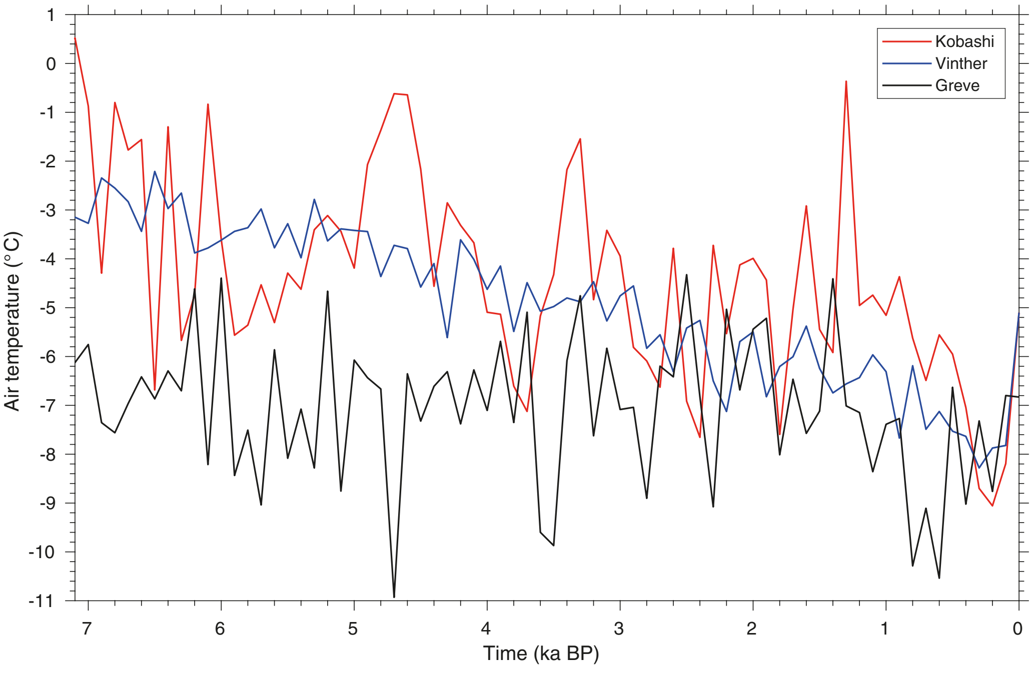

Figure 3-4. *Reconstructed 100-year average MAAT for the last 7 ka based on d^{18}O proxy ice-core records (Vinther et al. 2009) (blue) and argon and nitrogen isotope proxy ice-core records (Kobashi et al. 2017) (red). The MAAT at 500 years intervals used in the SICOPOLIS simulations (Greve et al. 2011), downscaled to the DH-GAP01 site, is also shown (black).*

Topographic wetness index

The topographical wetness index (TWI) is used to map the *n*-factors to the ground surface along the 2D model domain by calculating the likelihood for soil saturation as a function of specific catchment area and local ground surface slope (Beven and Kirkby 1979), see also Hartikainen et al. (2010). These calculations are presented in Appendix A2. The resulting TWI values are related to the surface moisture conditions such that the values less than 10.9, between 10.9 and 13.2 and larger than 13.2 represent dry, fresh-moist and wet surface conditions, respectively (Hartikainen et al. 2010).

The distribution of TWI and the corresponding surface moisture conditions at the DH-GAP01 and DH-GAP04 bedrock drill sites with the presence of ice-sheet and no ice-sheet are given in Figure 3-5, see also Appendix A2.2. The results illustrate clearly that TWI yields predominantly dry surface conditions for the GAP site. Fresh-moist and wet conditions occur merely in narrow zones and mainly in depressions (Figures A2-6 and A2-7). Patches of fresh-moist surface conditions are found at the DH-GAP01 and DH-GAP04 drill sites, where even wet surface conditions can be detected in front of the ice sheet (Figure 3-5).

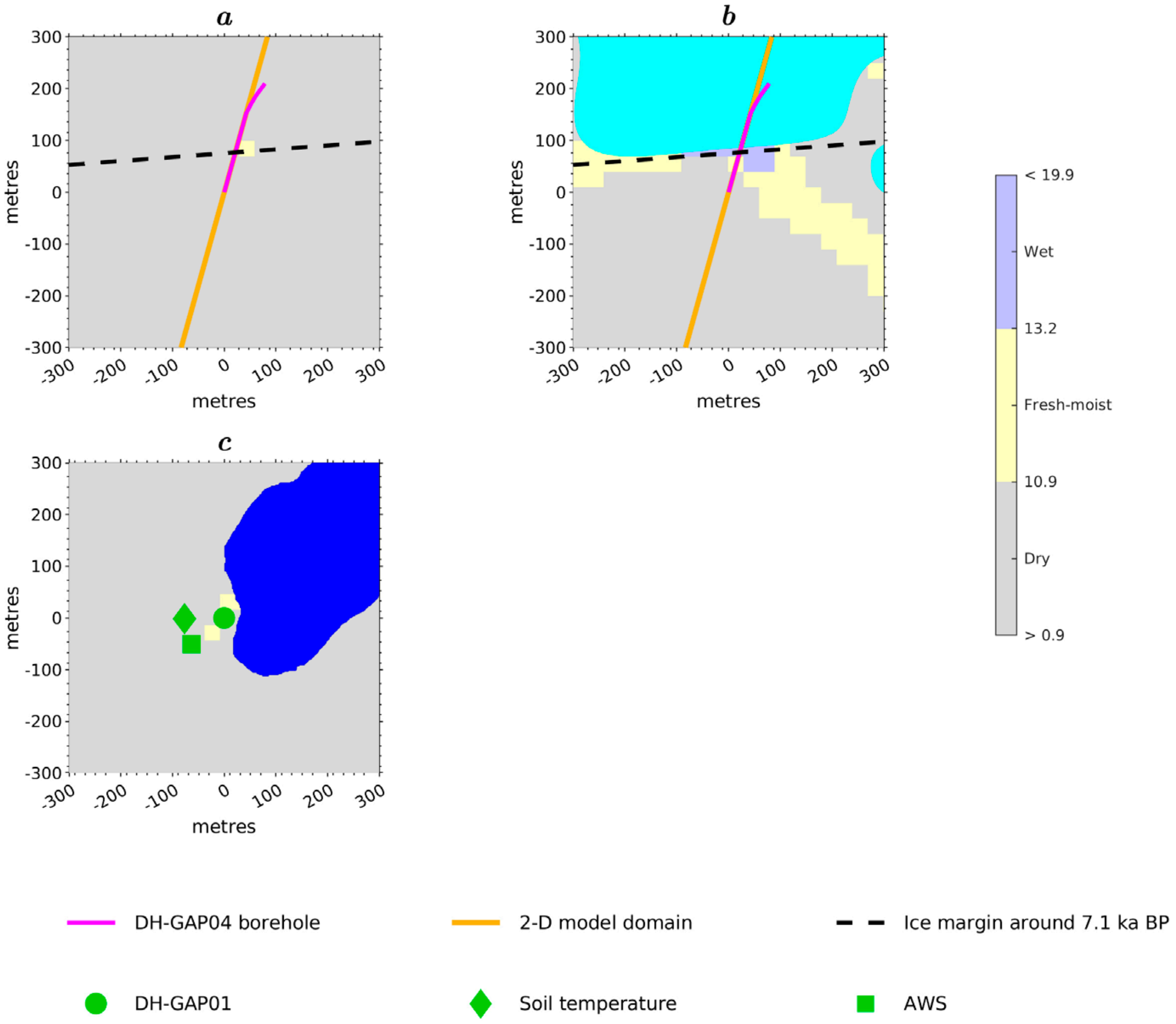

Figure 3-5. *Topographic wetness index (TWI) and the corresponding surface moisture condition for the DH-GAP04 site with an absence (a) and presence (b) of ice-sheet, and for the ice-free DH-GAP01 site (c). The locations of the sites are shown in Figure 3-1. Location of the ice margin around 7.1 ka BP is based on the results by Levy et al. (2018).*

Water bodies

Water bodies influence the thermal and hydraulic surface boundary conditions. The input data include the location and extent of water bodies (proglacial lakes and meltwater lakes at the ice-sheet margin), which are extracted from the soil map shown in Figure 3-2 and in Figure A3-9 and A3-10 (Appendix A3.3). It is assumed that the lakes and meltwater lakes have maintained their present positions and extents since the deglaciation. The variation in the extent of lakes has a negligible effect on the bedrock temperatures at the DH-GAP04 drill site, since the nearest lake is located 1 800 m from the site.

3.2.2 Subsurface properties and conditions

Material properties of bedrock and soil cover

Material properties of the bedrock are described in Appendix A3.2. The hydraulic conductivity and soil properties are adopted from the Forsmark site (Hartikainen et al. 2010) due to the lack of data for these parameters for the DH-GAP04 site. The hydraulic conductivity is assumed to be the same to the depth-dependent hydraulic conductivity of the rock mass at Forsmark, the site in south-central Sweden studied in Hartikainen et al. (2010), see Chapter 1. This is motivated by the similar type of crystalline bedrock at the sites, and by the overall purpose of evaluating the permafrost model as used at Forsmark site. The 100 metre-average values for the rock layers shown in Figure 3-2 are presented in Table 3-4.

The single layered soil cover consisting of till, glaciofluvial sediments, Eolian sand or gyttja is based on the soil map described in Appendix A3.3. The soil types are assumed to have similar thermal and hydraulic properties as the soil cover at the Forsmark site (Hartikainen et al. 2010). Considering that the effect of convective heat transfer on the permafrost development has proved to be negligible (Hartikainen et al. 2010), the hydraulic properties can be assumed to have a negligible effect on the permafrost development as well. The thermal and hydrological soil properties are presented in Table 3-5. The soil thickness at the DH-GAP04 drill site is overestimated in the soil model. The uncertainty in soil thickness is handled by a dedicated sensitivity analysis on soil thickness (see Section 3.3.3).

Table 3-4. Thermal and hydrological properties of rock. The average values for the 0–700 m depths are adopted for depths larger than 700 m (i.e. for > 700 to 9 400 m).

		Rock layer							
Parameter	**Unit**	**0–100 m**	**100–200 m**	**200–300 m**	**300–400 m**	**400–500 m**	**500–600 m**	**600–700 m**	**> 700 m**
Thermal conductivity	$W\ m^{-1}\ K^{-1}$	2.42	2.39	2.45	2.24	1.77	2.33	2.28	2.28
Specific heat capacity	$J\ kg^{-1}\ K^{-1}$	682	671	673	676	687	682	678	678
Radiogenic heat production	$W\ m^{-3}$	3.0×10^{-7}	3.0×10^{-7}	3.0×10^{-7}	3.0×10^{-7}	3.0×10^{-7}	3.0×10^{-7}	3.0×10^{-7}	3.0×10^{-7}
Bulk density	$kg\ m^{-3}$	3 218	3 229	2 786	2 736	2 768	2 771	2 935	2 935
Total porosity	%	0.43	0.54	0.43	0.54	0.95	0.62	0.58	0.58
Horizontal hydraulic conductivity	$m\ s^{-1}$	10^{-5}	5.0×10^{-6}	10^{-8}	10^{-11}	10^{-11}	10^{-11}	10^{-11}	10^{-11}
Vertical hydraulic conductivity	$m\ s^{-1}$	10^{-7}	5.0×10^{-8}	10^{-9}	10^{-11}	10^{-11}	10^{-11}	10^{-11}	10^{-11}
Parameters for the unfrozen groundwater content function									
χ_0	-	0.1	0.1	0.1	0.1	0.1	0.1	0.1	0.1
e_s	-	0.006	0.006	0.006	0.006	0.006	0.006	0.006	0.006

Table 3-5. Thermal and hydraulic properties of soil cover. The data is from the Forsmark site, see Hartikainen et al. (2010).

		Soil type			
Parameter	**Unit**	**Gyttja**	**Eolian sand**	**Glaciofluvial sediments**	**Till**
Thermal conductivity	$W\ m^{-1}\ K^{-1}$	0.6	2.19	1.0	2.14
Heat capacity	$J\ m^{-3}\ K^{-1}$	4.2×10^6	2.7×10^6	3.4×10^6	2.5×10^6
Bulk density	$kg\ m^{-3}$	46.4	1800	900	2000
Total and kinematic porosity	%	50	35	45	25
Hydraulic conductivity	$m\ s^1$	3.0×10^{-7}	1.5×10^{-4}	1.5×10^{-8}	1.5×10^{-6}
Parameters for the unfrozen groundwater content function					
χ_0	-	0.1	0.1	0.9	0.6
e_s	-	0.006	0.006	0.004	0.002

Geothermal heat flow

The measured vertical geothermal heat flow is based on the temperature measurements made in the DH-GAP04 borehole over the period September 2016 – August 2017 (Claesson Liljedahl et al. 2021). The heat flow is determined as a product of the vertical component of the measured temperature gradient and thermal conductivity. Both factors are calculated as 50 metres running means (Appendix A3.2).

The geothermal heat flow at the bottom of the model domain at the −9400 m elevation (10 km depth) is undisturbed by the long-term climate change at the ground surface. In the absence of geothermal heat flow data from several km depths, the geothermal heat flow at the bottom of the model domain is described by a near surface *palaeoclimatically corrected* 200 m average vertical geothermal heat flow of 37.8 mWm^{-2}. This palaeoclimatically corrected geothermal heat flow value was obtained from the measured present-day average vertical geothermal heat flow of 28.0 mWm^{-2} and an average palaeoclimatic correction of 9.8 mWm^{-2}, both values calculated for the 280–480 m depth interval (depth below LGL), see Appendix A3.2.9. The palaeoclimatic correction is computed by using a unidimensional heat conduction equation and glacial cycle (104–0 ka BP) site-average surface temperatures based on the basal ice temperature history of the SICOPOLIS simulations (Section 3.2.1, Appendix A1) during the glacial period (104–7 ka BP) and the ground surface temperature history during 7–0 ka BP (Section 3.2.9, Appendix A3).

Initial salinity concentration of groundwater

Data on groundwater salinity concentration at the beginning of the last glacial cycle is not available. Therefore, due to the similar type of crystalline bedrock between the sites and the overall purpose of evaluating the permafrost model as used for the Forsmark site, the initial salinity concentration of groundwater at 104 ka BP is assumed to be similar with the initial salinity distribution in Hartikainen et al. (2010) corresponding to the ionic composition of the present-day groundwater at Forsmark.

3.3 Numerical simulations

3.3.1 Finite element mesh and temporal discretisation

The numerical implementation, including the spatial and temporal resolution, is identical to the ones used in the previous Forsmark studies (Hartikainen et al. 2010, Brandefelt et al. 2013). To this end, the model domain (Figure 3-2) is discretised by using an unstructured finite element mesh of linear triangle elements. The mean grid spacing varies from less than 1 m close to the ground surface to about 300 m at the bottom of the model domain. The material properties for the bedrock and soil cover are described in Section 3.2.2.

Time is discretised by using a time step of 500 years from the beginning (104 ka BP) until LGM (20 ka BP) and 100 years from LGM until the present. The adaptive time integration scheme controls the time step depending on the convergence of the numerical solution such that it can be shorten to around one year from the 100- or 500-year default values. The annual time integral for TO in Equation 3-6 is calculated numerically by using one day long time intervals.

3.3.2 Boundary and initial conditions

For ground surface locations covered by the ice-sheet, the ground surface temperature is set equal to the basal ice temperature. Since the deformations of the soil and bedrock are omitted, the surface groundwater pressure corresponds to the atmospheric pressure when the ice-sheet is cold-based, whereas it is set equal to the hydrostatic pressure corresponding to the weight of the overlying ice when the ice-sheet is warm-based. For vegetated or barren locations, the surface temperature is set to the modelled MAGST (described in Section 3.1.2) and the surface groundwater pressure is set to correspond to the atmospheric pressure. For locations covered by water bodies, the ground surface temperature is set to a constant value of +4 °C and the atmospheric surface groundwater pressure is increased by a hydrostatic pressure of 98.1 kPa corresponding to an approximate average water depth of 10 metres for the lakes on the model domain. The groundwater salinity concentration is fixed to the constant value of 0.04 mass-%.

At the bottom of the model domain, the heat flow is set to 35.9 ± 2.0 $\mathrm{mWm^{-2}}$. It is calculated from the palaeoclimatically-corrected near surface vertical geothermal heat flow of 37.8 ± 2.0 $\mathrm{mWm^{-2}}$ (see Section 3.2.2, Appendix 3.2.8 and Appendix 3.2.9) by removing the effect of the radiogenic heat production of the 10 km-thick rock mass amounting to 1.9 $\mathrm{mWm^{-2}}$. The groundwater flow is zero at the bottom of the domain and the salt diffusion-dispersion flow has a constant value of 3 mm $\mathrm{a^{-1}}$ representing the dissolution of soluble salts from the rock matrix (Hartikainen et al. 2010). Both side boundaries are set to be no-flow boundaries.

The initial conditions for MAGT and groundwater pressure are obtained as a solution of a stationary heat conduction and groundwater flow problem for given mean glacial-cycle surface temperature, constant surface groundwater pressure and initial salinity concentration of the groundwater. Based on the information that the climate has been evolving during the past glacial cycles in a more or less similar manner, the resulting mean glacial-cycle surface temperature evolves slowly. Therefore, the mean glacial-cycle surface temperature was determined by using the results of SICOPOLIS simulations and the ground surface temperature reconstructions for the last 7 ka (Section 3.2). The surface groundwater pressure is set to the atmospheric pressure. The initial salinity concentration of groundwater is assumed to be similar with the initial salinity distribution in Hartikainen et al. (2010) (Section 3.2.2).

3.3.3 Test cases

The impacts of surface and subsurface conditions on the evolution of permafrost and frozen ground are investigated in various test cases covering plausible variations of the climate and basal ice-sheet conditions as well as uncertainties identified in previous studies (SKB 2006, Hartikainen et al. 2010).

The test cases are organised according to six relevant factors including i) MAAT, ii) precipitation, iii) glacial conditions, iv) timing of the last ice-sheet readvance, v) geothermal heat flow and vi) soil thickness as follows:

Middle and Late Holocene MAAT

V. Middle and Late Holocene MAAT (Figure 3-4) is based on the proxy ice-core records of δ^{18}O by Vinther et al. (2009).

K. Middle and Late Holocene MAAT (Figure 3-4) is based on the proxy ice-core records of argon and nitrogen isotopes by Kobashi et al. (2017).

Precipitation

L. The low precipitation case assumes that low precipitation with the maximum monthly precipitation of 5 mm in summer and 1 mm in winter dominates throughout the Holocene.

H. The high precipitation case assumes that the present-day precipitation at the DH-GAP01 site (Johansson et al. 2015a) prevails during the entire Holocene.

Glacial conditions

G. Glacial conditions are based on the reference SICOPOLIS simulation, see Section 3.2.2 and Appendix A1.

Gbh. The spatial distribution of the geothermal heat flow used in the SICOPOLIS simulation (based on Greve et al. 2019, see Section 3.2.2) assumes relatively low values, comparable to the measured value at GAP, for a large area surrounding the GAP site (Figure A1-1). Measurements of the geothermal heat flow across Greenland are however rare (e.g. Greve et al. 2019, Colgan et al. 2022). Studies of HFD in Fennoscandia have shown a large spatial variability in HFD (Näslund et al. 2005), both on a local and regional scale. Given the similar geological settings between Fennoscandia and Greenland, there is therefore a large uncertainty related to the prevailing geothermal heat flux within a few hundreds of km around the GAP site. In particular, the geothermal heat flux upstream (east of) the GAP site is important. If the HFD is underestimated in this region in the ice-sheet simulation based on Greve et al. (2019), see Section 3.2.2, the ice advected from this area in over the GAP site would be too cold and the simulated bedrock temperatures would be affected accordingly. Therefore, a sensitivity case with higher HFD in this upstream area was constructed, allowing for higher basal temperatures and warmer ice from this area to be advected towards the GAP site. Hence, in this sensitivity case, we investigate this upstream effect on the GAP MAGT by using an alternative map of geothermal heat-flux in SICOPOLIS, as described in Appendix A1.

Gbt. There is a large uncertainty associated with the last glacial cycle air temperature used as forcing in the SICOPOLIS simulations (Appendix A1). A warmer climate than used in the simulations may result in increased basal temperatures, and thus a higher MAGT. Therefore, in this sensitivity case, the subglacial temperature of the reference SICOPOLIS simulation is increased by the amount of the estimated uncertainty of 2.5 °C in the glacial MAAT but never above the pressure melting point of ice. This is estimated from the difference in the downscaled MAAT used in the SICOPOLIS simulations and the above two MAAT reconstructions for the last 7 ka (Figure 3-4).

Timing of the last ice-sheet readvance

200. The ice-sheet readvances into approximately the present-day location by the end of the Little Ice Age. This is considered to be the latest plausible readvance based on Willemse et al. (2003).

500. The ice-sheet readvances into proximity of the present-day location at around 500 years BP, i.e. at the onset of the Little Ice Age, based on the SICOPOLIS simulations.

800. The ice-sheet readvances into proximity of the present-day location at around 800 years BP, i.e. before of the Little Ice Age, based on Young and Briner (2015).

1 800. The ice-sheet readvances into proximity of the present-day location at around 1 800 years BP. This assumes the earliest plausible readvance according to Young and Briner (2015).

Geothermal heat flow

Min. A geothermal heat flow of 33.9 mWm^{-2} at the bottom of the model domain (at 10 km depth), based on a minimum palaeoclimatic correction of 7.8 mWm^{-2} for the 200 metres average geothermal heat flow between 280 and 480 metres depth (Section 3.2.3 and Appendix A3.2.9).

Mean. A geothermal heat flow at the bottom of the model domain (at 10 km depth), based on the measured present-day vertical geothermal heat flow of 28.0 mWm^{-2} calculated for the depth interval between 280 and 480 metres by using the mean annual borehole temperature for September 2016 – August 2017 and the mean palaeoclimatic correction of 9.8 mWm^{-2} based on the 32 surface temperature cases.

Max. A geothermal heat flow of 37.9 mWm^{-2} at the bottom of the model domain (at 10 km depth), based on a maximum palaeoclimatic correction of 11.8 mWm^{-2} for the 200 metres average geothermal heat flow between 280 and 480 metres depths (Section 3.2.3 and Appendix A3.2.9).

Soil thickness

S100. The soil cover is based on the soil map and model seen in Figures A3-9 and A3-10.

S10. The thickness of the soil cover based on the soil model is reduced to 10 % everywhere by rescaling the soil thickness of the soil model (Figure A3-10) by the factor 0.1. From observations around the DH-GAP04 borehole, it can be concluded that the soil model (Figure A3-10) considerably overestimates the soil thickness in this area (see Appendix A3.3.2). Since this area is used for a comparison between measured bedrock temperatures from the borehole and corresponding modelled bedrock temperatures, this sensitivity case is constructed for the model evaluation.

Combining the two MAAT cases (V, K), two precipitation cases (L, H), two glacial condition cases (G, Gbh) and two cases for the timing of the last ice-sheet readvance (500, 800) together with the mean geothermal heat flow case (Mean) and the soil thickness case based on the soil map (S100) composes a core of 16 test cases. An additional 16 test cases are formed to investigate further uncertainties related to the Weichselian glacial conditions (Gbt), timing of the last readvance of GrIS (200, 1 800), geothermal heat flow (Min, Max) and soil thickness (S10). In the evaluation of the permafrost model performance for safety assessment purposes, overestimated modelled bedrock temperatures are potentially more critical than underestimated ones (Chapter 1). In order to be pessimistic, the objective of these additional cases is therefore primarily to assess uncertainties that may result in warmer conditions than in the 16 cases described above.

All test cases are evaluated by both Models A and B. As described in the introductory paragraphs of Section 3.1, the difference between the models is that Model B accounts for nonzero thermal offset (TO), where zero TO is used in Model A. All test cases are summarised in Table 3-6.

Table 3-6. Test cases for the numerical simulations. 'Vinther', 'Kobashi' and 'Greve' refers to data based on the studies by Vinther et al. (2009), Kobashi et al. (2017) and Greve (2019) respectively. For further details see Section 3.3.3.

Case	**Middle and Late Holocene MAAT**		**Precipitation**		**Glacial condition**			**Last ice-sheet readvance timing (years BP)**				**Geothermal heat flow (mW m^{-2})**			**Soil thickness**	
	Vinther	Kobashi	Low	High	Greve	Modified Greve basal heat flow density	Modified Greve basal temperature	**200**	**500**	**800**	**1 800**	**Min** (33.9)	**Mean** (35.9)	**Max** (37.9)	**100 %** thickness	**10 %** thickness
V_L_G_500_Mean_S100	•		•		•				•				•		•	
V_L_G_800_Mean_S100	•		•		•					•			•		•	
V_L_Gbh_500_Mean_S100	•		•			•			•				•		•	
V_L_Gbh_800_Mean_S100	•		•			•				•			•		•	
V_H_G_500_Mean_S100	•			•	•				•				•		•	
V_H_G_800_Mean_S100	•			•	•					•			•		•	
V_H_Gbh_500_Mean_S100	•			•		•			•				•		•	
V_H_Gbh_800_Mean_S100	•			•		•				•			•		•	
K_L_G_500_Mean_S100		•	•		•				•				•		•	
K_L_G_800_Mean_S100		•	•		•					•			•		•	
K_L_Gbh_500_Mean_S100		•	•			•			•				•		•	
K_L_Gbh_800_Mean_S100		•	•			•				•			•		•	
K_H_G_500_Mean_S100		•		•	•				•				•		•	
K_H_G_800_Mean_S100		•		•	•					•			•		•	
K_H_Gbh_500_Mean_S100		•		•		•			•				•		•	
K_H_Gbh_800_Mean_S100		•		•		•				•			•		•	
K_L_Gbt_500_Mean_S100		•	•				•		•				•		•	
K_H_Gbt_500_Mean_S100		•		•			•		•				•		•	
V_L_G_200_Mean_S100	•		•		•			•					•		•	
V_L_G_1800_Mean_S100	•		•		•						•		•		•	
K_H_Gbt_200_Mean_S100		•		•			•	•					•		•	
K_H_Gbt_1800_Mean_S100		•		•			•				•		•		•	
V_L_G_500_Min_S100	•		•		•				•			•			•	
V_L_G_500_Max_S100	•		•		•				•					•	•	
V_L_Gbh_500_Min_S100	•		•			•			•			•			•	
V_L_Gbh_500_Max_S100	•		•			•			•					•	•	
K_H_G_500_Min_S100		•		•	•				•			•			•	
K_H_G_500_Max_S100		•		•	•				•					•	•	
K_H_Gbh_500_Min_S100	•			•		•			•			•			•	
K_H_Gbh_500_Max_S100		•		•		•			•					•	•	
V_L_G_500_Mean_S10	•		•		•				•				•			•
K_H_G_500_Mean_S10		•		•	•				•				•			•

4 Results

The permafrost models with zero TO (Model A) and nonzero TO (Model B) are used to simulate the thermal evolution of the ground from 104 ka BP until present (2010 AD) in the 2D model domain, aligned along the DH-GAP04 borehole, for the specified material parameters, initial conditions and boundary conditions described in Chapter 3. In addition, the present-day ground surface temperature and TO are simulated using the surface conditions from the STM site close to the 'Talik lake' (Johansson et al. 2015a). The main results for MAGST, TO, MAGT, unfrozen groundwater content, permafrost depth and the depth of perennially frozen ground together with the results for the groundwater pressure, flow and salinity concentration are presented in this chapter. Supplementary results are presented in Appendix A4.

4.1 Mean annual ground surface temperature (MAGST) and thermal offset (TO)

The present-day MAGST and TO are computed at the STM site (Figure 3-1). According to the TWI value of 7.4 (see Section 3.2.1), dry surface moisture conditions prevail at the site. When the precipitation acts on the surface moisture conditions through the *n*-factors (Section 3.1.2), the values for the low precipitation case (Table 3-1) and the high precipitation case (Table 3-3) together with the five-year average (2011–2015) of the air temperature average (−5.2 °C) from the STM site (Appendix A2.3) result in the MAGST and TO presented in Table 4-1. The measured values in the table are based on the soil temperature data that have been collected at 25 centimetres depth intervals down to 1.25 m depth during the period 2011–2015 by Johansson et al. (2015a). The surface values are obtained by extrapolation.

Further, MAGST and TO are calculated for the fresh-moist and wet ground surfaces that are found close to the STM site and at the DH-GAP04 site close to the ice-sheet margin (Figure 3-2). The results are presented in Table 4-2 and plotted in Figure 4-1 along the ground surface above the borehole. Values close to zero MAGST together with zero TO in Figure 4-1 represent the basal ice temperature at the pressure melting point of the overlying ice-sheet. With respect to the dry surface condition, the fresh-moist and wet zone above the borehole in front of the ice-sheet (Figure 3-5) yields elevated MAGST and decreased TO along the borehole towards the ice-sheet (Figure 4-1). In comparison to the dry area, the modelled present-day MAGST in the fresh-moist and wet zones is increased by ~0.5 °C and ~1.5 °C, respectively, whereas TO is reduced decimally (0.1–0.2 °C) (Table 4-2, Figure 4-1).

Table 4-1. Modelled and measured present-day MAGST and TO at the STM site close to DH-GAP01 associated with dry moisture condition and considering low and high precipitation cases.

Parameter	Unit	Modelled values		Measured values	
		Low precipitation	High precipitation	Mean	Standard deviation
MAGST	°C	−4.4	−3.5	−3.0	0.7
TO	°C	−0.8	−0.5	−0.5	0.5

Table 4-2. Modelled present-day MAGST and TO for fresh-moist and wet ground surfaces close to the STM site and above the borehole of DH-GAP04 close to the ice margin and considering low and high precipitation cases.

Parameter	Unit	Fresh-moist		Wet	
		Low precipitation	High precipitation	Low precipitation	High precipitation
MAGST	°C	−3.9	−3.0	−2.6	−1.9
TO	°C	−0.7	−0.4	−0.6	−0.3

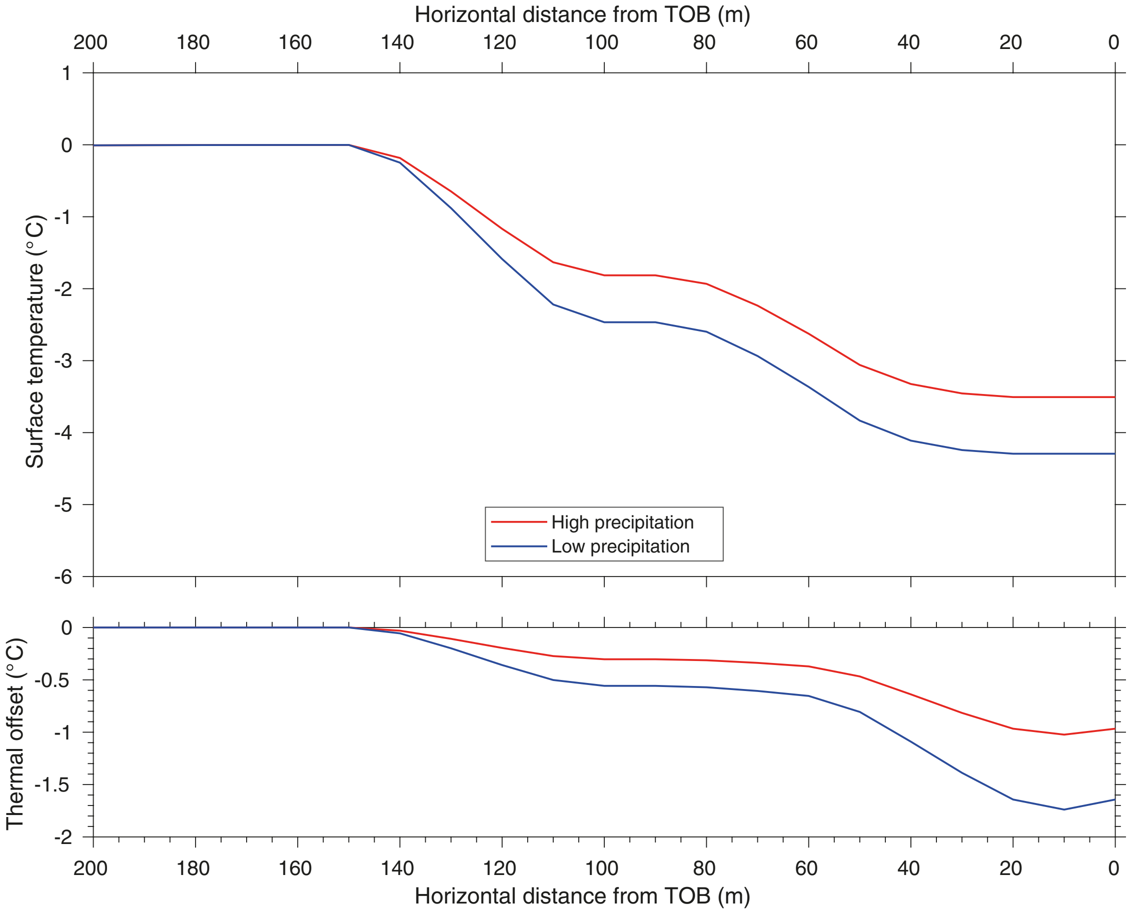

Figure 4-1. *Modelled present-day MAGST and TO along the ground surface over the borehole of DH-GAP04 for the high and low precipitation cases. TOB refers to "Top of Borehole".*

The evolution of MAGST and TO at the DH-GAP04 site during the glacial cycle (104–0 ka BP) is shown in in Figure 4-2. During the glacial period, the ground surface temperature is driven by the basal ice temperature, which after an initial transient warming cools down gradually until the onset of deglaciation at c 10 ka BP as shown in Figure 4-2. MAGST achieves its lowest glacial value of −10.7 °C at 14.1 ka BP with the reference SICOPOLIS simulation (Section 3.2.1) and −9.1 °C at 18.5 ka BP with the sensitivity SICOPOLIS simulation. The deglaciation phase starts at around 10.5 ka BP with rapid warming of the ground surface as the overlying ice-sheet turns from cold-based to warm-based (the base of the ice-sheet reaches the pressure melting point temperature over a period of 500 years). During the following 3 000 years, the ice-sheet stays warm-based until the deglaciation of the site at around 7 ka BP. Without seasonal freezing when ice covers the area, no active layer is created, and thereby TO is zero.

After the deglaciation, the ground surface is influenced directly by the prevailing climate, including the air temperature (Figure 3-4), and different precipitation and surface moisture conditions. Consequently, the ground surface cools gradually until the last readvance of the ice-sheet at 200–1 800 years BP when the drill site gets partially covered by the ice-sheet as the ice-sheet reaches its present-day position. From the last readvance until present, climate warms up and the ground surface reaches its current temperature. MAGST varies considerably in time and location, between 0 and −7 °C, depending on the air temperature and precipitation conditions (Figure 4-2). The maximum difference in MAGST in time is ~5 °C. On the ice-free land, seasonal freezing takes place creating active layer and thereby TO extending to ~−1 °C for the high precipitation case and to ~−1.5 °C for the low precipitation case.

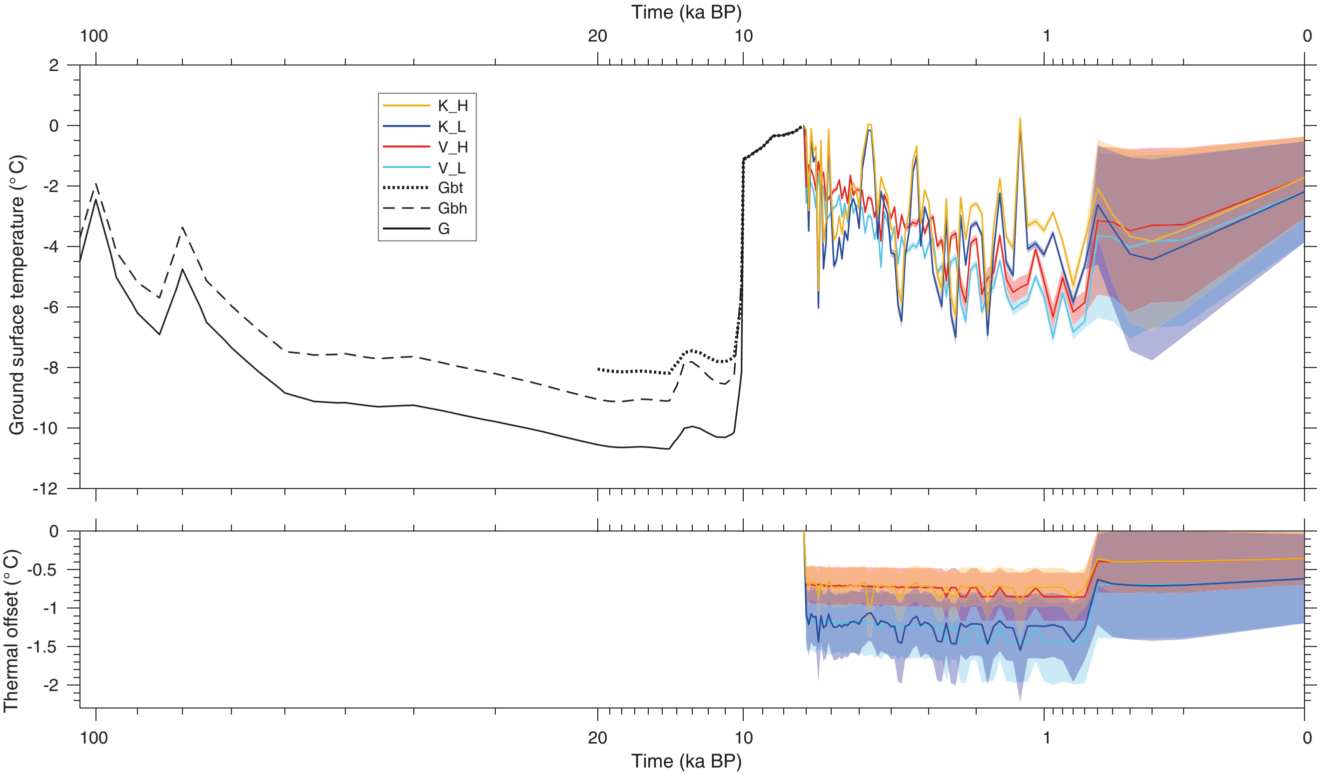

***Figure 4-2.** Evolution of MAGST and TO (calculated as a mean value along the projected DH-GAP04 borehole length on the ground surface) for the basal ice temperature histories G (Greve), Gbh (modified Greve basal heat flow density) and Gbt (modified Greve basal temperature) during the glacial period (104–7 ka BP) and for the V (Vinther) and K (Kobashi) air temperature cases, L (low) and H (high) precipitation cases and the last readvance of the GrIS case at 500 years BP during the last 7 ka (approximately Middle to Late Holocene). Solid lines show the mean and coloured areas the standard deviation for the 200 m horizontal length of the borehole (horizontal distance from TOB towards the ice-sheet).*

4.2 Thermo-hydro-chemical evolution of ground surface and bedrock

4.2.1 Glaciated period (104–7 ka BP)

At the initial state at 104 ka BP, the ground surface temperature is equal to the prescribed glacial cycle mean ground surface temperature of −6.3 °C and the ground is perennially frozen down to the depth of 440 m below LGL (495 m below TOB) and the permafrost (0 °C isotherm) extends to the depth of 450 m below LGL (505 m below TOB).

During the glacial period, when the ground surface cools down as a result of the basal ice temperature of the reference SICOPOLIS simulation (Figure 4-2), the perennially frozen ground develops down to a depth of 605 m below LGL (675 m below TOB) at 13.2 ka BP, whereas the permafrost reaches a depth of 625 m below LGL (700 m below TOB) just after the onset of deglaciation at around 9.8 ka BP (Figure 4-3). Correspondingly, for the basal ice temperature of the sensitivity SICOPOLIS simulation (Figure 4-2), the perennially frozen ground obtains a depth of 535 m below LGL (600 m below TOB) at 13.7 ka BP and the permafrost a depth of 550 m below LGL (615 m below TOB) at 13.8 ka BP (Figures 4-4, 4-5).

During the deglaciation phase, from around 10.5 to 7 ka BP, the ground warms up rapidly and the perennially frozen ground and permafrost degrade strongly, by 240 m for the reference SICOPOLIS simulation (Figure 4-3) and by 310 m for both the sensitivity SICOPOLIS simulation and the warm variant of the reference SICOPOLIS simulation (Figures 4-4, 4-5). The warming of the ground also results in a very strong reduction in geothermal heat flow, from 35 to 12 mWm^{-2} (see Figure A4-1, in Appendix 4).

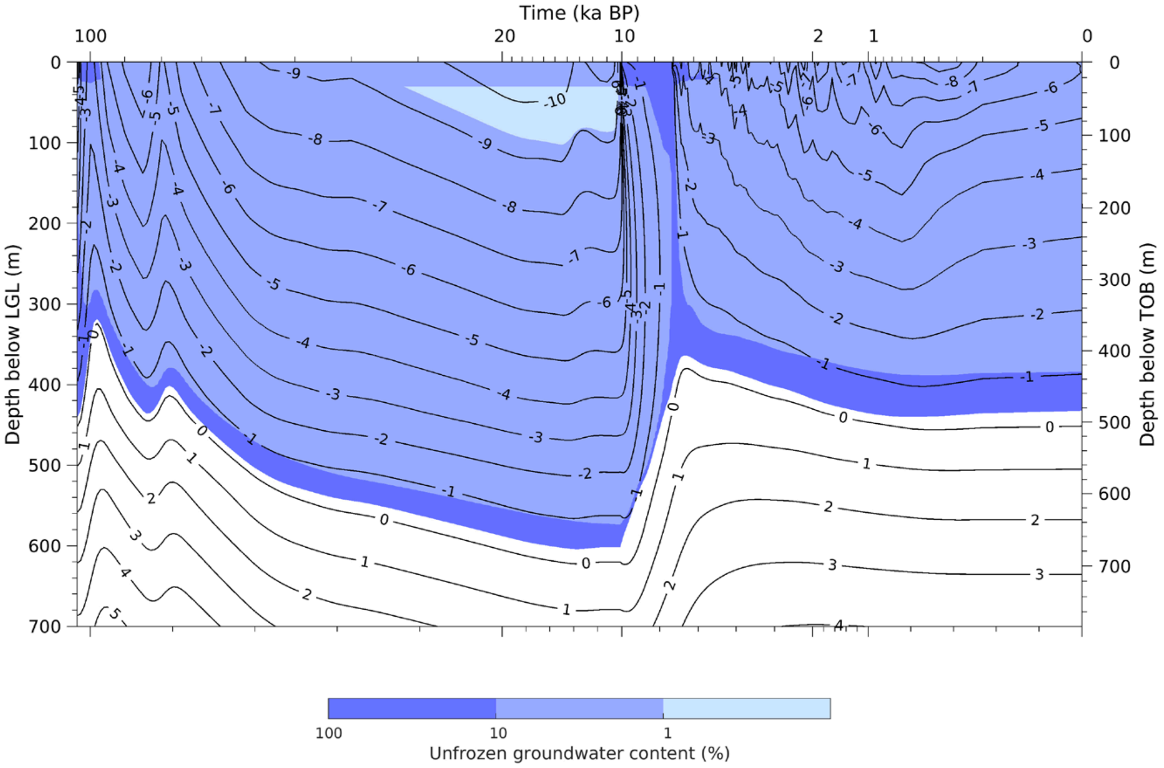

__Figure 4-3.__ Evolution of MAGT (line contours) and unfrozen groundwater content (filled areas) at the DH-GAP04 site during period 104–0 ka BP for the test case V_L_G_500_Mean_S100 with Model B. The perennially frozen ground is illustrated by the blue shadings.

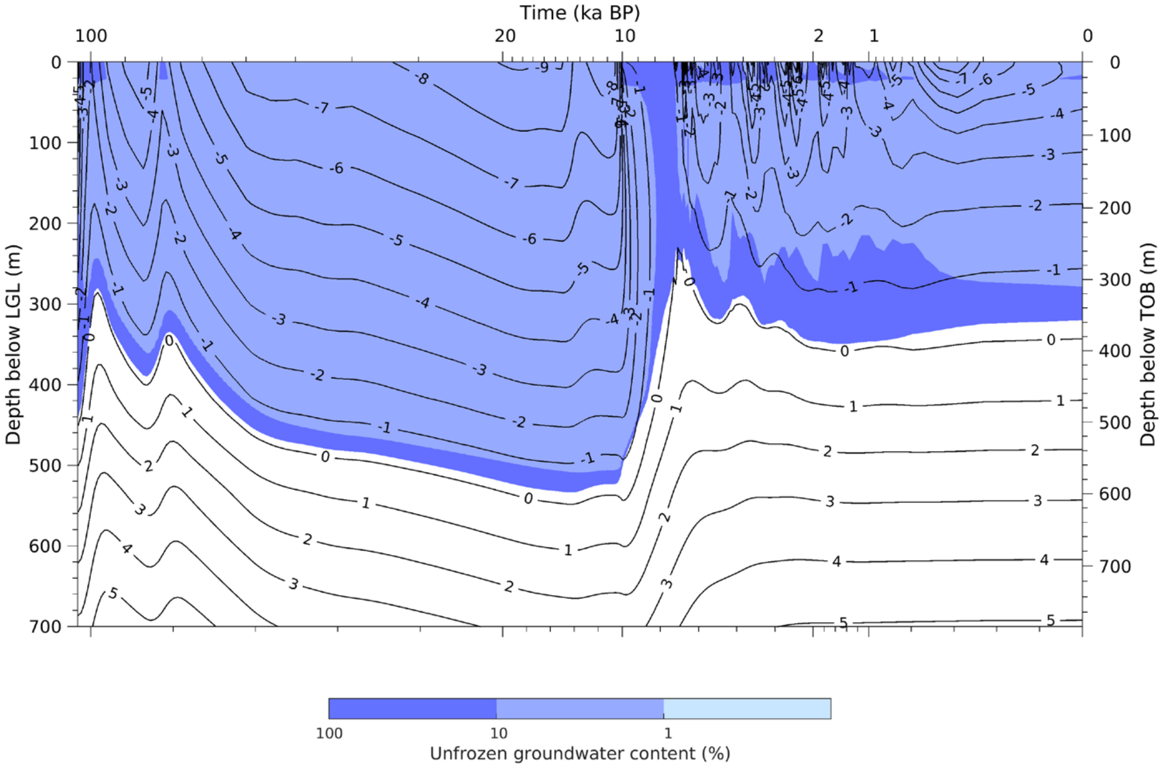

__Figure 4-4.__ Same as Figure 4-3, but for the test case K_H_Gbh_500_Mean_S100.

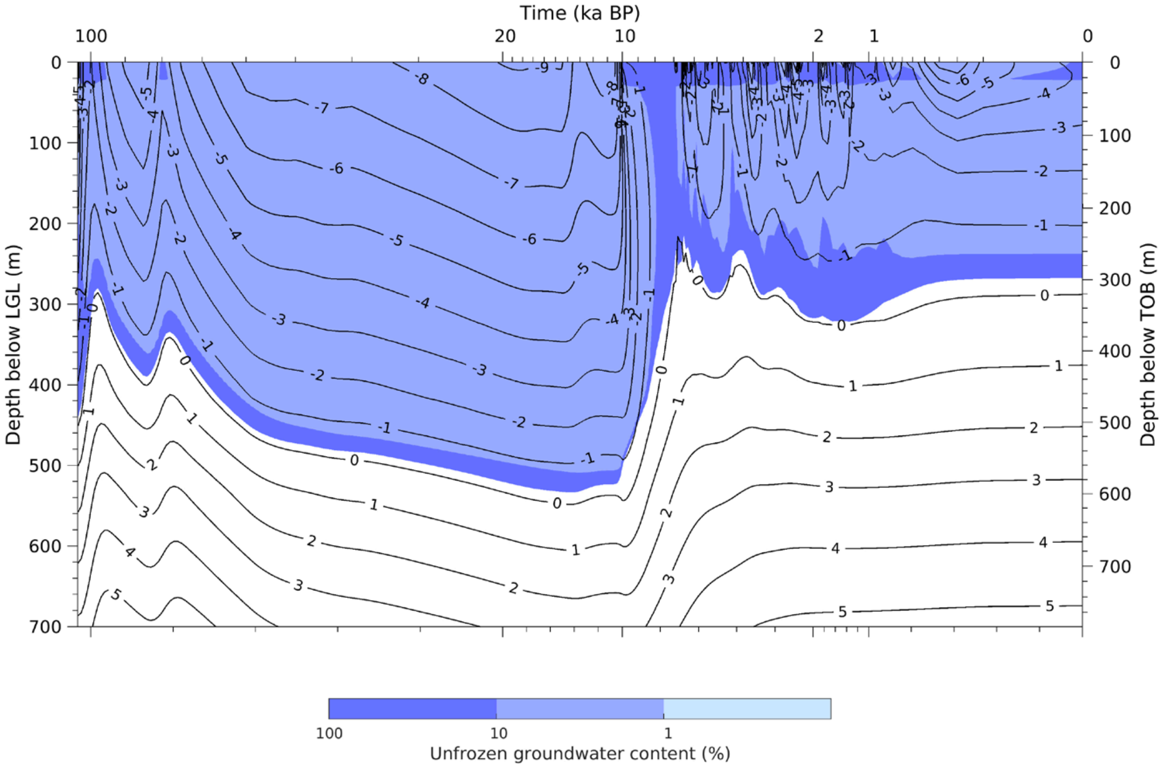

***Figure 4-5.** Same as Figure 4-3, but for the test case K_H_Gbh_800_Mean_S100 and Model A.*

The thermal state of the ground including the distribution of MAGT, unfrozen groundwater content and geothermal heat flow density and direction at the onset (10.5 ka BP) and end (7.1 ka BP) of deglaciation are shown in Figures 4-6 to 4-9. The corresponding hydro-chemical states containing salinity concentration, excess groundwater pressure, i.e. the groundwater pressure in excess of the initial steady-state hydrostatic pressure, and groundwater flow velocity and normalised flow direction are shown in Figures 4-10 to 4-13.

The perennially frozen ground contains a permeable frozen fringe, typically a 20–30 m thick layer containing unfrozen groundwater of 10 to < 100 volume-%, where groundwater flow can still occur as shown in Figure 4-11 (dark blue). The rest of the perennially frozen ground (with an unfrozen water content of more than 0 to 10 %) gets almost impermeable and the groundwater flow is significantly reduced (Figure 4-10). The increase in the unfrozen water content in two locations from 2.5 to 4 km to the left and from 5 to 7.5 km to the right from the borehole is related to the increase in the groundwater salinity concentration (Figure 4-10). At the end of the deglaciation, the perennially frozen ground obtains its minimum depth consisting mainly of the permeable frozen fringe (Figures 4-8, 4-9).

4.2.2 Middle and Late Holocene period (7–0 ka BP)

After the deglaciation, the ground surface is influenced directly by the prevailing climate, including the air temperature (Figure 3-4), and different precipitation and surface moisture conditions. Consequently, the ground surface cools gradually (Figure 4-2) with successive development of perennially frozen ground and permafrost (Figures 4-3 to 4-5) until the last readvance of the ice-sheet at 200–1 800 years BP. The transition from warm-based glacial conditions to colder ice-free conditions increases the geothermal heat flow considerably, from 12 to 25 mWm^{-2}, see Figure A4-1 in Appendix A4. Subsequently, the ground surface warms up to the present-day state. The maximum depth of perennially frozen ground and permafrost are obtained immediately after the last readvance, ranging between 270 and 430 m below LGL and 290 and 450 m below LGL, respectively. The measured permafrost depth based on the borehole temperature data is 340 m below LGL (380 m below TOB). The modelled permafrost dept for the K_H_Gbh 500_S100 test case with Model B exceeds the measured depth by 5 metres.

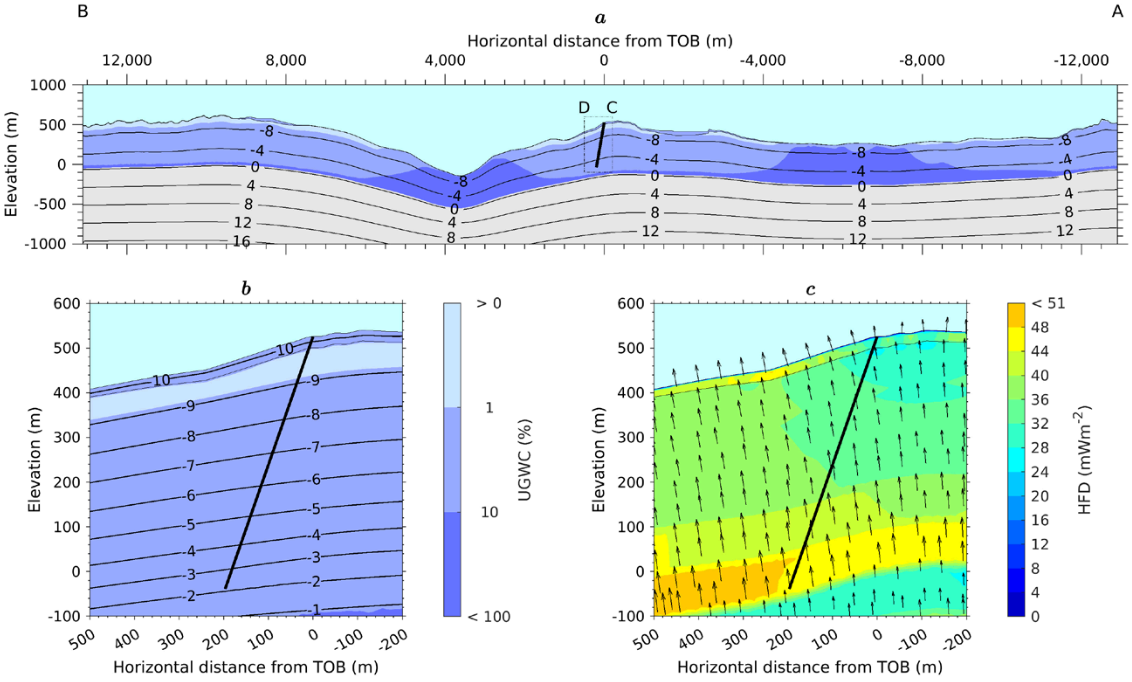

Figure 4-6. *MAGT and unfrozen groundwater content (UGWC) at the onset of deglaciation at 10.5 ka BP (a and b), and associated geothermal heat flow density (HFD) and flow direction (c) for the reference SICOPOLIS simulation (test case V_L_G_500_Mean_S100 and Model B). The ice-sheet is illustrated in cyan and the DH-GAP04 borehole by the black line. Note that the top plot uses a 2x vertical exaggeration.*

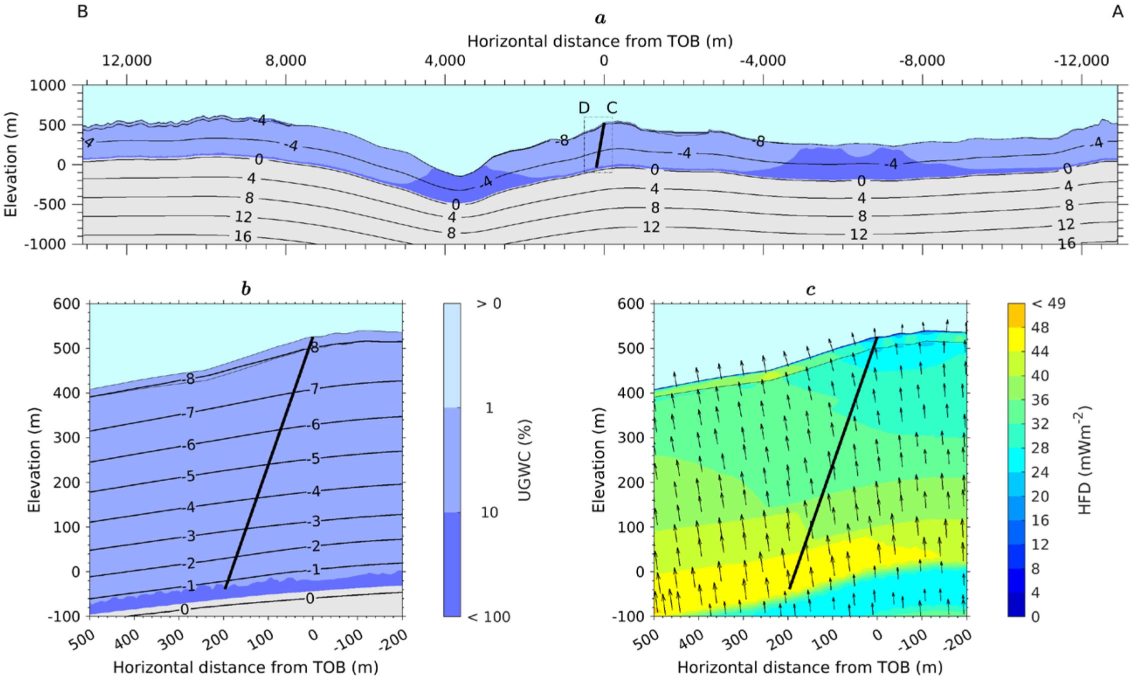

Figure 4-7. *Same as Figure 4-6, but for the sensitivity SICOPOLIS simulation (test case K_H_Gbh_500_Mean_S100 and Model B).*

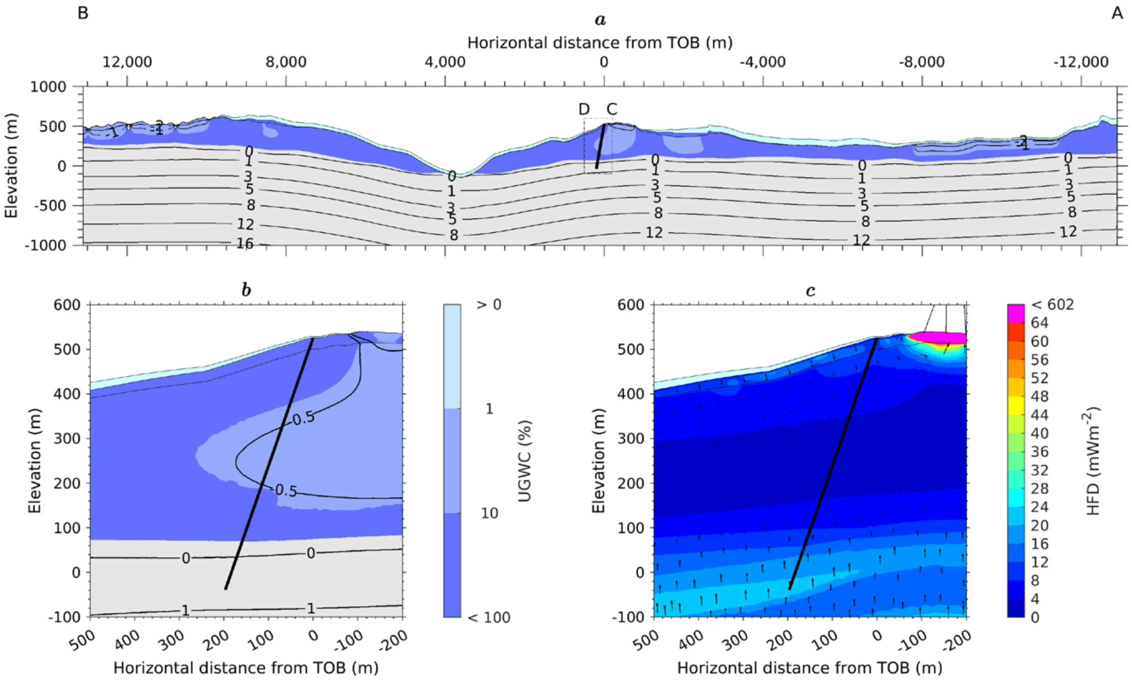

Figure 4-8. *Same as Figure 4-6, but for the end of deglaciation at 7.1 ka BP.*

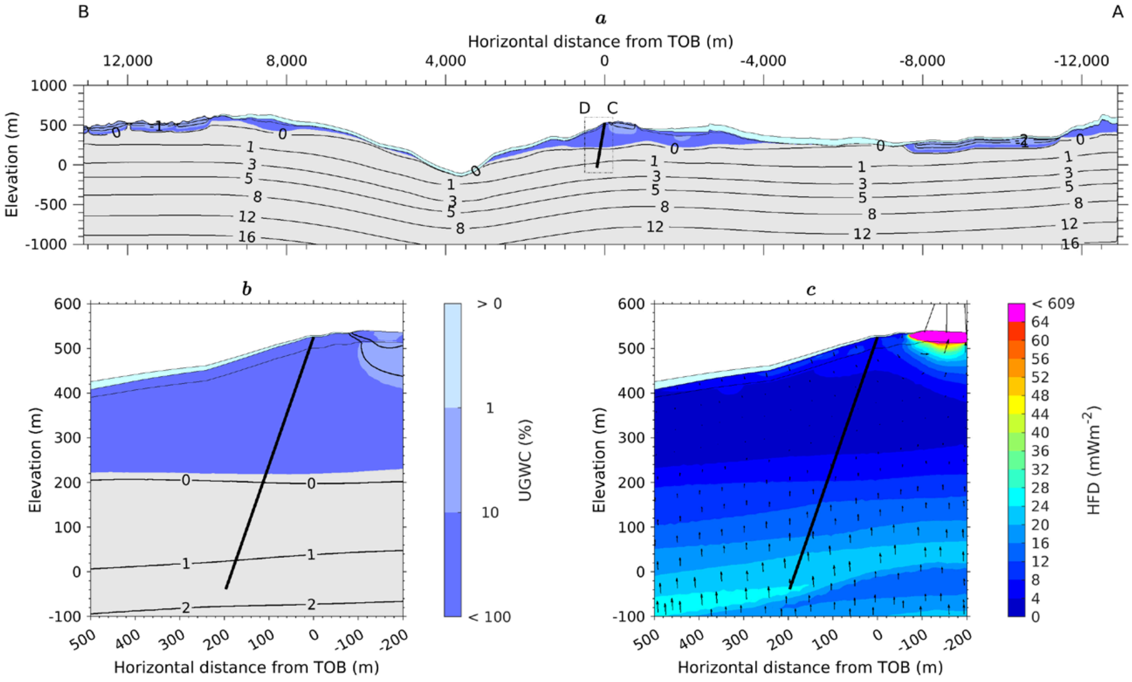

Figure 4-9. *Same as Figure 4-6, but for the sensitivity SICOPOLIS simulation and the end of the deglaciation at 7.1 ka BP.*

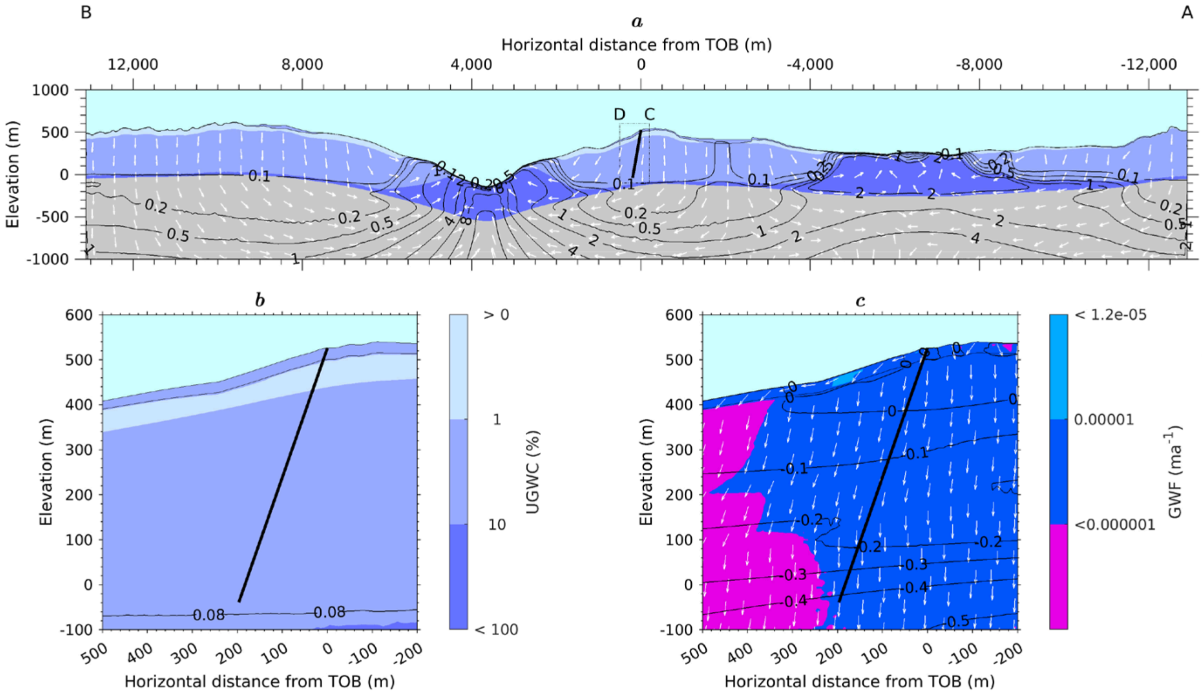

Figure 4-10. *Salinity concentration in mass-% and unfrozen groundwater content (UGWC) at the onset of deglaciation at 10.5 ka BP (a and b), excess groundwater pressure in MPa and groundwater flow (GWF) velocity and normalised flow direction (c) for the reference SICOPOLIS simulation (test case V_L_G_500_Mean_S100 and Model B). The ice-sheet is illustrated in cyan and the DH-GAP04 borehole by the black line. Note that the top plot uses a 2x vertical exaggeration.*

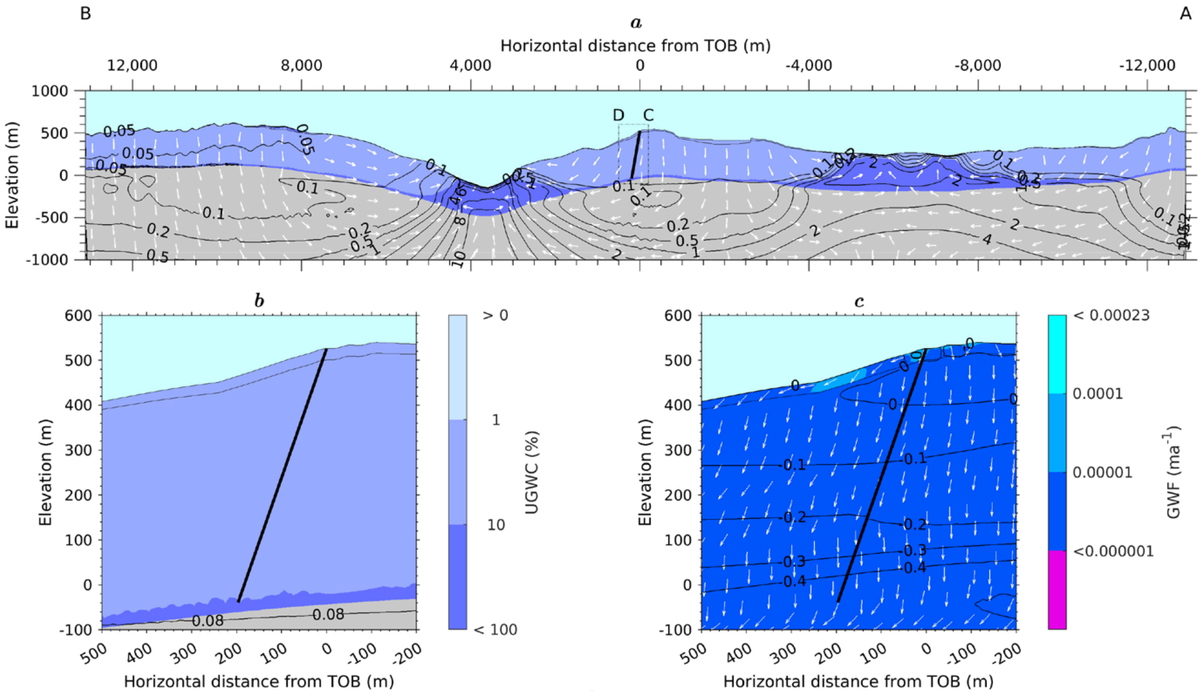

Figure 4-11. *Same as Figure 4-10, but for the sensitivity SICOPOLIS simulation (test case K_H_Gbh_500_Mean_S100 and Model B).*

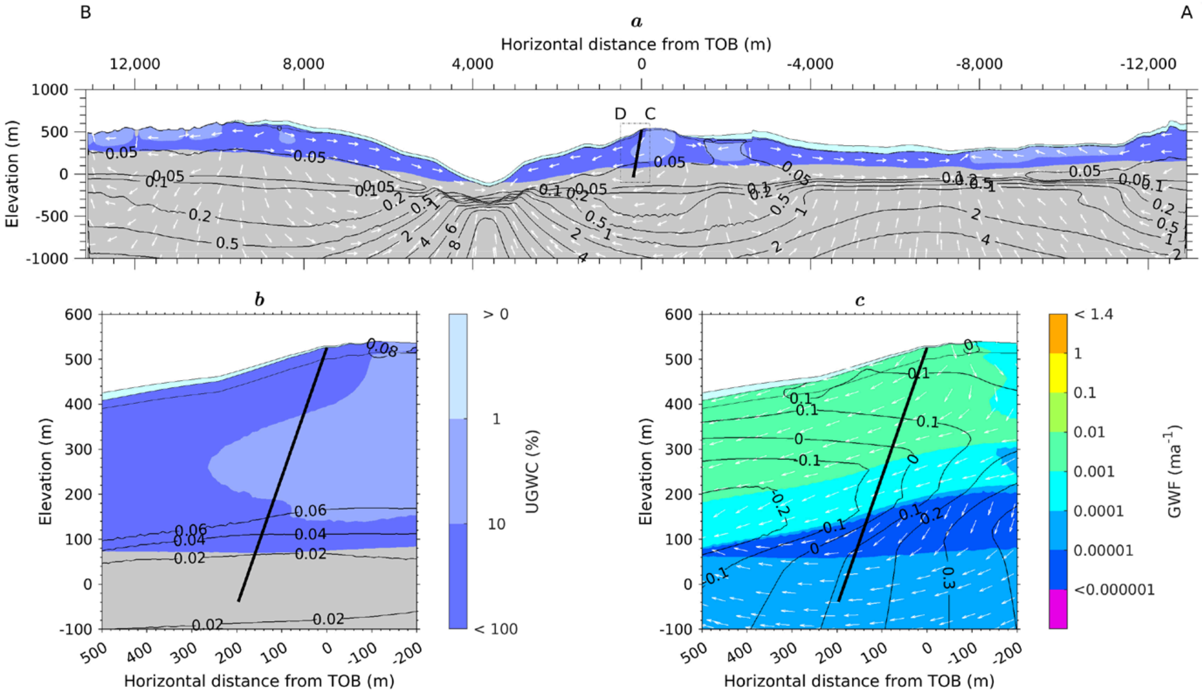

Figure 4-12. Same as Figure 4-10, but for the end of the deglaciation at 7.1 ka BP.

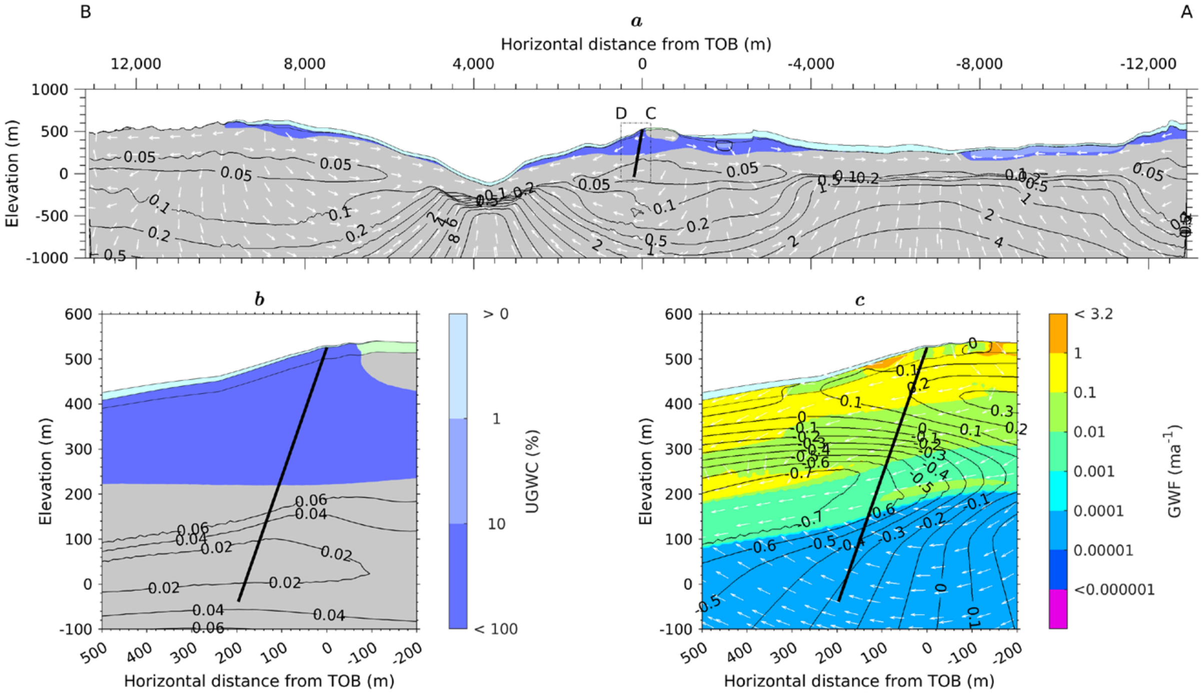

Figure 4-13. Same as Figure 4-10, but for the sensitivity SICOPOLIS simulation and the end of the deglaciation at 7.1 ka BP.

The present-day thermal state is shown for three test cases: V_L_G_500_Mean_S100 with Model B which results in the coldest bedrock (Figure 4-14), K_H_Gbh 500_S100 with Model B which yields the best agreement with the measured borehole temperature (Figure 4-15), and K_H_Gbh 800 with Model A which is the warmest simulation of the 16 core test cases (Figure 4-16). One third of the high downward geothermal heat flow values up to 300 mWm^{-2} is estimated to be due to a model artefact of the surface boundary condition type, as the ground surface temperature is forced to increase by ~3.5 °C during the last century. The corresponding hydro-chemical states including salinity concentration, excess groundwater pressure, i.e. the groundwater pressure in excess of the initial steady-state hydrostatic pressure, and groundwater flow velocity and normalised flow direction are shown in Figures 4-17 to 4-19. In addition, MAGT profiles and the range of fluctuation along the borehole and the extension for the same test cases are presented in Figures 4-20 to 4-22.

The modelled present-day MAGT along the borehole for all test cases with Model A and Model B are presented Figure 4-23 and Figure 4-24, respectively. The measured temperature in the figures is the annual mean temperature for the year September 2016 to August 2017 (Appendix A3.2.7). In addition, the mean and standard deviation of the borehole temperature difference between the model and observation (Figure 4-23 and Figure 4-24) are calculated for the 91–491 metres depth interval below LGL (100–550 m below TOB). The results are illustrated in Figure 4-25 (Model A) and in Figure 4-26 (Model B). In general, the test cases V_H_Gbh_800_Mean_S100 and K_H_Gbh_500_Mean_S100 give the best agreement with the measured bedrock temperature for Model A and Model B, respectively, whereas the test cases V_L_G_200_Mean_S100 and K_H_Gbt_1800_Mean_S100 yield the largest deviation for both Models (Figures 4-23 and 4-24).

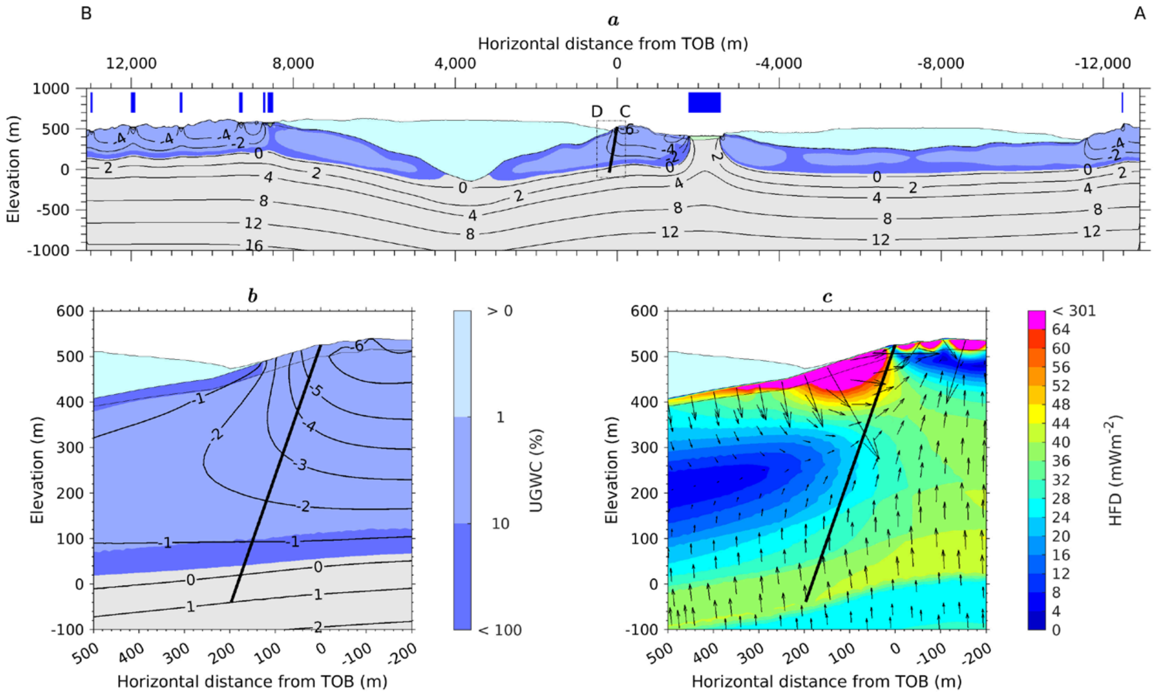

Figure 4-14. *Present-day MAGT contours and unfrozen groundwater content (UGWC) (a and b), and geothermal heat flow density (HFD) and flow direction (c) for test case V_L_G_500_Mean_S100 and Model B. The ice-sheet is illustrated in cyan, the location of the lakes by the blue bars and the borehole of DH-GAP04 by the black line. Note that the top plot uses a 2x vertical exaggeration.*

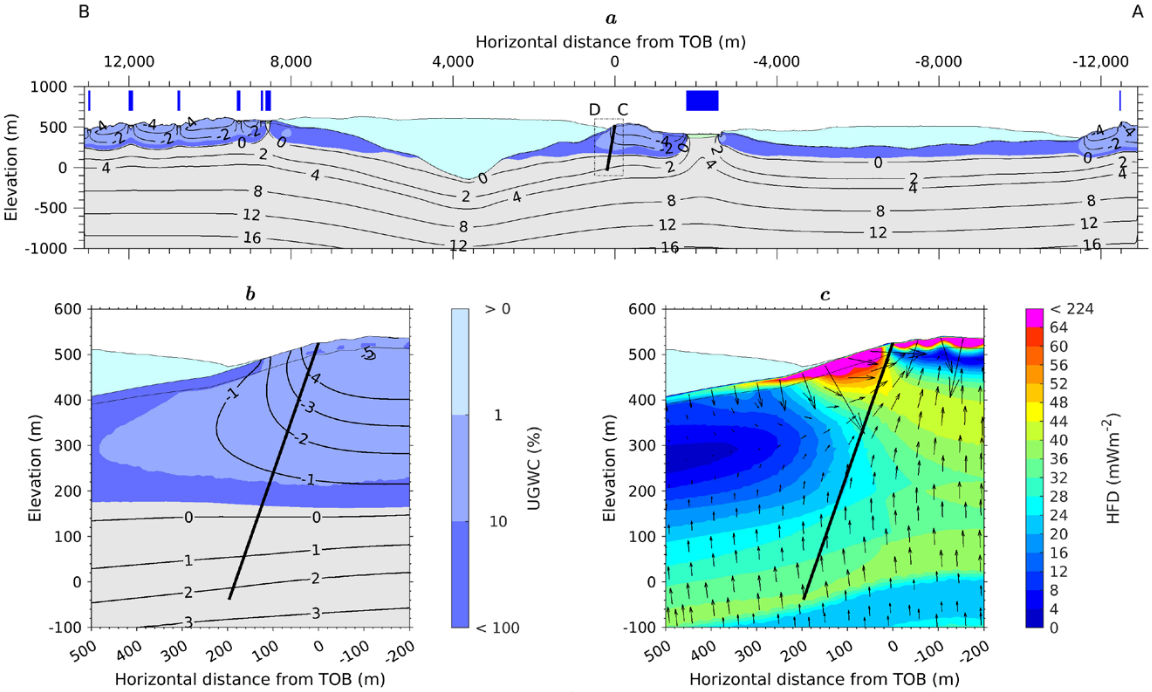

Figure 4-15. Same as Figure 4-14, but for the K_H_Gbh_500_Mean_S100 test case. The ice-sheet is illustrated in cyan, the location of the lakes by the blue bars and the borehole of DH-GAP04 by the black line.

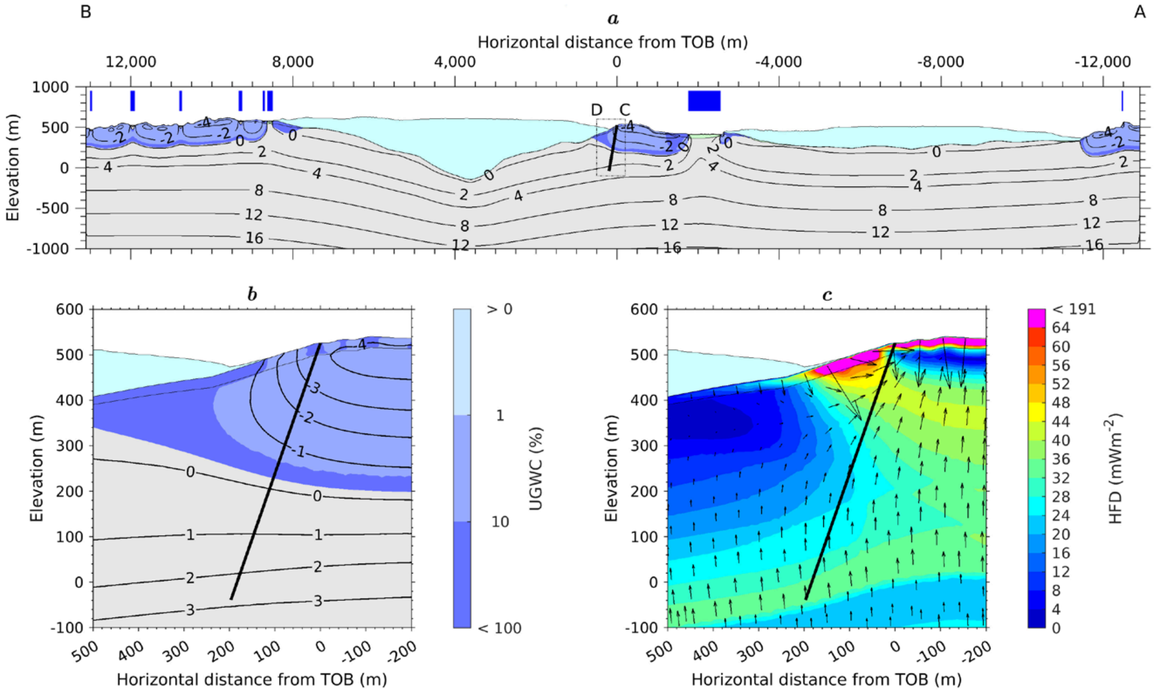

Figure 4-16. Same as Figure 4-14, but for the K_H_Gbh_800_Mean_S100 test case and Model A. The ice-sheet is illustrated in cyan, the location of the lakes by the blue bars and the borehole of DH-GAP04 by the black line.

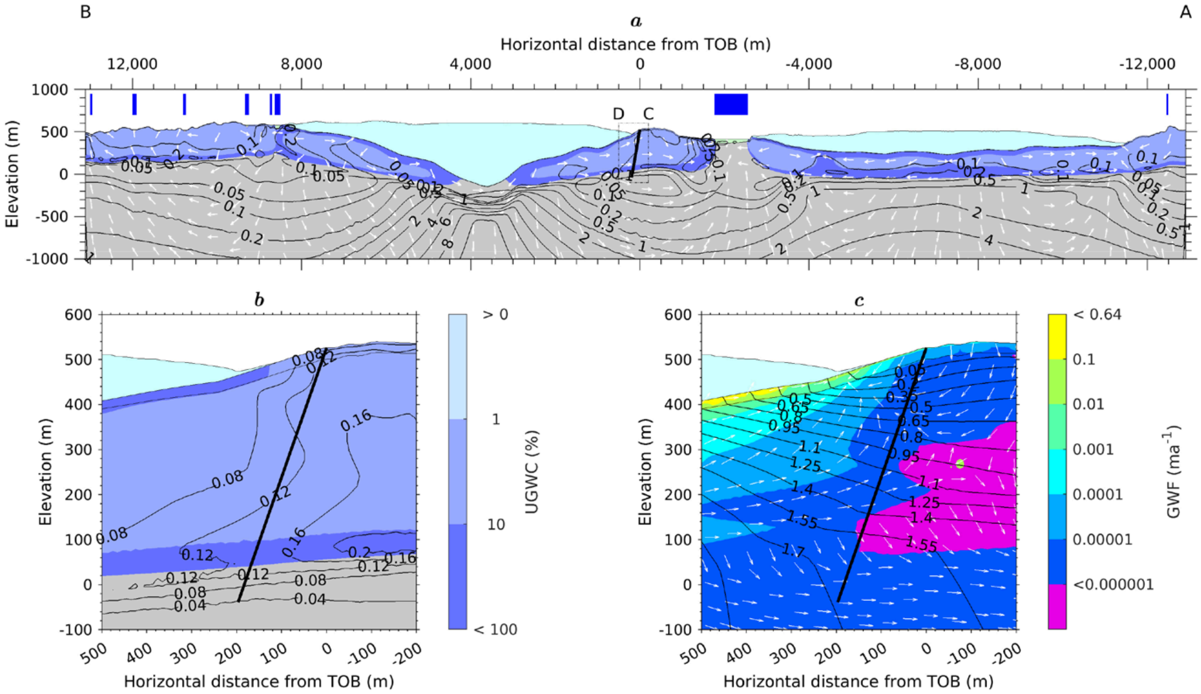

Figure 4-17. *Present-day salinity concentration in mass-% and unfrozen groundwater content (UGWC) (a and b), excess groundwater pressure in MPa and groundwater flow velocity and normalised flow direction (c) for test case V_L_G_500_Mean_S100 and Model B. The ice-sheet is illustrated in cyan, the location of the lakes by the blue bars and the borehole of DH-GAP04 by the black line. Note that the top plot uses a 2x vertical exaggeration.*

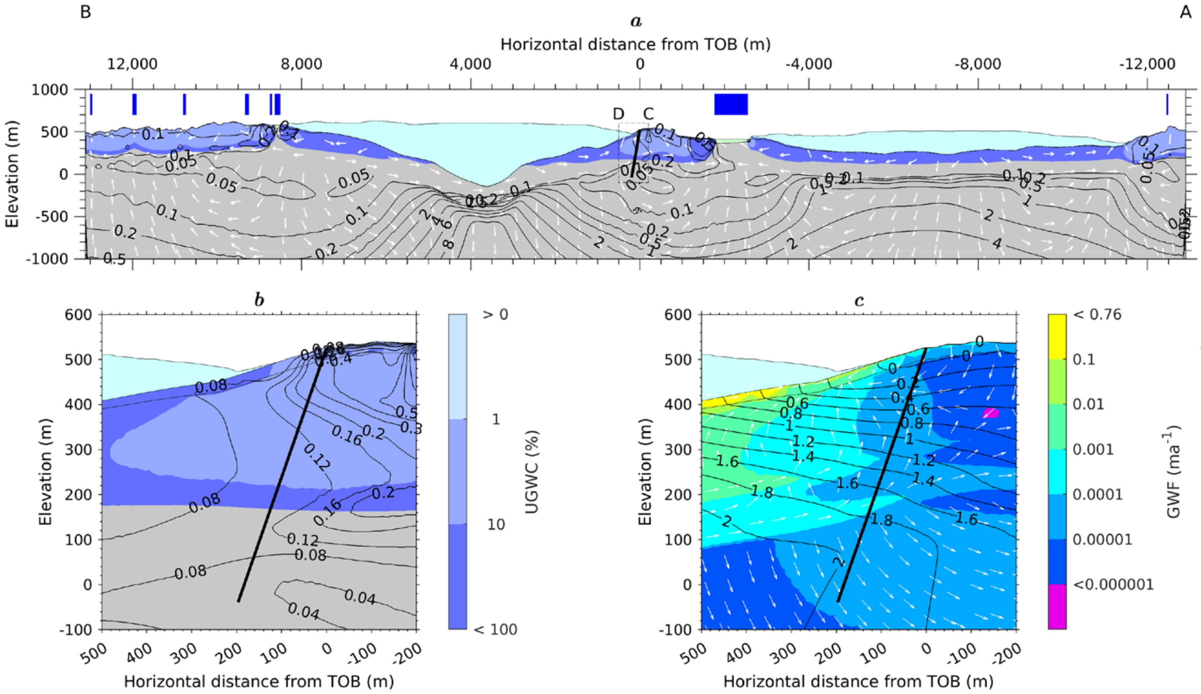

Figure 4-18. *Same as Figure 4-17, but for the K_H_Gbh_500_Mean_S100 test case. The ice-sheet is illustrated in cyan, the location of the lakes by the blue bars and the borehole of DH-GAP04 by the black line.*

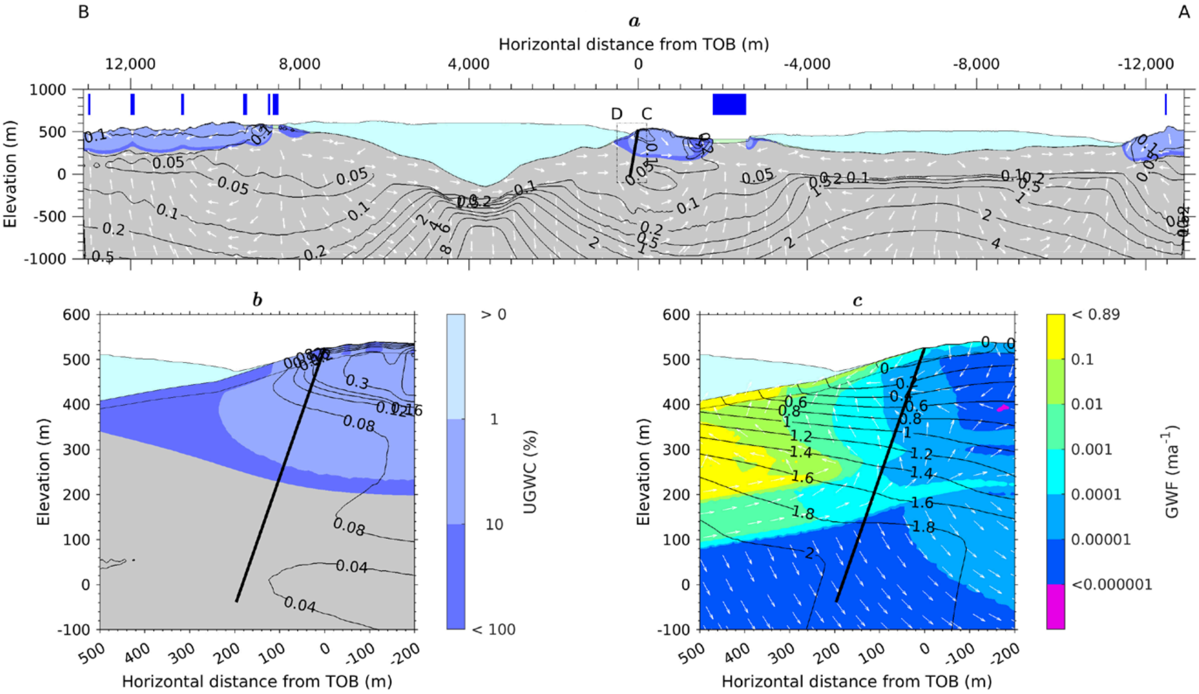

Figure 4-19. *Same as Figure 4-17, but for the K_H_Gbh_800_Mean_S100 test case and Model A. The ice-sheet is illustrated in cyan, the location of the lakes by the blue bars and the borehole of DH-GAP04 by the black line.*

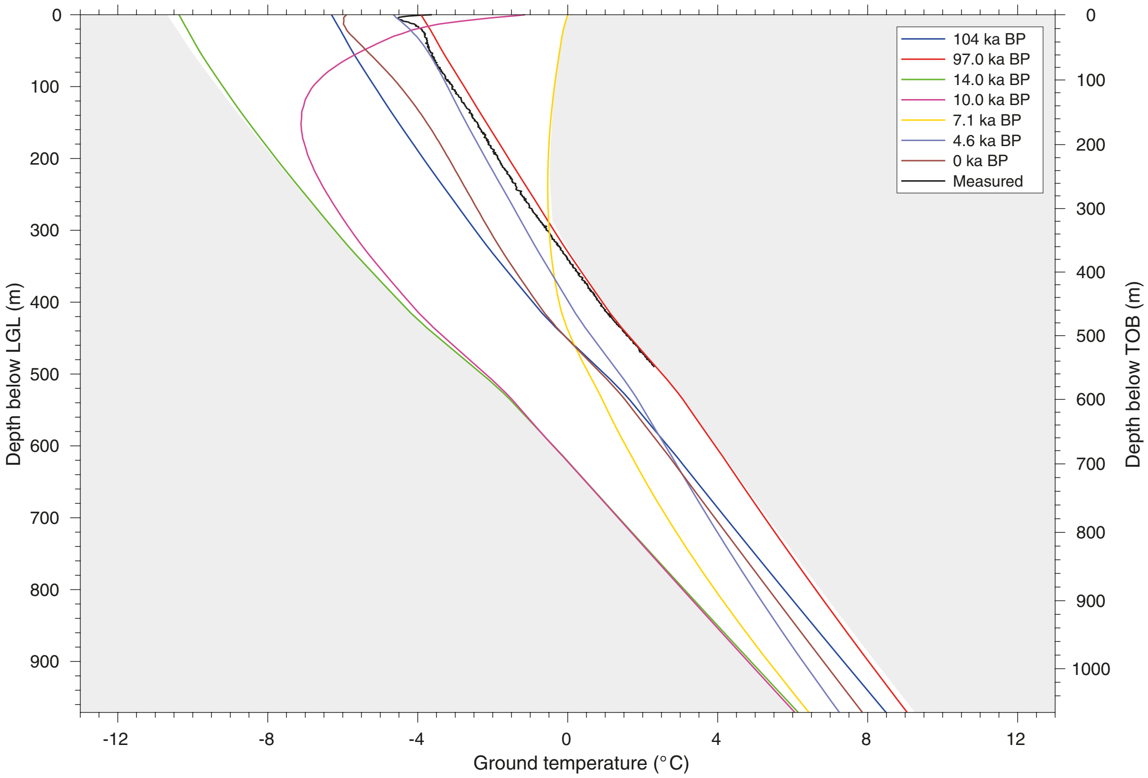

Figure 4-20. *MAGT along the borehole and the extension for the V_L_G_500_Mean_S100 test case and Model B. White envelope represents the range of temperature fluctuation over the glacial cycle (104–0 ka BP).*

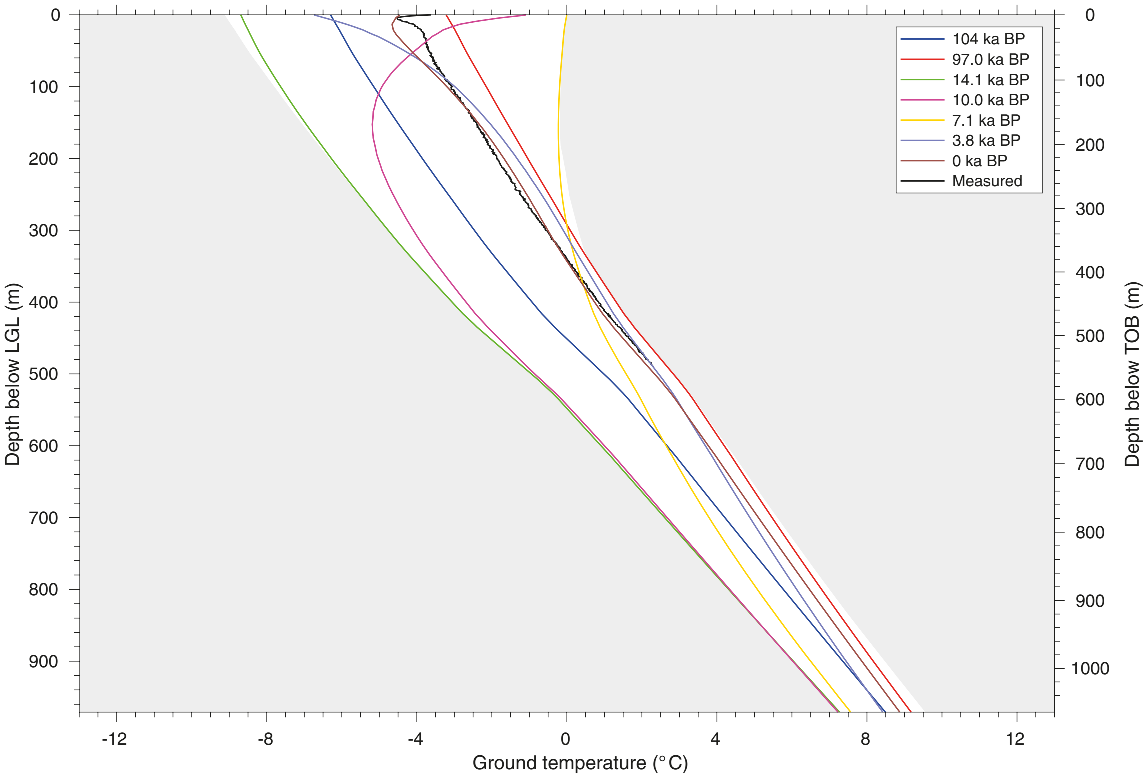

***Figure 4-21.** Same as Figure 4-20, but for the K_H_Gbh_500_Mean_S100 test case.*

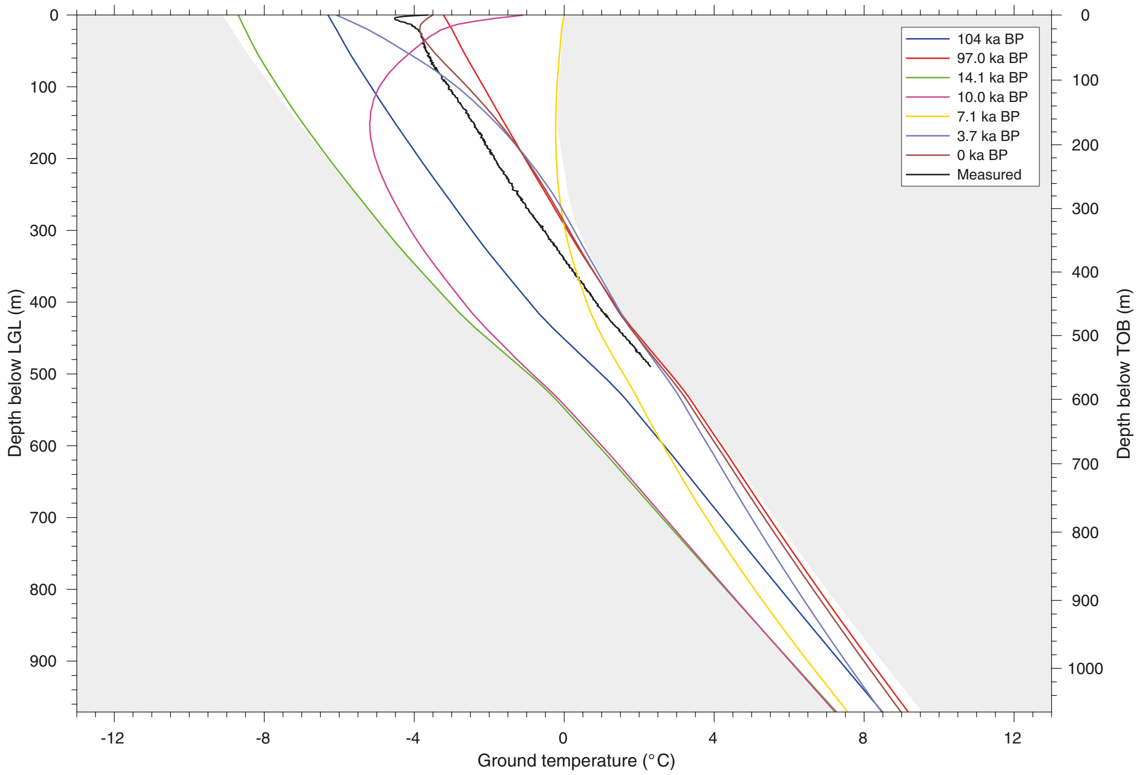

***Figure 4-22.** Same as Figure 4-20, but for the K_H_Gbh_800_Mean_S100 test case and Model A.*

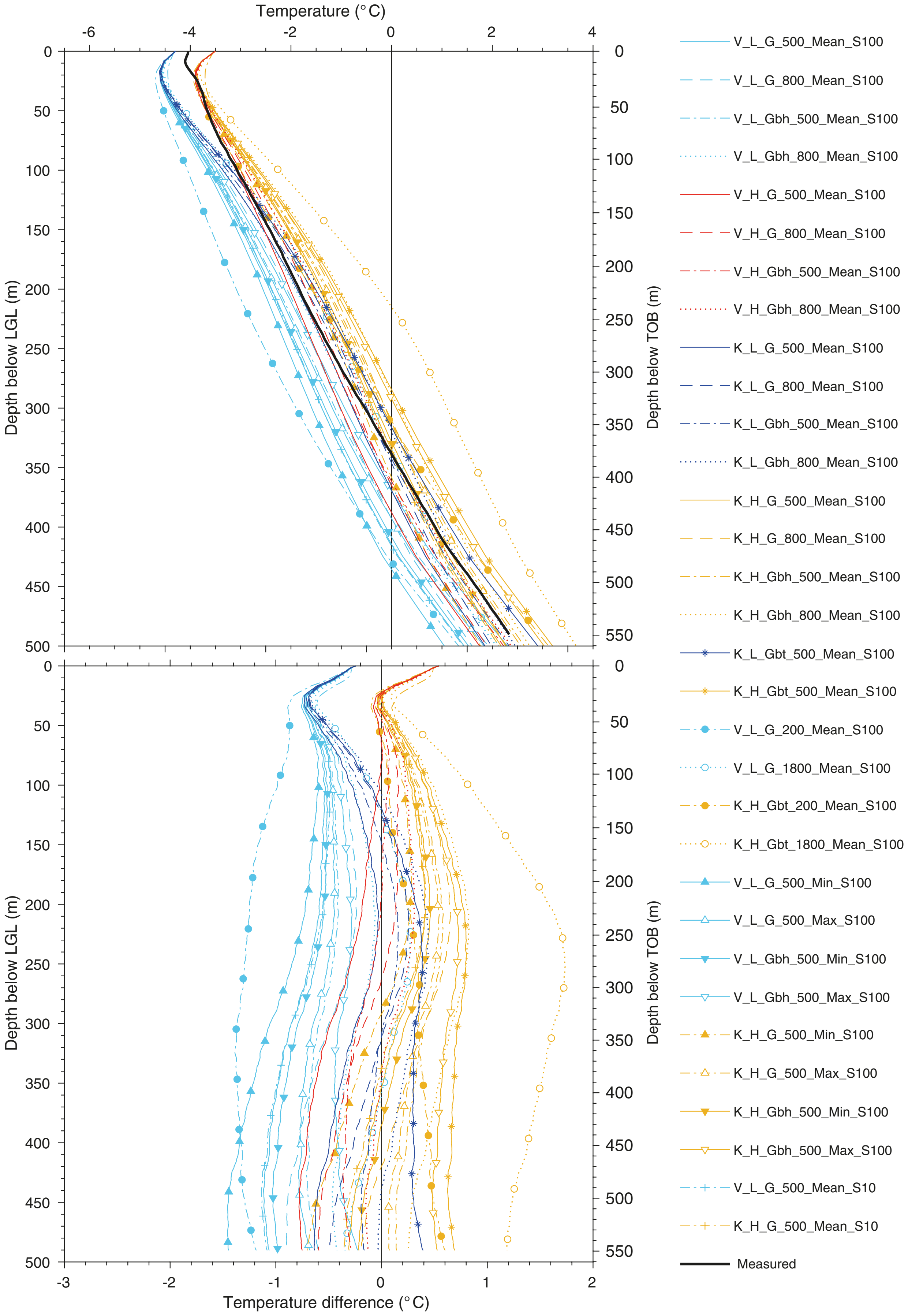

Figure 4-23. *Modelled present-day MAGT along the borehole of DH-GAP04 for the test cases described in Section 3.3.3 and Model A. The measured temperature (black line in upper panel) constitutes the annual mean for the year August 2016 to September 2017 (described in Appendix A3).*

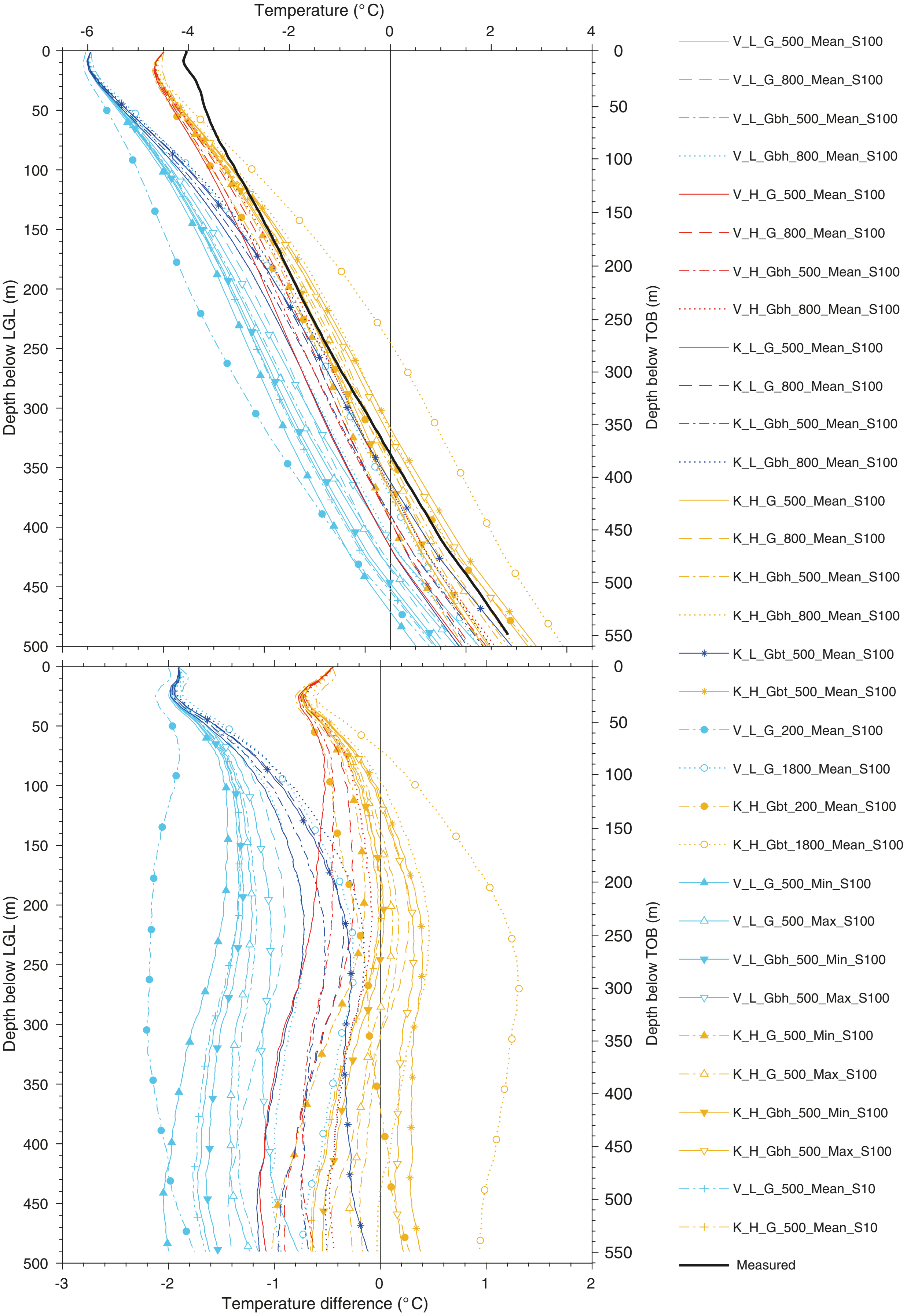

Figure 4-24. *Modelled present-day MAGT along the borehole of DH-GAP04 for the test cases described in Section 3.3.3 and Model B. The measured temperature (black line in upper panel) constitutes the annual mean for the year August 2016 to September 2017 (described in Appendix A3).*

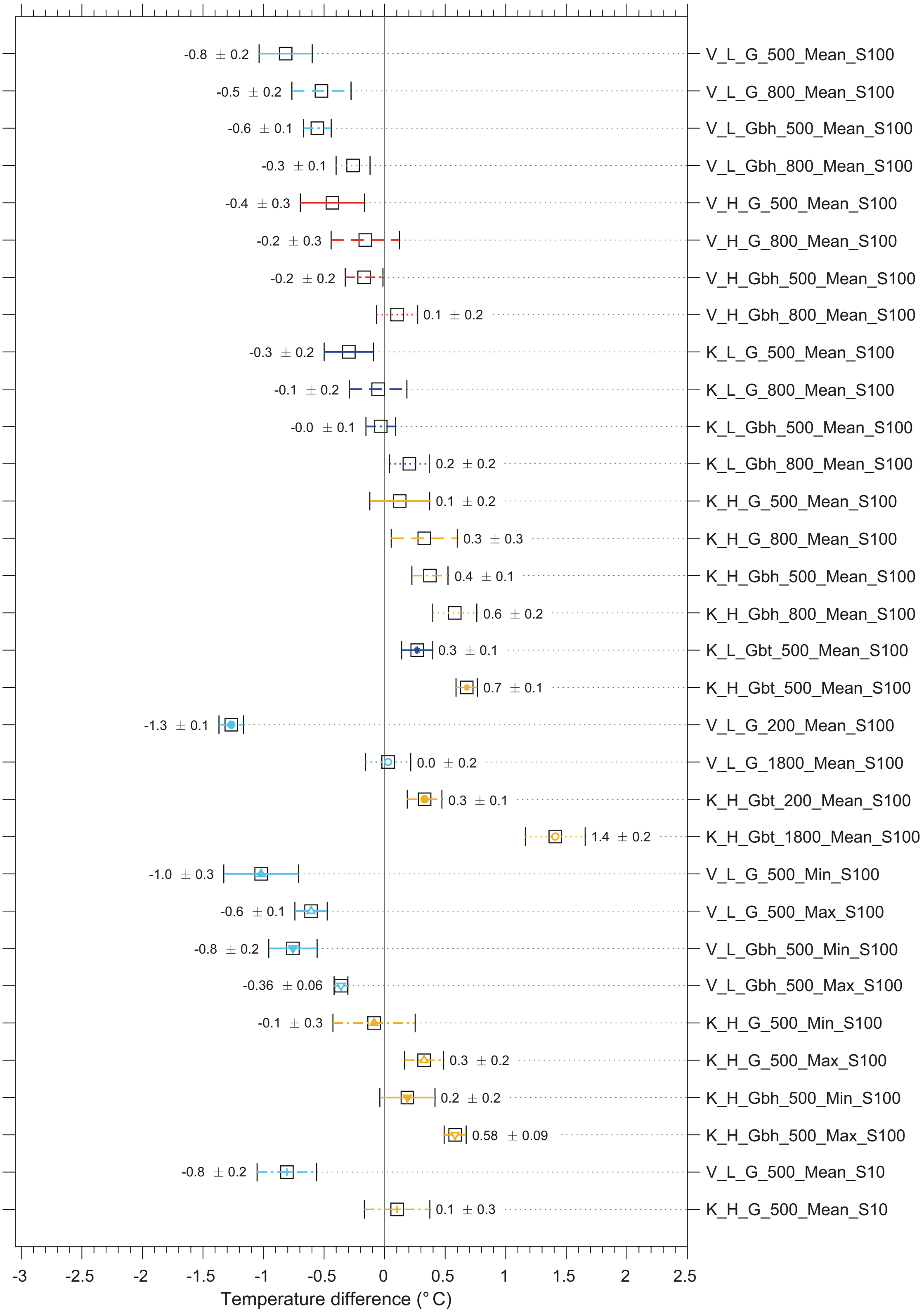

Figure 4-25. *Mean and standard deviation of the present-day borehole temperature difference shown in Figure 4-23 for the test cases described in Section 3.3.2 and Model A. The mean (square) and standard deviation (half of the line length) are calculated for the depth interval between 91 and 491 metres below LGL (100–550 m below TOB).*

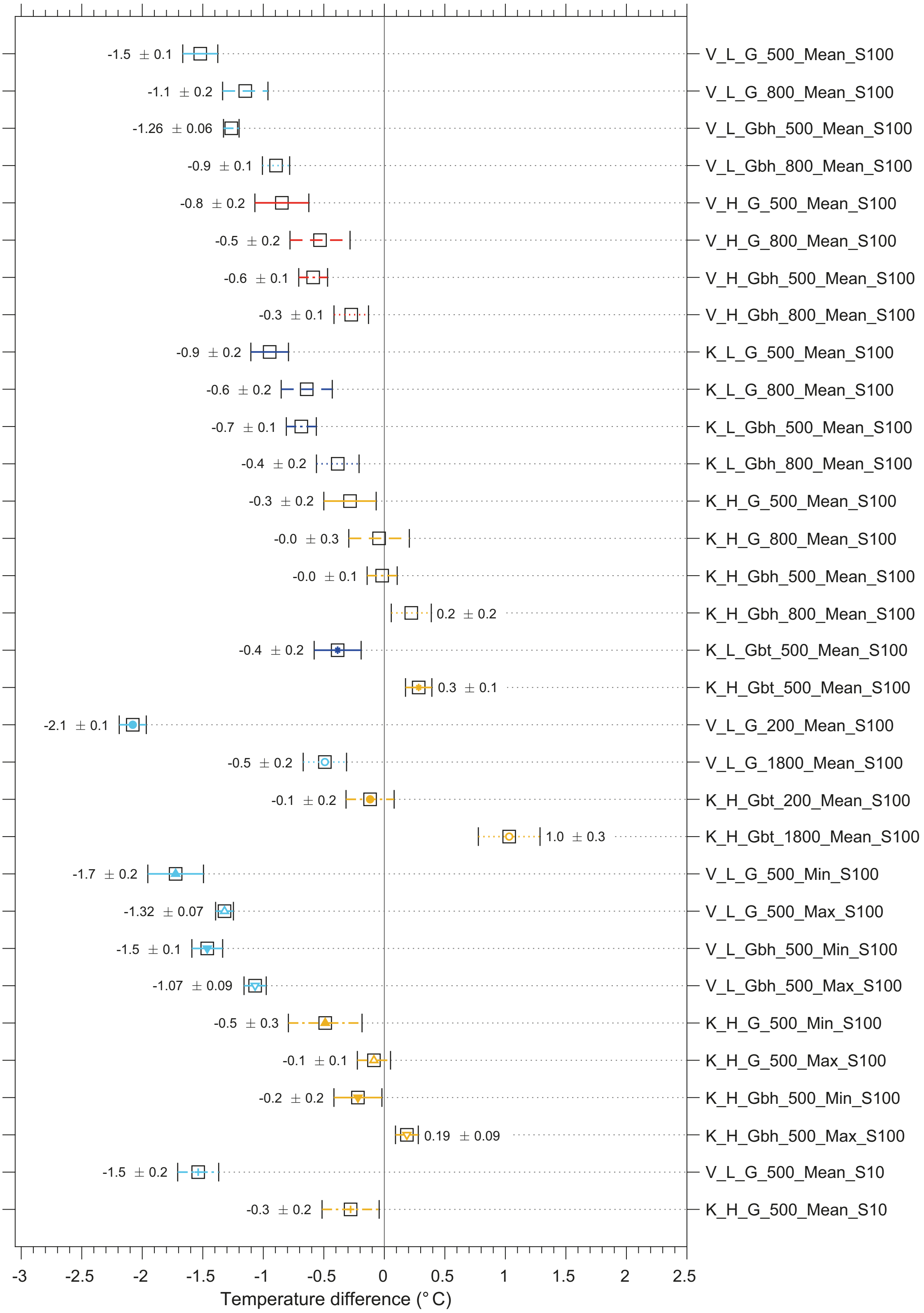

***Figure 4-26.** Mean and standard deviation of the present-day borehole temperature difference shown in Figure 4-24 for the test cases described in Section 3.3.2 and Model B. The mean (square) and standard deviation (half of the line length) are calculated for the depth interval between 91 and 491 metres below LGL (100–550 m below TOB).*

The effect of the variation in the key parameters on the bedrock temperature is illustrated in Figure 4-27. The higher Middle and Late Holocene air temperature (Kobashi v Vinther) results in 0.5 ± 0.1 °C higher average bedrock temperature for both models (Figure 4-27a), whereas the lower precipitation variant (low v high) yields 0.38 ± 0.06 °C (0.6 ± 0.1 °C) colder bedrock on average for Model A (Model B) (Figure 4-27b). The approximately 1.5 °C higher basal ice temperature (the sensitivity SICOPOLIS simulation v the reference SICOPOLIS simulation) leads to a 0.3 ± 0.1 °C increase in the average bedrock temperature (Figure 4-27c), whereas the 300 years earlier last readvance of the GrIS (800 vs. 500 years BP) results in the average temperature increase of 0.25 ± 0.06 °C (0.31 ± 0.08 °C) (Figure 4-27d). The thermal offset (the nonzero TO v zero TO) yields 0.64 ± 0.09 °C and 0.39 ± 0.05 °C average decreases in the bedrock temperature for the low and high precipitation variant, respectively (Figure 4-27e).

The sensitivity of present-day MAGT to the basal ice temperature, timing of the last readvance of the GrIS, geothermal heat flow and soil thickness for the bedrock temperature is further demonstrated in Figure 4-28. The 2.5 °C increase in the basal ice temperature (Figure 4-2) gives 0.6 ± 0.2 °C higher average bedrock temperature for both Models A and B. While the 300 years later last readvance of the GrIS at 200 years decreases the average present-day MAGT by 0.4 ± 0.2 °C (0.5 ± 0.2 °C), the 1 300 years earlier last readvance at 1 800 years BP yields a 0.8 ± 0.2 °C (0.9 ± 0.2 °C) increase in the average bedrock temperature for Model A (Model B). Regarding the geothermal heat flow, the 2 mWm^{-2} lower geothermal heat flow at the 10 km depth leads to 0.20 ± 0.09 °C lower average bedrock temperature, whereas the 2 mWm^{-2} higher geothermal heat flow results in the same amount higher average bedrock temperature for both Models A and B. Finally, the 90 % reduction of the soil thickness (test case S10) results in the 0.01 ± 0.03 °C decrease in the average bedrock temperature for both Models A and B (Figure 4-28).

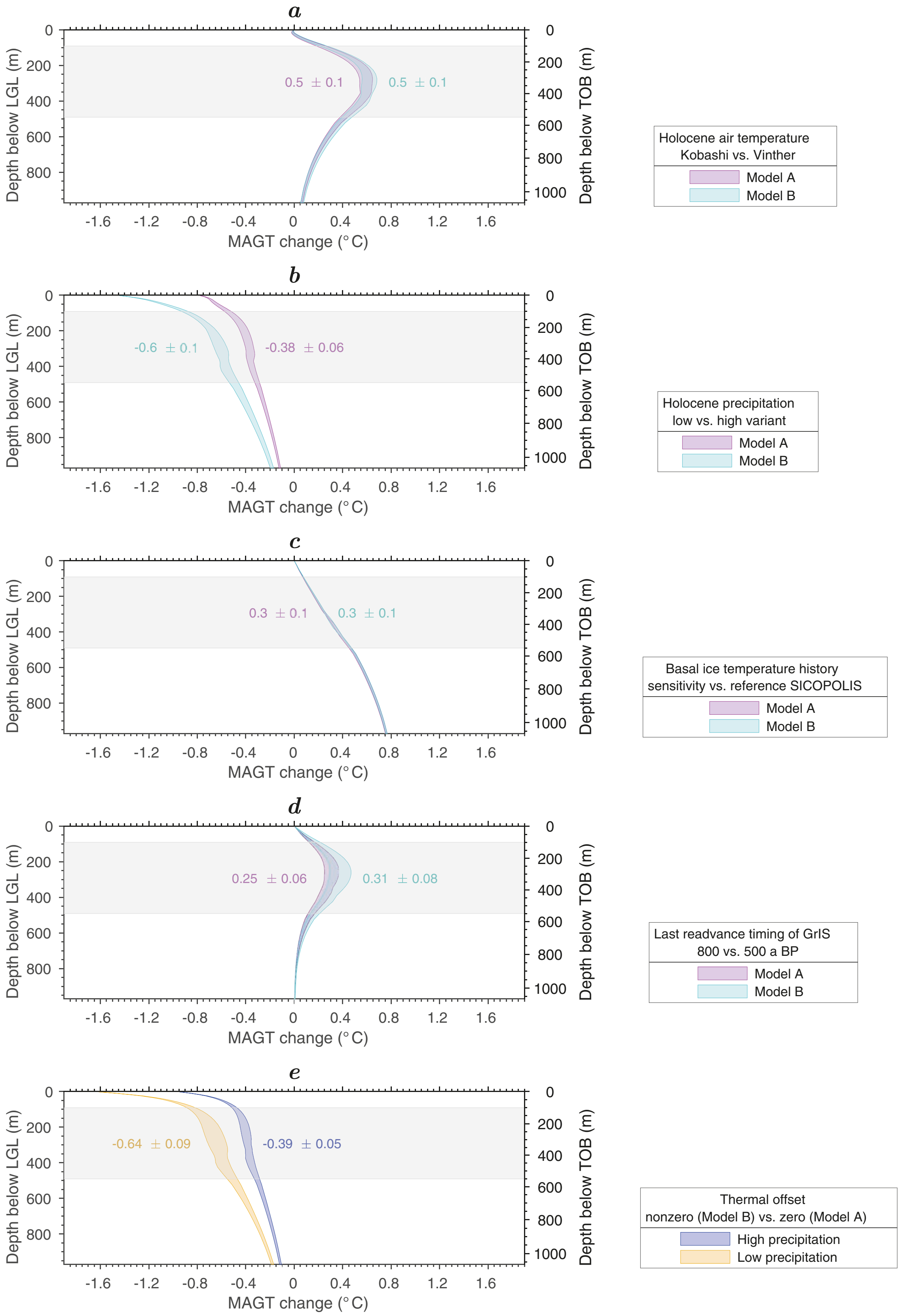

***Figure 4-27.** Present-day MAGT change along the borehole between the test cases of K (Kobashi) and V (Vinther) air temperature (a), L (low) and H (high) precipitation (b), Gbh (sensitivity SICOPOLIS) and G (reference SICOPOLIS) basal ice temperature history (c), 800 and 500 ka BP timing of the last readvance of the GrIS (d), and nonzero TO (Model B) and zero TO (Model A) (e). The 16 core test cases are included. Results in (a–d) are presented for Model A and Model B and in (e) for low and high precipitation variants. Coloured areas overlap with each other in a, c and d. The mean and standard deviation are calculated for the 91–491 metres depth interval below LGL (100–550 m below TOB) (grey area).*

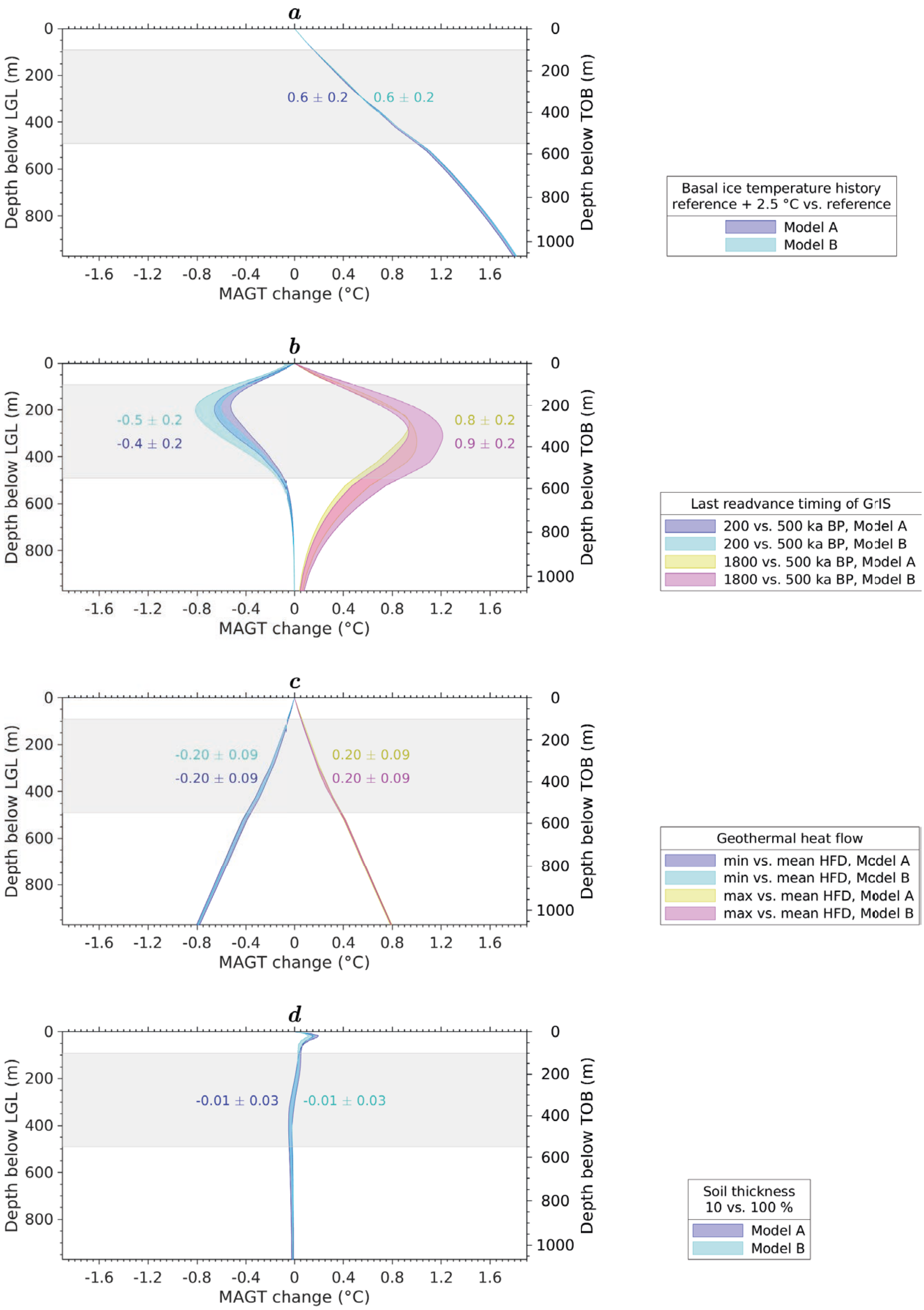

Figure 4-28. *Same as Figure 4-27 but for test cases between Gbt and G basal ice temperature (a), 200 and 500 years BP, 1 800 and 500 years BP timing of the last readvance of the GrIS (b), Min and Mean and Max versus Mean geothermal heat flow (c), and 10 and 100 % soil thickness (d). The grey area shows the 91–491 metres depth interval below LGL (100–550 m below TOB).*

5 Discussion

In the following, important factors for the thermal evolution of the ground and development of permafrost and perennially frozen ground (including air temperature, precipitation, surface moisture conditions, glacial conditions and geothermal heat flow) are discussed together with the results for the ground surface temperature, bedrock temperature, unfrozen groundwater content and groundwater flow and salinity.

5.1 Ground surface temperature

DH-GAP01 site

Calculations performed by the surface models for the STM site (Figure 2-3 and 3-1) show that under the optimised surface moisture conditions based on the present-day precipitation (the high precipitation variant) the surface models predict ~0.5 °C lower present-day MAGST compared to the measured value of −3.0 ± 0.5 °C, whereas the modelled TO is consistent with the measured value of −0.5 ± 0.5 °C (Table 4-1). In case the precipitation is reduced down to the level of the low precipitation variant, the modelled MAGST and TO are lowered further by ~0.9 °C and ~0.3 °C, respectively.

In the surface models, the surface moisture conditions are identified in terms of TWI. The results for the present-day surface moisture conditions (Figures 3-5, A2-6, A2-7) illustrate that dry surface conditions dominate the GAP site, with fresh-moist and wet conditions occurring in narrow zones and mainly in depressions. In relation to vegetation, the modelled dry surface condition is associated with short grassland in subarctic and tussocks in arctic climate (Hartikainen et al. 2010). This is in line with the observations at the DH-GAP01 site, where the vegetation is dominated by dwarf-shrub heath (Johannsson et al. 2015a). Depending only on the topography, TWI disregards the influence of water bodies such as the 'Talik lake' at the DH-GAP01 site, which likely contribute to the surface moisture conditions. Furthermore, considering that the present-day TWI values are used throughout the Middle and Late Holocene, changes in the topography due to erosion and sedimentation processes (and their influence on the TWI, surface moisture conditions and surface temperature) remain undetermined. The ice-sheet effect on the surface moisture conditions at the ice margin, however, is accounted for by the TWI (Figures 3-5, A2-6, A2-7).

DH-GAP04 site

At the DH-GAP04 site (Figures 2-3, 2-5, and 3-1), TWI yields fresh-moist and wet surface conditions for the barren ground surface above the borehole in front of the ice-sheet. As a result, the modelled ground surface temperature gets up to 3 °C higher than the air temperature (Table 4-2, Figure 4-1). When comparing with observations, modelled winter surface conditions agree well with the actual conditions, as visual monitoring on the site has detected accumulation of snow in the depression between the ice-sheet and the slope along the borehole (Figure 2-5 right). On the other hand, the absence of vegetation enables the insolation to warm the barren ground surface freely in summer, despite an increased air humidity due to the evaporation of melting ice-sheet. Consequently, the summer surface temperature can increase above the air temperature contradicting the model outcome of temperature reduction. However, without further information it is not possible to evaluate if the modelled MAGST in the fresh-moist and wet zones (Figure 3-5) is underestimated after the last readvance of the GrIS during the Late Holocene (0–1 800 years BP).

From the Middle to Late Holocene (from 7.1 ka BP up until between 0.3–1.8 ka BP), without the presence of the ice-sheet, dry surface moisture conditions prevail at the DH-GAP04 site. The small fresh moist area located above the middle section of the borehole (Figure 3-5) influences MAGST and TO only marginally (Figure 4-2). Regarding MAGST on the ice-covered areas during the Late Holocene, the main uncertainties concern the timing of the last readvance of the GrIS and the position of the ice margin. Plausibly, the basal ice temperature is at the pressure melting point during the readvance, which can be reliably defined in terms of the ice thickness. The +4 °C lake bottom temperature assumption is conservative since it results in a fast and extensive warming up of the ground (Figures 4-14 to 4-19).

However, the influence of lakes on the bedrock temperature at the DH-GAP04 site is marginal, since the nearest lake is located more than 1.5 km away from the borehole (Figure 3-2) (SKB 2006), corresponding to four times the permafrost thickness.

5.2 Bedrock temperature

The uncertainty in the modelled bedrock temperatures is estimated in terms of the mean and standard deviation between the modelled and measured temperatures for the depth interval between 91 and 491 metres below LGL (100–550 m below TOB). It is worthy of a remark that this depth interval has limitations on detecting effects on the bedrock temperature. Ground surface temperature signals dating from 3 000 to 200 years period before the present day have the maximum effect on the bedrock temperature, whereas effects of more distant signals have been gradually diminished in time yielding incomplete information on factors such as basal ice temperature history and geothermal heat flow.

The results also show that the different factors, including Middle and Late Holocene air temperature and precipitation, basal ice temperature history, geothermal heat flow, and ice-sheet readvance timing, interact weakly with each other. This indicates that the total effect can be obtained by superposition as a sum of the individual effects.

We remark that the 2D model overpredicts responses to the real 3D external forcing. For example, the warming of ground surface can be overestimated during last readvance of the GrIS as the ground surface turns to be warmer in front of the ice-sheet (Figure 3-5). In addition, the 2D model is unsuitable for modelling talik formation properly, since the important 3D groundwater flow network is not included. We also remark that the 2D model domain is aligned with the borehole to minimise unfavourable effects on comparisons with temperature measurements.

Best fit

Regarding Model A, the best fit with the measured bedrock temperature is obtained with the K_L_Gbh_Mean_500_S100 test case. It considers the Holocene MAAT based on the proxy ice-core records of argon and nitrogen isotopes by Kobashi et al. (2017) (K), low precipitation case (L), glacial conditions based on spatially modified geothermal heat flow (Gbh), timing of last readvance of the GrIS at 500 years BP and full soil thickness (S100) (Section 3.3.3). The high precipitation variant (H) of the same test case, i.e. K_H_Gbh_Mean_500_S100, yields the best match for Model B (Figure 4-25). These modelled temperature results are almost identical to the measured temperatures, differing by only 0.0 ± 0.1 °C from the measured temperature (Figures 4-24 and 4-25). The similarity of the results is explained by the outcome that the low precipitation case (L) with very light rain and snowfall and with zero TO (Model A) and the high precipitation case (H) based on the present-day precipitation with nonzero TO (Model B) have an approximately equivalent influence on the bedrock temperature (−0.4 ± 0.1 °C) (Figure 4-26). This is also valid for all corresponding test cases. Considering that Model A omits the verified TO and that there is no evidence in support of lower Middle and Late Holocene precipitation than the 40 mm annual precipitation level of the L precipitation case, the K_H_Gbh_Mean_500_S100 test case for Model B gives the better result of the two cases.

Effects of basal ice temperature and geothermal heat flow

The basal ice temperature history until the deglaciation during the 10.4–10.5 ka BP period (Figure 4-2) and the geothermal heat flow at the 10 km depth determines the base level for the bedrock temperature and its gradient. From this level, the bedrock warms up by ~4–6 °C during the deglaciation phase and the following ice free period (Figures 4-20 to 4-22). Both factors have a similar influence with an increasing trend in depth on the bedrock temperature (Figures 4-27 and 4-28). For example, the combination of the G basal ice temperature history and the maximum geothermal heat flow in the K_H_G_Max_500_S100 test case for Model B yields a compatible result (−0.1 ± 0.1 °C) with the K_H_Gbh_Mean_500_S100 test case (Figure 4-25). The temperature signal of the anomalous fast heating in the beginning of the deglaciation (Figures 4-20 to 4-22) has evened out from the borehole temperature profile.

Uncertainties in the parameters used in the SICOPOLIS simulations including spatial distribution of the geothermal heat flow and the last glacial cycle air temperature are accounted for by the basal ice temperature. When comparing the simulations with the G basal ice temperature history, the ~10 mWm^{-2} increase in the geothermal heat flow surrounding the DH-GAP04 site in the simulations with the Gbh basal ice temperature history, yields a ~0.4 °C increase in the bedrock temperature. To evaluate the effect of the uncertainty on the bedrock temperature further information on the spatial and temporal variability of geothermal heat flow is required. The permafrost simulation with a basal ice temperature history shows a spatial variability of the geothermal heat flow over the 2D model domain amounting to ~20 mWm^{-2} for the depth interval between 91 and 491 metres below LGL (Appendix A4). In addition, the geothermal heat flow seems to vary in time increasing to a ~10 mWm^{-2} higher value than that used in the SICOPOLIS simulations during the glacial phase (10.5–104 ka BP). Because of the coarse resolution (10 km) of the computational grid and time-independent geothermal heat flow, SICOPOLIS simulations are unable to handle the effects of plausible spatial and temporal variations in geothermal heat flow on the basal ice temperature. The 2.5 °C uncertainty in the last glacial cycle air temperature in the simulations with the Gbt basal ice temperature history results in a 0.8 °C increase in bedrock temperature as compared to the simulations with the G basal ice temperature history. The effect is deemed to be the largest since the full uncertainty is directly transmitted to the basal ice temperature.

The ~4 mWm^{-2} uncertainty associated with the palaeoclimatic correction in the geothermal heat flow has an effect on the bedrock temperature amounting to a 0.6 °C difference between the simulations with the minimum and maximum geothermal heat flow. Considering that the palaeoclimatic correction covers all the relevant factors including the Middle and Late Holocene air temperature (V, K) and precipitation (L, H), basal ice temperature history (G, Gbh) and timing of the last readvance of the GrIS (550, 800), the effect of the uncertainty on the bedrock temperature is reliable.

Effects of surface conditions

During the Middle and Late Holocene, the ground surface temperature and thermal offset driven by the air temperature and precipitation condition together with the last readvance of the ice-sheet govern the evolution of bedrock temperature. Regarding the borehole depth interval (91–491 m below LGL), the last 1 800 years seems to be of critical importance for the bedrock temperature. In addition, dissimilar factors such as the last readvance of the GrIS and the distinctly warmer period in the K air temperature profile between 200 and 1 700 years BP in comparison with that of the V air temperature (Figure 3-4) seem to have similar warming trend on the bedrock temperature (Figure 4-27). Regarding the uncertainty in the Middle and Late Holocene air temperature, the most part of the 0.6 °C effect on the bedrock temperature comes from the latest part of the Holocene (1 700–200 years BP). Effects of the air temperature discrepancies on the bedrock temperature before 3 ka BP are undetectable.

The uncertainty in the Middle and Late Holocene precipitation and TO representing the effect of seasonal freezing and thawing of soil have a similar effect on the bedrock temperature. The simulations between the low (L) and high (H) precipitation cases as well as between zero TO (Model A) and nonzero TO (Model B) result in a 0.3–0.7 °C temperature difference. Considering that the low and high precipitation cases (40 and 280 mm annual precipitation), determine the lower and upper limiting values for the precipitation during this period, the precipitation effect is plausible. Similarly, the TO effect is plausible, since while the zero TO referring to no seasonal freezing and thawing of soil defines the upper liming value for TO, the nonzero TO meaning freezing and melting of maximum amount of soil water results in the lower limiting value for TO. Freezing and melting of maximum amount of soil water is possible, because the ground is assumed to be completely saturated by groundwater in Model B. Among the parameters evaluated here, the uncertainty in timing of the last readvance of the GrIS between 1 800 and 200 years BP seems to have the largest effect on the bedrock temperature amounting generally to an 1–2 °C difference between the simulations with the earliest and latest readvances. The amount of the effect is valid since the timing of the last readvance of the GrIS based on geological findings is well defined (Section 3.3.3).

The large uncertainty in the soil thickness (Section 3.3.3) is shown to have a very small effect (−0.0 ± 0.1 °C) on the bedrock temperature for the depth interval between 91 and 491 metres below LGL independently of TO (Figure 4-28). On the other hand, the permafrost model omits the frost phenomenon that can create ground ice into ice lenses and ice wedges in the soil layer, which can change the soil thickness and the influence of soil on the ground temperature (French 2007, Williams and Smith 1989, Yershov 1998). Independently of the soil thickness the frost phenomenon increasing the soil water content can influence the bedrock temperature by increasing the amount of TO up to the theoretical maximum of pure water amounting approximately −4 °C (Equation 3-6). The degree of saturation of soil at the DH-GAP04 site is unknown as well as the existence of ground ice. However, visual perceptions of barren ground at the DH-GAP04 site in front of the ice-sheet support unsaturated soil water conditions, and thereby smaller TO than that of Model B. In addition, it is plausible that the Middle and Late Holocene has included periods during which the climate has been dry enough to drain and keep the topmost soil layer unsaturated.

5.3 Permafrost and perennially frozen ground

In the permafrost model, the development of permafrost and perennially frozen ground is governed by the basal ice temperature during the glaciated period (104–7 ka BP) and the ground surface temperature modelled by the surface model in terms of the air temperature and surface moisture conditions dependent *n*-factors, during the last 7 ka. Given the variation in these parameters, the thickness of the modelled perennially frozen ground at the DH-GAP04 site varies between 240 and 600 metres over the last 104 ka (Figures 4-3 to 4-5). The maximum thickness is obtained after LGM at 13.2 ka BP and the minimum thickness at the end of the deglaciation at 7.1 ka BP. The permafrost thickness (depth of 0 °C isotherm) is typically 20 metres greater than the thickness of the perennially frozen ground. The modelled present-day permafrost depth at the DH-GAP04 site based on the bedrock temperature results (Figures 4-23 and 4-24) varies considerably between the test cases amounting between 210 and 440 metres for Model A and between 250 and 480 metres for Model B. The perennially frozen ground depth remains 10 to 20 metres shallower. Among the parameters considered here a combination of the lowest basal ice temperature (G) and minimum geothermal heat flow (Min) together with the lowest Middle and Late Holocene air temperature (V) and lowest precipitation (L) yields the maximum depth, whereas the highest basal ice temperature (Gbt), the highest air temperature (K) and precipitation (H) and the earliest readvance of the GrIS at 1 800 years BP result in the minimum thickness by a clear 70 metres margin. In addition, the modelled present-day subglacial perennially frozen ground at the DH-GAP04 site extends 500 to 3 000 metres horizontally under the ice-sheet margin with an increasing amount of unfrozen groundwater (Figures 4-14 to 4-16). This compares well with the 2 km subglacial permafrost interpretation at this site by Ruskeeniemi et al. (2018). In areas where the unfrozen groundwater content gets larger than 10 %, the groundwater flow is enhanced in the partially frozen ground up to ~ 1 m/a, in particular below the ice-sheet (Figures 4-17 to 4-19). In contrast, for deeply frozen locations such as the DH-GAP04 drill site the ground becomes impermeable and the groundwater flow through the frozen ground is effectively prevented.

In addition to the temperature, the perennially frozen ground depends also on the groundwater pressure and salinity such that the freezing of groundwater decreases with increasing groundwater pressure and salinity concentration. The groundwater pressure increases with depth due to gravity such that the hydrostatic pressure at the 500 metres depth decreases the freezing point of water by 0.35 °C. During the deglaciation and the last readvance of the GrIS, the groundwater pressure is further increased due to the weight of an overlying warm-based ice-sheet (Figures 4-17 to 4-19). At the end of the deglaciation, at 7 ka BP, the groundwater refreezes rapidly (Figure 4-3), as the groundwater is depressurized with the retreating ice-sheet (Figure 4-12). The salinity concentration of groundwater increases with depth, as well. In addition, a strong concentration of salinity can be seen in depressions below the ice-sheet from 2.5 to 4 km to the left and from 5 to 7.5 km to the right from the borehole during the glacial period (104–7.1 ka BP) (Figures 4-10 and 4-11). As a result, the freezing of groundwater is reduced significantly despite low temperatures (Figures 4-6 and 4-7). Furthermore, the perennially frozen ground gets diluted (thawed zones in Figures 4-12 and 4-13), as the almost impermeable ground prevents the motion of salinity towards the ground surface on the one hand, and the excluded salt in the freezing process migrates down to the unfrozen zone on the other hand.

In the beginning of the ice-free period, open taliks, layers of year-round unfrozen ground through the permafrost, are formed below the lakes in the model domain shown in Figure 3-2. Only the largest lake located approximately 2 km to the right from the borehole is able to maintain an open talik, whereas the taliks under the other smaller lakes (in the left part of profile) partially or completely close over time (Figures 4-14 to 4-16).

6 Conclusions

The present study aimed to investigate how simulated ground surface temperatures, permafrost depths and bedrock temperatures from permafrost models used in safety assessments compare with observed data on soil temperature and bedrock temperature from the GAP site in west Greenland. Two versions of a numerical permafrost model (Model A without thermal offset and Model B with thermal offset) were evaluated.

We present an extensive set of permafrost model simulations for key parameters of the thermal evolution of ground and bedrock for a location by the Greenland ice sheet (GrIS) in the Kangerlussuaq region, south–western Greenland. The last glacial cycle period is simulated up to present-day with the overall purpose of evaluating the permafrost modelling code by comparing modelled bedrock temperatures with temperatures observed in a 649 m deep borehole at the present ice-sheet margin. The input parameters include air temperature and precipitation for the last 7 ka (approximately the Middle and Late Holocene), surface moisture conditions and thermal offset (seasonal freezing and thawing of soil) as well as initial conditions based on basal ice temperature histories for the last glacial period, deep-ground geothermal heat flow accounting for palaeoclimatic effects and timing of the most recent ice-sheet readvance. The following conclusions can be drawn from the study:

- Taking all identified uncertainties in input data into account, the comparison between observed and modelled bedrock temperatures show that the permafrost models predict the present-day bedrock temperature for the full 400 metres depth interval (91–491 m below the ground surface) within the range −1.4 and +1.6 °C for Model A and −2.2 and +1.3 °C for Model B.
- This uncertainty ranges relates both to input data uncertainty and intrinsic model errors. The fact that the uncertainty ranges in the simulated temperature are nearly centred around the measured temperature indicates that any potential intrinsic model error is small, as such error would systematically simulate either too warm or too cold conditions.
- These ranges will be used to assess the assumptions and conclusions associated with the permafrost simulations previously made for the safety assessments at the Forsmark site, Sweden (SKB 2010, 2014, 2020). Generally, one concern is if the model was to produce too high bedrock temperatures, since this would result in too shallow permafrost modelled for the Forsmark site. However, the model uncertainties obtained in the present study, typically up to around ±1.5 °C, are considered small in this context. Also worth noting is that within the obtained uncertainty range, the contribution by the (smaller) intrinsic model errors is of relevance for the previous Forsmark simulations, whereas the contribution by the larger input data errors at Greenland is not of relevance for the previous Forsmark simulations, since corresponding input data errors are already handled in the Forsmark simulations.
- The model results also provide useful information on uncertainties of the key parameters and their effect on the evolution of permafrost and perennially frozen ground and the bedrock temperature down to a 500 metres depth. While the air temperature, precipitation, surface moisture conditions, thermal offset and timing of ice-sheet readvance govern the uppermost subsurface temperature with the overall uncertainty effect of ~3.5 °C, the initial conditions and geothermal heat flow determine the baseline for the bedrock temperature with the combined uncertainty effect of ~1.5 °C.

References

SKB's (Svensk Kärnbränslehantering AB) publications can be found at www.skb.com/publications. SKBdoc documents will be submitted upon request to document@skb.se.

Aebly F A, Fritz S C, 2009. Palaeohydrology of Kangerlussuaq (Søndre Strømfjord), West Greenland during the last ~8 000 years. The Holocene, 19, 1, 91–104, doi:10.1177/0959683608096601

Anderson N J, Leng M L, 2004. Increased aridity during the early Holocene in West Greenland inferred from stable isotopes in laminated-lake sediments. Quaternary Science Reviews, 23, 841–849.

Applegate P J, Kirchner N, Stone E J, Keller K, Greve R, 2012. An assessment of key model parametric uncertainties in projections of Greenland Ice Sheet behavior. The Cryosphere 6, 589–606.

Artemieva I M, 2019. Lithosphere thermal thickness and geothermal heat flux in Greenland from a new thermal isostasy method. Earth-Science Reviews 188, 469–481.

Bartholomew I D, Nienow P, Sole A, Mair D, Cowton T, King M A, Palmer S, 2011. Seasonal variations in Greenland Ice Sheet motion: Inland extent and behaviour at higher elevations. Earth and Planetary Science Letters 307, 271–278.

Bennike O, Björck S, 2002. Chronology of the last recession of the Greenland Ice Sheet. Journal of Quaternary Science 17, 211–219.

Benfield A E, 1939. Terrestrial heat flow in Great Britain. Proceedings of the Royal Society 173, 428–450.

Beven K J, Kirkby M, 1979. A physically-based variable contributing area model of basin hydrology Hydrological Science Bulletins 24, 43–69.

Birch F, 1948. The effects of Pleistocene climatic variations upon geothermal gradients. American Journal of Science, 246, 729–760.

Bosson E, Selroos J-O, Stigsson M, Gustafsson L-G, Destouni G, 2013. Exchange and pathways of deep and shallow groundwater in different climate and permafrost conditions using the Forsmark site, Sweden, as an example catchment. Hydrogeology Journal 21, 225–237.

Brandefelt J, Näslund J-O, Zhang Q, Hartikainen J, 2013. The potential for cold climate conditions and permafrost in Forsmark in the next 60 000 years. SKB TR-13-04, Svensk Kärnbränslehantering AB.

Briner J P, McKay N P, Axford Y, Bennike O, Bradley R S, de Vernal A, Fisher D, Francus P, Fréchette B, Gajewski K, Jennings A, Kaufman D S, Miller G, Rouston C, Wagner B, 2016. Holocene climate change in Arctic Canada and Greenland, Quaternary Science Reviews, 147, 340–364.

Brown J B, Ferrians O J, Heginbottom J A, Melnikov E S, 1997. Circum-Arctic Map of Permafrost and Ground-Ice Conditions. U.S. Geol. Surv. Map CP-45, scale 1:10 000 000.

Calov R, Ganopolski A, Claussen M, Petoukhov V, Greve R, 2005. Transient simulation of the last glacial inception. Part I: glacial inception as a bifurcation in the climate system. Climate Dynamics 24, 545–561.

Cappelen J (ed), 2012. Weather and climate data from Greenland 1958–2011 – Observation data with description. DMI Technical Report 12-15, Danish Meteorological Institute.

Cappelen (ed) J, 2017a. Greenland – DMI historical climate data collection 1784–2016. DMI Technical report 17-04, Danish Meteorological Institute.

Cappelen (ed) J, 2017b. Weather observations from Greenland 1958–2016, DMI Technical report 17-08, Danish Meteorological Institute.

Cappelen J, Vraae Jørgensen B, Vaarby Laursen E, Sligting Stannius L, Sjølin Thomsen R, 2001. The observed climate of Greenland, 1958–99 – with climaticological standard normals, 1961–90. DMI Technical Report 00-18, Danish Meteorological Institute.

Carslaw H S, Jaeger J C, 1959. Conduction of Heat in Solids. 2nd ed., 510 pp., Clarendon, Oxford, England.

Christiansen H H, Humlum O, 2000. Permafrost. In: Holm, Jakobsen J, Böcher N, Nielsen R, Guttesen O, Humlum O, Jensen E (eds). Topografisk Atlas Grønland Det Kongelige Geografiske Selskab og Kort and Matrikelstyrelsen, 32– 35.

Claesson Liljedahl L, Kontula A, Harper J, Näslund J O, Selroos J O, Pitkänen P, Puigdomenech I, Hobbs M, Follin S, Hirschorn S, Jansson P, Kennell L, Marcos N, Ruskeeniemi T, Tullborg E L, Vidstrand P, 2016. The Greenland Analogue Project: Final report. SKB TR-14-13, Svensk Kärnbränslehantering AB.

Claesson Liljedahl L, Meierbachtol T, Harper J, van As D, Näslund J O, Selroos J O, Saito J, Follin S, Ruskeeniemi T, Kontula A, Humphrey N, 2021. Rapid and Sensitive Response of Greenland's Groundwater System to Ice-Sheet Change. Nature Geoscience 14, 751–755.

Colgan W, Wansing A, Mankoff K, Lösing M, Hopper J, Louden K, Ebbing J, Christiansen F G, Ingeman-Nielsen T, Claesson Liljedahl L, MacGregor J A, Hjartarson Á, Bernstein S, Karlsson N B, Fuchs S, Hartikainen J, Liakka J, Fausto R, Dahl-Jensen D, Bjørk A, Näslund J O, Mørk F, Martos Y, Balling N, Funck T, Kjeldsen K K, Petersen D, Gregersen U, Dam G, Nielsen T, Khan A, Løkkegaard A, 2022. Greenland Geothermal Heat Flow Database and Map (Version 1). Earth Systems Science Data 14, 2209–2238.

Csatho B M, Van der Veen C J, Tremper C M, 2005. Trimline mapping from multispectral Landsat ETM+ imagery. Géographie physique et Quaternaire 59, 49–62.

Dansgaard W, Johnsen S J, Clausen H B, Dahl-Jensen D, Gundestrup N S, Hammer C U, Hvidberg C S, Steffensen J P, Sveinbjörnsdottir A E, Jouzel J, Bond G, 1993. Evidence for general instability of past climate from a 250-kyr ice-core record. Nature 364, 218–220.

Dahl-Jensen D, Mosegaard K, Gundestrup N, Clows G D, Johnsen J, Hansen A W, Balling N, 1998. Past Temperatures Directly from the Greenland Ice Sheet. Science 282 (5387), 268–271. doi: 10.1126/science.282.5387.268

Dietrich R, Rülke A, Scheinert M, 2005. Present-day vertical crustal deformations in West Greenland from repeated GPS observations. Geophysical Journal International 163, 865–874.

Engels S, Helmens K, 2010. Holocene environmental changes and climate development in Greenland SKB R-10-65, Svensk Kärnbränslehantering AB.

Engström J, Paananen M, Klint K E, 2012. The Greenland Analogue Project. Geomodel version 1 of the Kangerlussuaq area on Western Greenland. Posiva Working Report 2012-10, Posiva Oy, Finland.

Ettema J, Van den Broeke M R, Van Meijgaard E, Van de Berg W J, Bamber J L, Box J E, Bales R C, 2009. Higher surface mass balance of the Greenland ice sheet revealed by high resolution climate modeling, Geophysical Research Letters 36, L12501., doi:10.1029/2009GL038110

Fausto R S, Ahlstrøm A P, van As D, Bøggild C E, Johnsen S J, 2009. A new present-day temperature parameterization for Greenland. Journal of Glaciology 55, 95–105.

Fettweis X, Tedesco M, van den Broeke M, Ettema, J, 2011. Melting trends over the Greenland ice sheet (1958–2009) from spaceborne microwave data and regional climate models. The Cryosphere, 5, 359–375.

Fitzpatrick A A W, Hubbard A L, Box J E, Quincey D J, van As D, Mikkelsen A P B, Doyle S H, Dow C F, Hasholt B, Jones G A, 2014. A decade (2002–2012) of supraglacial lake volume estimates across Russell Glacier, West Greenland. The Cryosphere 8, 107–121.

Forman S L, Marín L, van Der Veen C, Tremper C, Csatho B, 2007. Little Ice Age and neoglacial landforms at the inland ice margin, Isunguata Sermia, Kangerlussuaq, west Greenland. Boreas 36, 341–351.

Fredskild B, Funder S V, Larsen H C, 1989. Quaternary geology of the ice-free areas and adjacent shelves of Greenland. Quaternary geology of Canada and Greenland. In Fulton R J (ed). Quaternary geology of Canada and Greenland. Geological Survey of Canada, Geology of Canada, 743–792.

French H M, 2007, The periglacial environment. John Wiley and Sons Ltd. DOI:10.1002/9781118684931

Funder S, Hansen L, 1996. The Greenland ice sheet – a model for its culmination and decay during and after the last glacialmaximum. Bulletin of the Geological Society of Denmark 42, 137–152.

Ganopolski A, Calov R, Claussen M, 2010. Simulation of the last glacial cycle with a coupled climate ice-sheet model of intermediate complexity. Climate of the Past 6, 229–244.

Garde A A, Hollis J A, 2010. A buried Paleoproterozoic spreading ridge in the northern Nagssugtoqidian orogen, West Greenland. Geological Society, London, Special Publications 338, 213–234.

Goodrich, L E, 1978. Some results of a numerical study of ground thermal regimes, in 'Proceedings of the Third International Conference on Permafrost, Edmonton, Canada, 10 July 1978, 30–34.

Greve R, 1997. Application of a polythermal three-dimensional ice-sheet model to the Greenland ice sheet: response to steady-state and transient climate scenarios. Journal of Climate 10, 901–918.

Greve R, 2005. Relation of measured basal temperatures and the spatial distribution of the geothermal heat flux for the Greenland ice sheet. Annals of Glaciology 42, 424–432.

Greve R, 2019. Geothermal heat flux distribution for the Greenland ice sheet, derived by combining a global representation and information from deep ice cores. Polar Data Journal 3, 22–36.

Greve R, Saito F, Abe-Ouchi A, 2011. Initial results of the SeaRISE numerical experiments with the models SICOPOLIS and IcIES for the Greenland ice sheet. Annals of Glaciology 52, 23–30.

Hanna E, Huybrechts P, Steffen K, Cappelen J, Huff R, Shuman C, Irvine-Fynn T, Wise S, Griffiths M, 2008. Increased runoff from melt from the Greenland Ice Sheet: a response to global warming. Journal of Climate, 21, 331–341.

Harper J, Hubbard A, Ruskeeniemi T, Claesson Liljedahl L, Lehtinen A, Booth A, Brinkerhoff D, Drake H, Dow C, Doyle S, Engström J, Fitzpatrick A, Frape S, Henkemans E, Humphrey N, Johnson J, Jones G, Joughin I, Klint K E, Kukkonen I, Kulessa B, Landowski C, Lindbäck K, Makahnouk M, Meierbachtol T, Pere T, Pedersen K, Pettersson R, Pimentel S, Pimentel S, Quincey D, Tullborg E-L, van As D, 2011. The Greenland Analogue Project. Yearly report 2010. SKB R-11-23, Svensk Kärnbränslehantering AB.

Harper J, Hubbard A, Ruskeeniemi T, Claesson Liljedahl L, Kontula A, Hobbs M, Brown J, Dirkson A, Dow C, Doyle S, Drake H, Engström J, Fitzpatrick A, Follin S, Frape S, Graly J, Hansson K, Harrington J, Henkemans E, Hirschorn S, Humphrey N, Jansson P, Johnson J, Jones G, Kinnbom P, Kennell L, Klint K E, Liimatainen J, Lindbäck K, Meierbachtol T, Pere T, Pettersson R, Tullborg E-L, van As D, 2016. The Greenland Analogue Project: Data and Processes. SKB R-14-13, Svensk Kärnbränslehantering AB.

Harper J, Meierbachtol T, Humphrey N, , 2019. Greenland ICE project. Final report. SKB R-18-06, Svensk Kärnbränslehantering AB.

Hartikainen J, 2006. Numerical simulation of permafrost depth at Olkiluoto. Posiva Working Report 2006-52, Posiva Oy.

Hartikanen J, 2012. Simulations of permafrost evolution at Olkiluoto. Posiva Working Report 2012-34, Posiva Oy, Finland.

Hartikanen J, 2018. Continuum thermodynamic modelling of porous medium with application to ground freezing. PhD thesis. Aalto University, Finland.

Hartikainen J, Kouhia R, Wallroth T, 2010. Permafrost simulations at Forsmark using a numerical 2D thermo-hydro-chemical model. SKB TR-09-17, Svensk Kärnbränslehantering AB.

Henriksen N, Higgins A K, Kalsbeek F, Pulvertaft T C R, 2000. Greenland from Archean to Quaternary: Descriptive text to the geological map of Greenland, 1:2 500 000: Geology of Greenland Survey Bulletin 185.

Hinkel K M, Klene A E, Nelson F E, 2008. Spatial and interannual patterns of winter n-factors near Barrow, Alaska. In 'Proceedings of the Ninth International Conference on Permafrost', Fairbanks University of Alaska, 705–709.

Howat I M, Negrete A, Smith B E, 2014. The Greenland Ice Mapping Project (GIMP) land Classification and surface elevation datasets. The Cryosphere 8, 1509–1518.

Howat I M, Negrete A, Smith B, 2015. MEaSURES Greenland Ice Mapping Project. Digital Elevation Model. Version 1. Boulder, Colorado USA. NASA National Snow and Ice Data Center Distributed Active Archive Center.

Huber C, Leuenberger M, Spahni R, Flückiger J, Schwander J, Stocker T F, Johnsen S, Landais A, Jouzel J, 2006. Isotope calibrated Greenland temperature record over Marine Isotope Stage 3 and its relation to CH4. Earth and Planetary Science Letters, 243, pp 504–519.

Huybrechts P, 2002. Sea-level changes at the LGM from ice-dynamic reconstructions of the Greenland and Antarctic ice-sheets during the glacial cycles. Quaternary Science Reviews 21, 203–231.

Johannessen O M, Khvorostovsky K, Miles M W, Bobylev L P, 2005. Recent ice-sheet growth in the interior of Greenland. Science 310, 1013–1016.

Johansson E, Berglund S, Lindborg T, Petrone J, van As D, Gustafsson L-G, Näslund J-O, Laudon H, 2015a. Hydrological and meteorological investigations in a periglacial lake catchment near Kangerlussuaq, west Greenland – presentation of a new multi-parameter dataset. Earth System Science Data 7, 93–108.

Johansson E, Gustafsson L-G, Berglund S, Lindborg T, Selroos J-O, Claesson Liljedahl L, Destouni G, 2015b. Data evaluation and numerical modeling of hydrological interactions between active layer, lake and talik in a permafrost catchment, Western Greenland. Journal of Hydrology 527, 688–703.

Johansson E, 2016. The influence of climate and permafrost on catchment hydrology. PhD thesis. Stockholm University.

Joughin I, Smith B E, Howat I M, Scambos T, Moon T, 2010. Greenland flow variability from ice-sheet-wide velocity mapping. Journal of Glaciology 56, 415–430.

Jørgensen A S, Andreasen F, 2007. Mapping of permafrost surface using ground-penetrating radar at Kangerlussuaq Airport, western Greenland. Cold Regions Science and Technology 48, 64–72.

Kade A, Romanovsky V E, Walker D A, 2006. The n-factor of nonsorted circles along a climate gradient in Arctic Alaska. Permafrost and Periglacial Processes, 17, 279–289.

Kane D L, Yoshikawa K, McNamara J P, 2013. Regional groundwater flow in an area mapped as continuous permafrost, NE Alaska (USA). Hydrogeology Journal 21, 41–52.

Karunaratne, K C, Burn, C R, 2003. Freezing n-factors in discontinuous permafrost terrain near Mayo, Yukon Territory. In Proceedings of the 8th International Conference on Permafrost. Zurich: University of Zurich-Irche, 519–524.

Karunaratne K C, Burn C R, 2004. Relations between air and surface temperature in discontinuous permafrost terrain near Mayo, Yukon Territory. Canadian Journal of Earth Sciences, 41, 1437–1451.

Karunaratne K C, Kokelj C R, Burn C R, 2008. Near-surface permafrost conditions near Yellowknife, Northwest Territories, Canada. In Proceedings of the Ninth International Conference on Permafrost, University of Alaska Fairbanks, 29 June –3 July 2008, 907–912.

Kleman J, Stroeven, Lundqvist J, 2008. Patterns of Quaternary ice-sheet erosion and deposition in Fennoscandia and a theoretical framework for explanation. Geomorphology 97, 73–90.

Klene A E, 2008. Interannual variability of winter n-factors in the Kuparuk river basin, Alaska. In Proceedings of the Ninth International Conference on Permafrost, University of Alaska Fairbanks, 29 June – 3 July 3 2008, 953–958.

Klene A E, Nelson F E, Shiklomanov N I , Hinkel K M, 2001. The N-factor in natural landscapes: Variability of air and soil-surface temperatures, Kuparuk River Basin, Alaska. Arctic, Antarctic, and Alpine Research, 33, 140–148.

Kobashi T, Menviel L, Jeltsch-Thömmes A, Vinther B M, Box J E, Muscheler R, Nakaegawa T, Pfister P L, Döring M, Leuenberger M, Wanner H, Ohmura A, 2017. Volcanic influence on centennial to millennial Holocene Greenland temperature change, Scientific Reports 7, 1441. doi:10.1038/s41598-017-01451-7

Kouhia R, 1999. Techniques for the analysis of non-linear systems – with applications to solid and structural mechanics. PhD thesis. Helsinki University of Technology, Finland.

Krabill W, Abladati W, Frederick E, Manizade S, Martin C, Sonntag J, Swift R, Thomas R, Wright W, Yungel J, 2000. Greenland Ice Sheet: High-elevation balance and peripheral thinning. Science 289, 428–430.

Kukkonen I T, Jõeleht A, 2003. Weichselian temperatures from geothermal heat flow data. Journal of Geophysical Research: Solid Earth 108. doi:10.1029/2001JB001579

Kukkonen I T, Rath V, Kivekäs L Šafanda J, Čermak V, 2011. Geothermal studies of the Outokumpu Deep Drill Hole, Finland: Vertical variation in heat flow and palaeoclimatic implications. Physics of the Earth and Planetary Interiors 188, 9–25.

Landais A, Jouzel J, 2006. Isotope calibrated Greenland temperature record over Marine Isotope Stage 3 and its relation to CH_4. Earth and Planetary Science Letters 243, 504–519.

Levy L B, Kelly M A, Howley J A, Virginia R A, 2012. Age of the Ørkendalen moraines, Kangerlussuaq, Greenland: constraints of the extent of the southwestern margin of the Greenland Ice Sheet during the Holocene. Quaternary Science Reviews 52, 1–5.

Levy L B, Kelly M A, Applegate P A, Howley J A, Virginia R A, 2018. Middle to late Holocene chronology of the western margin of the Greenland Ice Sheet: A comparison with Holocene temperature and precipitation records. Arctic, Antarctic, and Alpine Research 50. doi: 10.1080/15230430.2017.1414477

Liakka J. Löfverström M, Colleoni F, 2016. The impact of the North American glacial topography on the evolution of the Eurasian ice-sheet over the last glacial cycle. Climate of the Past 12, 1225–1241.

Lindbäck K, Pettersson R, Doyle S H, Helanow C, Jansson P, Savstrup Kristensen S, Stenseng L, Forsberg R, Hubbard A L, 2014. High-resolution ice thickness and bed topography of a land-terminating section of the Greenland Ice Sheet. Earth System Science Data Discussions 7, 129–148.

Lisiecki L E, Raymo M E, 2005. A Pliocene-Pleistocene stack of 57 globally distributed benthic $d^{18}O$ records. Paleoceanography 20, PA1003. doi:10.1029/2004PA001071

Lofverstrom M, Liakka J, 2018. The influence of atmospheric grid resolution in a climate model-forced ice-sheet simulation. The Cryosphere 12, 1499–1510.

Lunardini V J, 1978. Theory of n-factors and correlation of data. In Proceedings of the 3rd International Conference on Permafrost, Edmonton, Canada, 10–13 July 1978, 40–46.

Mayborn K R, Lesher C E, 2006. Origin and evolution of the Kangâmiut mafic dyke swarm, West Greenland. Geological Survey of Denmark and Greenland Bulletin 11, 61–86.

Mikkola M, Hartikainen J, 2001. Mathematical model of soil freezing and its numerical implementation. International Journal of Numerical Methods in Engineering 52, 543–557.

Mikkola M, Hartikainen J. 2002. Computational aspects of soil freezing problem. In Huyghe J, Raats P, Cowin S C (eds). Proceedings of the Fifth World Congress on Computational Mechanics, Vienna, 7–12 July 2002.

Nielsen L T, Aðalgeirsdóttir G, Gkinis V, Nuterman R, Hvidberg C S, 2018. The effect of a Holocene climatic optimum on the evolution of the Greenland ice sheet during the last 10 kyr. Journal of Glaciology 64, 477–488.

Näslund J O, Jansson P, Fastook J L, Johnson J, Andersson L, 2005. Detailed spatially distributed geothermal heat flow data for modelling of basal temperatures and melt water production beneath the Fennoscandian ice-sheet. Annals of Glaciology 40, 95–101.

Palmer S, Shepherd A, Nienow P, Joughin I, 2011. Seasonal speedup of the Greenland Ice Sheet linked to routing of surface water. Earth and Planetary Science Letters 302, 423–428.

Petrone J, 2018. Regional surface regolith analysis. Kangerlussuaq region, Western Greenland. WSP Sverige AB. SKBdoc 1888215 ver 1.0, Svensk Kärnbränslehantering AB.

Petrone J, Sohlenius G, Johansson E, Lindborg T, Näslund J-O, Strömgren M, Brydsten L, 2016. Using ground-penetrating radar, topography and classification of vegetation to model the sediment and active layer thickness in a periglacial lake catchment, western Greenland. Earth System Science Data 8, 663–677.

Porter S C, 1989. Some geological implications of average Quaternary glacial conditions. Quaternary Research 32, 245–261.

Robinson A, Goelzer H, 2014. The importance of insolation changes for paleo ice-sheet modeling. The Cryosphere 8, 1419–1428.

Ruskeeniemi T, Engström J, Lehtimäki J, Vanhala H, Korhonen K, Kontula A, Claesson Liljedahl L, Näslund J-O, Pettersson R, 2018. Subglacial permafrost evidencing readvance of the Greenland Ice Sheet over frozen ground. Quaternary Science Reviews 199, 174–187.

Rückamp M, Greve R, Humbert A, 2019. Comparative simulations of the evolution of the Greenland ice sheet under simplified Paris Agreement scenarios with the models SICOPOLIS and ISSM. Polar Science 21, 14–25.

Scholz H, Baumann M, 1997. An "open system pingo" near Kangerlussuaq (Søndre Strømfjord), West Greenland. Geology of Greenland Survey Bulletin 176, 104–108.

Schwanghart W, Kuhn N J, 2010. TopoToolbox: A set of Matlab functions for topographic analysis. Environmental Modelling & Software 25, 770–781.

SeaRISE partners, 2008. Assessing ice-sheet contributions to sea level through the 21st century, SeaRISE White Paper.Available at: http://websrv.cs.umt.edu/isis/index.php/SeaRISE White Paper

SKB, 2006. Climate and climate-related issues for the safety assessment SR-Can. SKB TR-06-23, Svensk Kärnbränslehantering AB.

SKB, 2010. Climate and climate related issues for the safety assessment SR-Site. SKB TR-10-49, Svensk Kärnbränslehantering AB.

SKB, 2011. Long-term safety for the final repository for spent nuclear fuel at Forsmark. Main report of the SR-Site project. SKB TR-11-01, Svensk Kärnbränslehantering AB.

SKB, 2014. Climate and climate-related issues for the safety assessment SR-PSU. SKB TR-13-05, Svensk Kärnbränslehantering AB.

SKB, 2019. Climate and climate-related issues for the safety evaluation SE-SFL. SKB TR-19-04, Svensk Kärnbränslehantering AB.

SKB, 2020. Post-closure safety for the final repository for spent nuclear fuel at Forsmark. Climate and climate-related issues, PSAR version. SKB TR-20-12, Svensk Kärnbränslehantering AB.

Sole A, Nienow P, Bartholomew I, Mair D, Cowton T, Tedstone A, King M A, 2013. Winter motion mediates dynamic response of the Greenland Ice Sheet to warmer summers. Geophysical Research Letters 40, 3940–3944.

Steffen K, Box J E, Abdalati W, 1996. Greenland Climate Network: GC-Net. In Colbeck S C (ed). Glaciers, ice-sheets and volcanoes: a tribute to Mark F. Meier. Special Report 96-27, Cold Regions Research & Engineering Laboratory, 98–103.

Storms J E A, de Winter I L, Overeem I, Drijkoningen G G, Lykke-Andersen H, 2012. The Holocene sedimentary history of the Kangerlussuaq Fjord-valley fill, West Greenland. Quaternary Science Reviews 35, 29–50.

Tarasov L, Peltier R W, 2002. Greenland glacial history and local geodynamic consequences. Geophysical Journal International 150, 198–229.

Ten Brink N W, 1975. Holocene history of the Greenland ice sheet based on radiocarbon-dated moraines in West Greenland. Kobenhavn: Kommissionen for Videnskabelige Undersogelse.

Ten Brink N W, 1974. Glacio-isostacy: new data from west Greenland and geophysical implications. Geological Society of America Bulletin 85, 219–228.

Ten Brink N W, Weidick A, 1974. Greenland Ice Sheet History Since the Last Glaciation. Quaternary Research 4, 429–440.

van Angelen J H, Lenaerts J T M, Lhermitte S L, Fettweis X, Kuipers Munneke P, van den Broeke M R, van Meijgaard E, Smeets C J P P, 2012. Sensitivity of Greenland Ice Sheet surface mass balance to surfacealbedo parameterization: a study with a regional climate model. The Cryosphere 6, 1175–1186.

van Angelen J H, van den Broeke M R, Wouters B, Lenaerts J T M, 2014. Contemporary (1960–2012) evolution of the climate and surface mass balance of the Greenland Ice Sheet. Surveys in Geophysics 35, 1155–1174.

van As D, Fausto R S, PROMICE Project Team, 2011. Programme for monitoring of the Greenland Ice Sheet (Promice): first temperature and ablation records, Geological Survey of Denmark and Greenland Bulletin 23, 73–76.

van As D, Hubbard A L, Hasholt B, Mikkelsen A B, van den Broeke M R, Fausto R S, 2012. Large surface meltwater discharge from the Kangerlussuaq sector of the Greenland ice sheet during the record-warm year 2010 explained by detailed energy balance observations. The Cryosphere 6, 199–209.

van den Broeke M R, Gallée H, 1996. Observation and simulation of barrier winds at the western margin of the Greenland ice sheet. Quarterly Journal of the Royal Meteorological Society 122, 1365–1383.

van Gool J A M, Alsop G I, Árting U E, Garde A A, Knudsen C, Krawiec A W, Mazur S, Nygaard J, Piazolo S, Thomas C W, Thrane K, 2002b. Precambrian geology of the northern Nagssugtoqidian orogen, West Greenland: mapping in the Kangaatsiaq area. Geology of Greenland Survey Bulletin 191, 13–23.

van Tatenhove F G M, Olesen O B, 1994. Ground temperature and related permafrost characteristics in West Greenland. Permafrost and Periglacial Processes 5, 199–215.

van Tatenhove F G, Van der Meer J J M, Koster E A, 1996. Implications for deglaciation chronology from new AMS-age determinations in West Greenland. Quaternary Research 45, 245–253.

van de Wal R S W, Boot W, van den Broeke M R, Smeets C J P P, Reijmer C H, Donker J J A, Oerlemans J, 2008. Large and rapid melt-induced velocity changes in the ablation zone of the Greenland Ice Sheet. Science 321, 111–113.

van de Wal R S W, Boot W, Smeets C J P P, Snellen H, van den Broeke M R, Oerlemans J, 2012. Twenty-one years of mass balance observations along the K-transect, West Greenland. Earth System Science Data 4, 31–35.

Vidstrand P, 2017. Concept testing and site-scale groundwater flow modelling of the ice-sheet marginal-area of the Kangerlussuaq region, Western Greenland. SKB R-15-01, Svensk Kärnbränslehantering AB.

Vinther B M, Buchardt S L, Clausen H B, Dahl-Jensen D, Johnsen S D, Fisher D A, Koerner R M, Raynaud D, Lipenkov V, Andersen K K, Blunier T, Rasmussen S O, Steffensen J P, Svensson A M, 2009. Holocene thinning of the Greenland ice sheet. Nature 461, 385–388.

Wahr J, van Dam T, Larson K, Francis O, 2001. Geodetic measurements in Greenland and their implications. Journal of Geophysical Research: Solid Earth 106, 16567–16581.

Weidick A, 1993. Neoglacial change of ice cover and the related response of the Earth's crust in west Greenland. Rapport Grønlands Geologiske Undersøgelse 159, 121–126.

Weidick A, 1996. Late Holocene and historical changes of glacier cover and related relative sea level in Greenland. Zeitschrift fur Gletscherkunde und Glazialgeologie 32, 217–224.

White D, Hinzman L, Alessa L, Cassano J, Chambers M, Falkner K, Francis J, Gutowski Jr W J, Holland M, Holmes R M, Huntington H, Kane K, Kliskey A, Lee C, McClelland J, Peterson B, Rupp T S, Straneo F, Steele M, Woodgate R, Yang D, Yoshikawa K, Zhang T, 2007. The arctic freshwater system: Changes and impacts. Journal of Geophysical Research: Biogeosciences 112, G04S54. doi:10.1029/ 2006JG000353

Willemse N W, Koster E A, Hoogakker B, van Tatenhove F G M, 2003. A continuous record of Holocene eolian activity in West Greenland. Quaternary Research 59, 322–334.

Williams P, Smith M, 1989. The frozen earth: fundamentals of geocryology. Cambridge: Cambridge University Press.

Wilson R W, Klint K E S, Van Gool J M, McCaffrey K J W, Holdsworth R E, Chalmers J A, 2006. Faults and fractures in central West Greenland: onshore expression of continental break-up and sea-floor spreading in the Labrador–Baffin Bay Sea. Geological Survey Of Denmark And Greenland Bulletin 11, 185–204.

Yershov E D, 1998. General geocryology. Cambridge: Cambridge University Press.

Young N E, Briner J P, 2015. Holocene evolution of the western Greenland Ice Sheet: Assessing geophysical ice-sheet models with geological reconstructions of ice-margin change. Quaternary Science Reviews 114, 1–17.

Appendix 1

Ice-sheet surface and basal conditions

During times of glaciated conditions at the GAP site, the permafrost model, described in Section 3.1, needs basal ice temperatures as thermal surface boundary condition. Since there is no palaeo-information on basal temperatures, such data need to come from model simulations. In this section, we describe the ice-sheet model simulations used as input to the permafrost experiments. In Section A1.1, the ice-sheet model and the experimental design is outlined. Section A1.2 describes the reference simulation used as input in the permafrost test cases (Section 3.3.3). Sections A1.3 and A1.4 discusses, and quantifies, the uncertainties related to the simulated basal temperatures. These include the uncertainties related to the spatial (Section A1.3) variability of the geothermal heat flux and the surface climate representation (Section A1.4).

A1.1 Ice-sheet model description and experimental design

The basal temperature was estimated using the 3D thermomechanical ice-sheet model SICOPOLIS (SImulation COde for POLythermal Ice-Sheets, version 3.0). The model is subjected to the shallow-ice approximation, meaning that only the lower order terms describing the ice flow are retained, while higher order terms, describing e.g. the detailed dynamics of ice streams and ice shelves, are neglected. The model is forced by MAAT and precipitation at the ice-sheet surface, and a prescribed representation of the geothermal heat flux beneath the ice-sheet. The governing equations of SICOPOLIS are described in detail in e.g. Greve (1997) and Greve et al. (2011). SICOPOLIS has been widely used for various palaeo-applications (e.g. Calov et al. 2005, Ganopolski et al. 2010, Robinson and Goelzer 2014, Liakka et al. 2016, Lofverstrom and Liakka 2018), and for analysing the present-day and future evolution of the Greenland ice sheet (GrIS) (e.g. Greve 2007, Greve et al. 2011, Applegate et al. 2012, Rückamp et al. 2019).

The model configuration in the present study is based on the experiments conducted by Applegate et al. (2012), which in turn were adopted from SeaRISE partners (2008) and Greve et al. (2011). The simulations use a 10 × 10 km horizontal resolution and 81 terrain-following vertical model levels. The spatial distributions of Greenland air temperature and precipitation are parameterised using the equations in Fausto et al. (2009), and the time-dependent air temperature changes of the last glacial cycle are taken to be proportional to the δ^{18}O variation of the GRIP ice core record (e.g. Dansgaard et al. 1993), following the methodology in Huybrechts (2002) and Greve et al. (2011). Changes in precipitation are assumed to be exponentially proportional to the air temperature changes (Greve et al. 2011). Ice extent is restricted to land areas, which means that ice spreading over ocean grid cells is immediately removed. The simulations start at 125 ka BP and are first spun up until 20 ka BP. Subsequent to this spin-up period, the model is integrated from 20 ka BP until present-day to compute the basal temperatures that are used as input to the permafrost simulations.

Table A1-1. Summary of the SICOPOLIS simulations performed in this study.

Simulation name	Description
Reference simulation	This simulation uses the same parameter values as in Applegate et al. (2012), except for a spatially variable (instead of a spatially uniform) representation of geothermal heat flux based on Greve (2019).
Sensitivity simulation	This simulation uses spatially uniform geothermal heat flux with local GAP anomaly compared to the reference simulation with the aim to address the uncertainty related to the spatial distribution of geothermal heat flux in the Greve (2019) dataset.

A1.2 Reference simulation

In this section, we describe the reference SICOPOLIS simulation (Table A1-1), used as input in the permafrost test cases (Section 3.3.3).

A major constraint of the ice-sheet simulations in this study is that they should result in approximately correct representation of the present-day location of the ice-sheet margin in the region of the GAP site, i.e. the ice-sheet margin should be situated directly east of the DH-GAP04 proglacial bedrock drill site (Claesson Liljedahl et al. 2016). Another important constraint is that the DH-GAP04 bedrock drill site should be ice-covered throughout most of the last glacial cycle, including the LGM, and that the deglaciation of the DH-GAP04 site should occur during the Middle Holocene at around 7–6 ka BP.

Applegate et al. (2012) conducted 100 ensemble simulations of the GrIS from 125 ka BP to 3500 AD. Each simulation used different combinations of the following model parameters: flow enhancement factor (E_f), melting coefficients for snow and ice (β_{snow} and β_{ice}), basal sliding factor (C_s) and geothermal heat flux (Q_{geo}). All other parameters were set identical as in Greve et al. (2011).

Here, we choose the parameter values of E_f, β_{snow}, β_{ice} and C_s corresponding to ensemble number 92 in Applegate et al. (2012) (Table A1-2), since this simulation was found to yield an approximately correct location of the modelled present-day ice-sheet margin near the DH-GAP04 drill site (the simulated ice-margin is located in the grid point adjacent to the drill site). However, whilst Applegate et al. (2012), in this ensemble simulation, used a spatially uniform Q_{geo} value of 32 mW m^{-2} over the entire Greenland domain, we use a spatially variable Q_{geo} distribution from the dataset developed by Greve (2019) (Figure A1-1). This dataset was compiled based on available Q_{geo} measurements across Greenland, including the measurements at the GAP site (average value of 31 mW m^{-2}, see Claesson Liljedahl et al. 2016). Hence, by replacing the uniform Q_{geo} value used in Applegate et al. (2012) with the Greve (2019) dataset, we ensure that i) the basal ice temperatures are calculated with the most up-to-date information available for Greenland Q_{geo} , ii) the basal ice temperatures at the GAP site are computed using the local value of Q_{geo} for that site (which are lower than for other Q_{geo} observations in Greenland), and iii) that Q_{geo} elsewhere on Greenland are generally higher than the low value of the GAP site.

The present-day GrIS thickness in the reference simulation is shown in Figure A1-2 (left). It is evident that the reference simulation results in too little ice in northern Greenland. However, the location of the simulated present-day ice margin in the region of the DH-GAP04 drill site, which is most relevant for this study, agrees with observations.

Table A1-2. Parameter values used in this study, adopted from ensemble number 92 in Applegate et al. (2012). The representation of the geothermal heat flux (Q_{geo}) is based on Greve (2019), see the text. All other parameters are set identical as in Greve et al. (2011). How the parameters are treated in SICOPOLIS is described in Greve (1997) and Greve et al. (2011).

Variable		Value
Positive degree-day factor for snow (mm water equiv. day^{-1} $°C^{-1}$)	β_{snow}	2.77
Degree-day factor for ice (mm water equiv. day^{-1} $°C^{-1}$)	β_{ice}	13.1
Ice-flow enhancement factor (dimensionless)	E_f	1.80
Basal sliding factor (m yr^{-1} Pa^{-1})	C_s	3.40

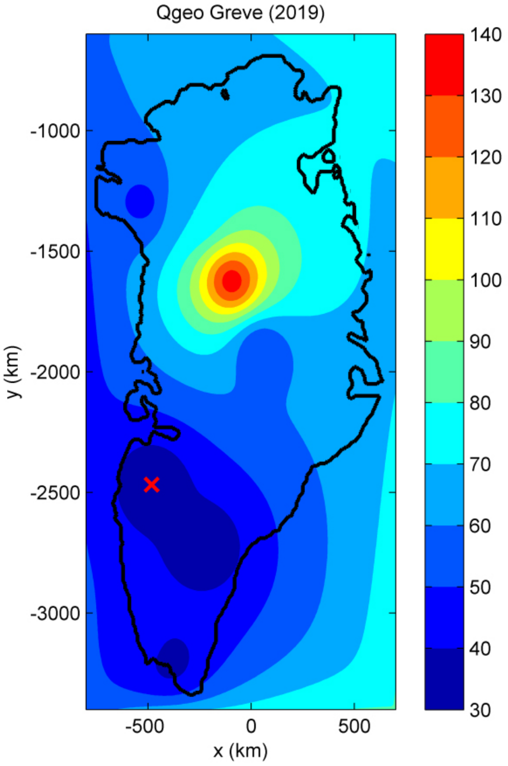

Figure A1-1. *Greenland geothermal heat flux (mW m^{-2}) from Greve (2019), used as input to the ice-sheet reference SICOPOLIS simulation (Table A1-1). The GAP site is indicated by a red cross and has a Q_{geo} value of 31 mW m^{-2} (see also Claesson Liljedahl et al. 2016).*

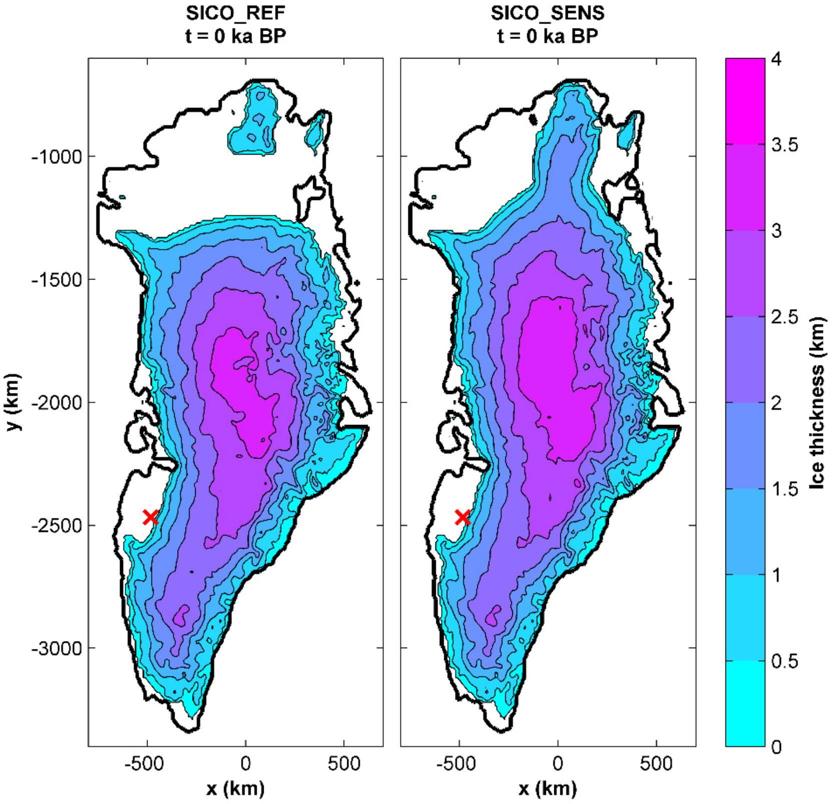

Figure A1-2. *Present-day ice thickness in the reference (left) and sensitivity (right) SICOPOLIS simulations, following simulations of the last 125 ka. The DH-GAP04 drill site is indicated by a red cross.*

The evolution of the ice-sheet thickness and basal temperature in the region of the DH-GAP04 drill site during the spin-up of the reference simulation is shown in Figure A1-3 (black line). After the initial 10–20 ka, during which the ice-sheet thickness at the site fluctuates between 0 and ~ 1 500 m, the ice thickness stabilises at ~ 1 700 m at about 100 ka BP. Subsequently, the ice thickness remains relatively constant, only increasing marginally between 100 ka BP and 20 ka BP. During the same time period, the basal temperature exhibits a general decline from approximately −2 °C at 100 ka BP to −10 °C at 20 ka BP.

The corresponding evolution of the ice-sheet thickness and basal ice temperature in the region of the DH-GAP04 drill site between 20 ka BP and present-day is shown in Figure A1-4 (black line). The ice-sheet thickness and basal temperature remain relatively unchanged until ~ 10 ka BP, at which point the basal temperature begins to increase rapidly in association with a rapid drop in the ice-sheet thickness by the deglaciation. The site becomes completely deglaciated at around 7 ka BP, in general agreement with other data (see Claesson Liljedahl et al. 2016).

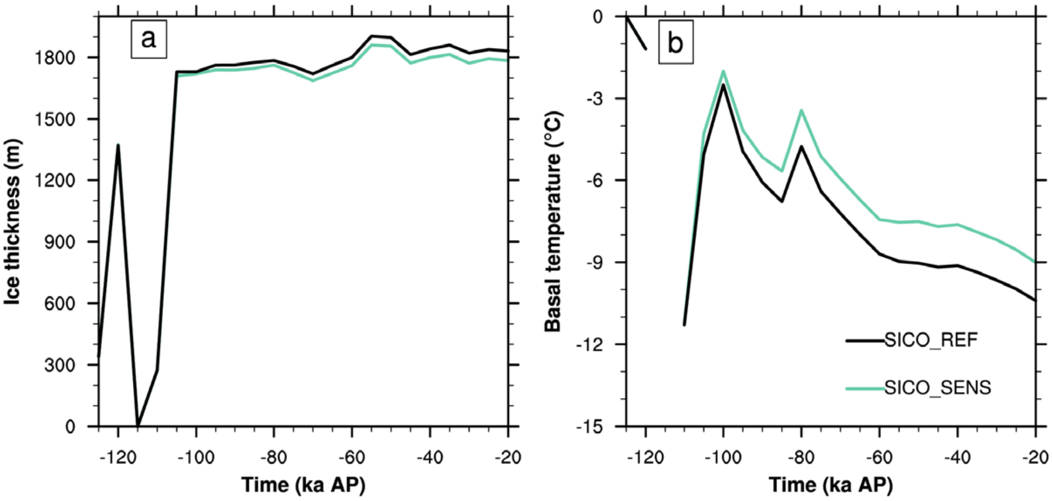

Figure A1-3. Evolution of ice thickness (a) and basal ice temperature (b) at the grid point closest to the DH-GAP04 drill site from 125 to 20 ka BP (i.e. the spin-up phase of the simulation). The black line corresponds to the reference simulation and the green line to the sensitivity simulation. The interruption in the basal-temperature evolution between 120 and 110 ka BP is explained by the fact that the GAP area is not ice-covered during this time (visualised by zero ice-sheet thickness at 115 ka BP in (a)).

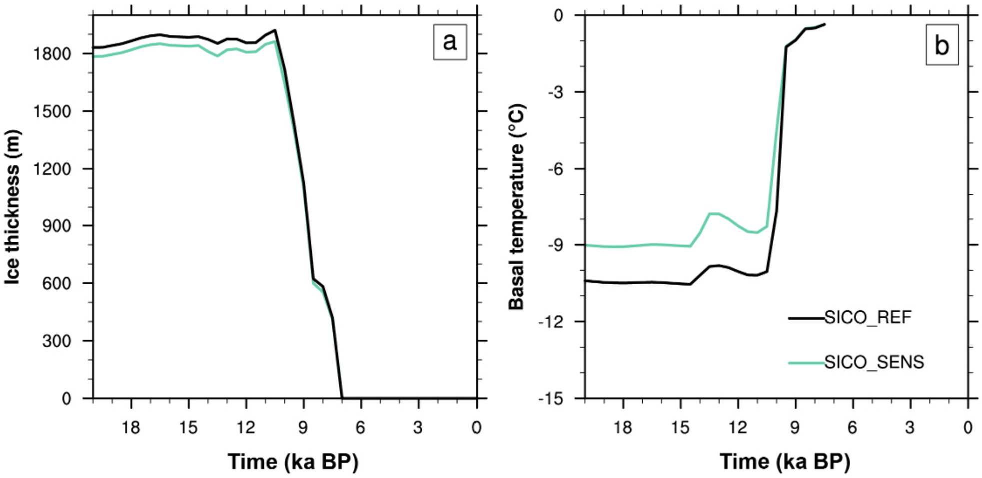

Figure A1-4. Evolution of ice thickness (a) and basal ice temperature (b) at the grid point closest to the DH-GAP04 drill site from 20 ka BP to present-day. The black line corresponds to the reference simulation and the green line to the sensitivity simulation.

A1.3 Evaluating the uncertainty related to the spatial distribution of geothermal heat flux (Qgeo)

The dataset by Greve (2019) includes the available observations of Q_{geo} across Greenland. However, the observations are very sparse, in summary only 8 observations. Between those few observational sites, the value of Q_{geo} was interpolated when producing the dataset. Therefore, due to the limited number of Q_{geo} observations, and the resulting large distance between those, there is great uncertainty related to the spatial coverage of each Q_{geo} value. For example, in Figure A1-1, it is suggested that the low Q_{geo} anomaly measured at the DH-GAP04 drill site extends a couple of hundred km beyond the drill site. However, since there is no solid information how far the low Q_{geo} value measured at GAP really extends beyond the site, it is possible that the spatial Q_{geo} coverage in Greve (2019) is overestimated. A smaller spatial extent of the low Q_{geo} anomaly at the GAP site could hence potentially allow for advection of warmer ice from regions upstream the site, resulting in higher basal temperatures than in reference simulation and, consequently, to higher bedrock temperatures in the permafrost model. In this context, it is worth noting that Q_{geo} with a very high spatial variability has been observed in Fennoscandia (Näslund et al. 2005), a region with similar types of bedrock as in Greenland.

To estimate an upper bound of the basal temperature at the DH-GAP04 drill site, resulting from advection of warmer ice upstream the site, we create a new Q_{geo} dataset. This dataset uses a uniform Q_{geo} value of 42 mW m^{-2} across entire Greenland *except* for the grid cell where GAP drill site is located, for which the observed Q_{geo} value of 31 mW m^{-2} (Claesson Liljedahl et al. 2016) is used. The surrounding value of 42 mW m^{-2} was chosen since it constitutes the maximum value upstream (east) of the DH-GAP04 area as found in a new evaluation of Greenland Q_{geo} based on seismic data (Artemieva 2019).

The new Q_{geo} dataset is used in a sensitivity simulation with SICOPOLIS (Table A1-1). Apart from Q_{geo}, the sensitivity simulations use identical parameters and boundary conditions as in the reference simulation (Section A1.2). In the sensitivity simulation*,* the resulting present-day GrIS thickness and ice-sheet margin position for the DH-GAP04 drill site area is very similar to that in the reference simulation (Figure A1-2).

The temporal evolution of basal ice temperature and ice-sheet thickness in the DH-GAP04 area in the sensitivity simulation is shown in Figure A1-3 (from 125 to 20 ka BP) and Figure A1-4 (from 20 to 0 ka BP). Subsequent to the initial ~20 ka of the spin-up, the basal ice temperature in simulation gradually diverges from the basal temperature in the reference simulation, culminating in a ~1.5 °C higher basal ice temperature at 20 ka BP (Figure A1-3). This difference in basal temperature between the sensitivity and reference simulations then remains approximately unchanged until 10 ka BP, after which the deglaciation of the GAP site is initiated. The timing of the completed deglaciation of the DH-GAP04 area is identical in the sensitivity simulation to the reference simulation.

In summary, it is estimated that advection of warmer ice upstream of the DH-GAP04 drill site, resulting from the uncertainty in the spatial distribution of Q_{geo} in Greve (2019), may contribute to increase in the basal temperature for the Dh-GAP04 drill site area by up to 1.5 °C. The simulated basal temperature from the sensitivity simulation is used as input in the permafrost test cases, see Section 3.3.3.

A1.4 Evaluating the uncertainty related to errors in the climate representation in the SICOPOLIS simulations

As described in Section A1.1, SICOPOLIS is forced by a relatively simple climate representation, for which the time-dependent variability of air temperature is assumed to be proportional to the GRIP $\delta^{18}O$ record (Huybrechts 2002, Greve et al. 2011). However, translating the $\delta^{18}O$ signal to air temperature is non-trivial, and may result in significant errors in the reconstructed air temperature. These errors may be larger for some time periods of the last glacial cycle than for others, in part resulting from a non-linear relation between $\delta^{18}O$ and air temperature (e.g. Huber et al. 2006). Furthermore, it has been argued that this methodology does not capture the temperature amplitude of some important climatic events during the latter part of the glacial cycle, e.g. the Holocene climate optimum, ~8–5 ka BP (Nielsen et al. 2018).

However, evaluating the impact of the uncertainties in surface air temperature on basal ice temperatures is a challenging task since small changes in the climate may break the constraint of the SICOPOLIS simulations stating that the present-day ice-sheet margin in the DH-GAP04 drill site area need to be simulated reasonably well (Section A1.2). Therefore, to obtain a crude *first-order* estimate of the maximum isolated impact of surface temperature changes on basal ice temperature, we perform steady-state simulations with a prescribed ice-sheet topography. The prescribed ice-sheet topography ensures that the ice-sheet thickness remains the same throughout the simulation and hence that the basal temperature is only influenced by the imposed air temperature perturbation at the surface and *not* by amplifying effects due to e.g. the temperature-lapse-rate feedback. Integrating to steady-state enables sufficient time for the imposed temperature anomaly at the surface to propagate to the ice-sheet bed, in the absence of other climate fluctuations, and therefore allows us to evaluate its maximum isolated impact on the basal ice temperature. The fixed ice-sheet topography and steady-state climate corresponds to the 20 ka BP time slice in the reference simulation.

From this sensitivity simulation, it can be seen that imposing a 1 °C warm and cold anomaly, respectively, at the ice-sheet surface results in ~0.5 °C temperature change in basal ice temperature DH-GAP04 drill site area after about 100 ka (Figure A1-5). Hence, it is here crudely estimated that half of the potential error in air temperature representation at the ice-sheet surface would be translated into a basal ice temperature error. However, as mentioned above, this estimate should be interpreted with caution. In reality, relatively small changes in surface air temperature could be amplified by the temperature-lapse-rate feedback as a result of changes in the local ice thickness. There are also other internal thermodynamic feed-back mechanisms in the ice-sheet system that are not accounted for in this simplified sensitivity experiment. Furthermore, real world climate and ice-sheets are not in steady-state, so having 100 ka of constant climate conditions is unrealistic. The results should thus be taken as a broad indication of the uncertainty introduced by climate representation errors in the SICOPOLIS simulations.

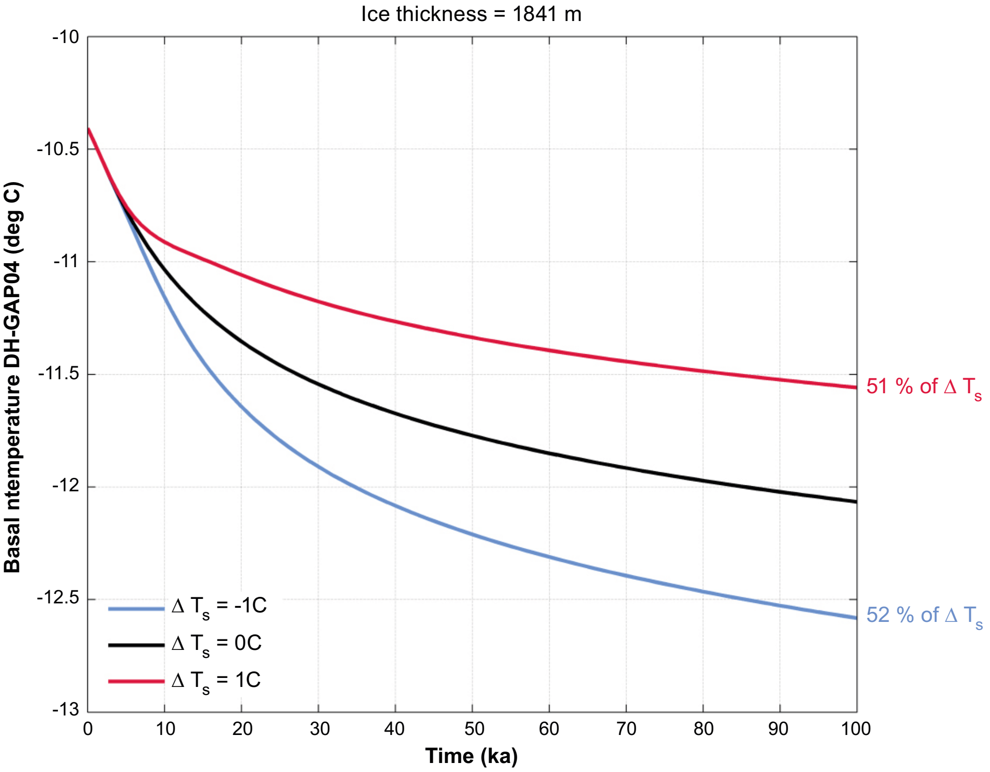

Figure A1-5. *Steady-state evolution of basal ice temperature in the reference SICOPOLIS simulation (black curve) and for an imposed +1 °C (red curve) and −1 °C (blue curve) air temperature perturbation at the ice-sheet surface. All simulations use fixed ice-sheet thickness and steady-state climate corresponding to 20 ka BP in the reference simulation.*

Appendix 2

Proglacial air temperature and surface conditions

A2.1 Proglacial MAAT

The proglacial Holocene MAAT for the DH-GAP01 site has been obtained by combining meteorological data from (i) the AWS KAN_B (DH-GAP01 site) (Van As et al. 2011, Johansson et al. 2015a), (ii) Kangerlussuaq and coastal sites in south–western Greenland (Cappelen et al. 2017a, b) and (iii) selected sites from the GrIS (Steffen et al. 1996), together with temperature proxy ice-core records of δ^{18}O (Vinther et al. 2009) and, argon and nitrogen isotopes (Kobashi et al. 2017).

Figure A2-1 shows three meteorological data sets of air temperature that have been used to reconstruct MAAT for the DH-GAP01 site for the recent history 1852–2017 AD (Common Era). The reconstruction involves three steps. First, the temperature data for the coastal sites in south–western Greenland for 1852–2017 AD (Cappelen et al. 2017a) has been used to reconstruct MAAT for Kangerlussuaq for the period 1852–1974 AD before the air temperature monitoring time at the site. This is done by using the linear correlation of the measured MAAT between Kangerlussuaq and the coastal sites in south–western Greenland for the period 1974–2017 AD shown in Figure A2-2(b). This temperature and the measured temperature for 1974–2011 AD are subsequently projected to the DH-GAP1 site by utilizing the linear correlation of the measurements for the period 2012–2017 AD between the DH-GAP01 site and Kangerlussuaq shown in Figure A2-2(a). For the most recent history 2012–2017 AD, the meteorological data form KAN_B is used directly.

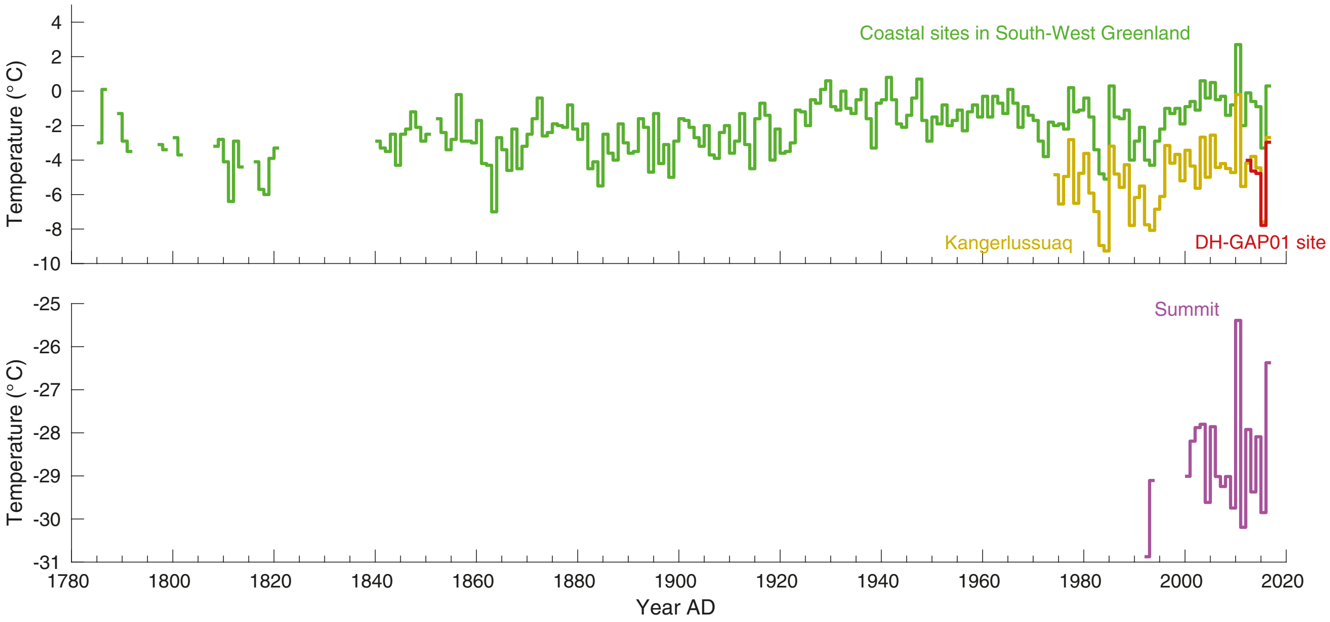

Figure A2-1. Continuous time series for MAAT at the DH-GAP01 site (2012–2017) (Van As et al. 2011), Kangerlussuaq (yellow) (1974–2017), coastal sites in south–western Greenland (1852–2017) (green) (Cappelen et al. 2017a, 2017b), and at Summit (2000–2017) (purple) (Steffen et al. 1996).

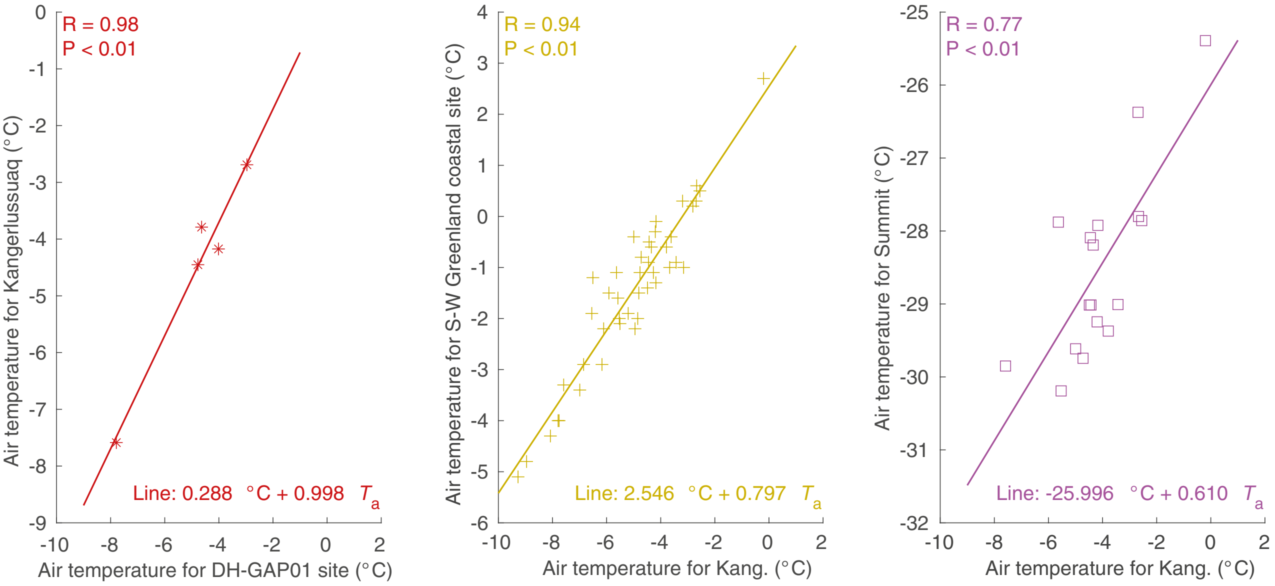

(a) **(b)** **(c)**

Figure A2-2. *Correlation of measured MAAT between the DH-GAP01 site and Kangerlussuaq (a), Kangerlussuaq and coastal sites in south–western Greenland (b) and Kangerlussuaq and Summit (c) (Van As et al. 2011, Cappelen et al. 2017a, 2017b, Steffen et al. 1996).*

For the time before year 1852 AD, two MAAT reconstructions as shown in Figure A2-3 have been used. The Holocene MAAT change for Greenland relative to 2000 AD (20-year averages) is based on the ice-core record of d^{18}O (Vinther et al. 2009), whereas the Holocene MAAT for Summit until 1993 AD (ten-year running mean) is based on the proxy ice-core record of argon and nitrogen isotopes (Kobashi et al. 2017). Discovering that despite of the long distance between Kangerlussuaq and Summit, there is a strong correlation in the measured MAAT between the two sites on an annual basis (Figure A2-2c), it was further found that there is a strong correlation between the reconstructed meteorological MAAT for the DH-GAP01 site and the air temperature data based on the ice-core records (Figure A2-4). Hence, with given linear correlations in Figure A2-4 and adopting the similar approach with the meteorological data completes the reconstruction of Holocene MAAT for the DH-GAP01 site.

The resulting MAAT given as temperature changes relative to the 30-year average for the period 1981–2010 AD are presented in Figure A2-5. MAAT reconstruction based on δ^{18}O varies moderately and has a clear decreasing trend until the Little Ice Age, whereas the reconstruction based on the argon and nitrogen isotopes fluctuates considerably and doesn't have any unique long-term trend.

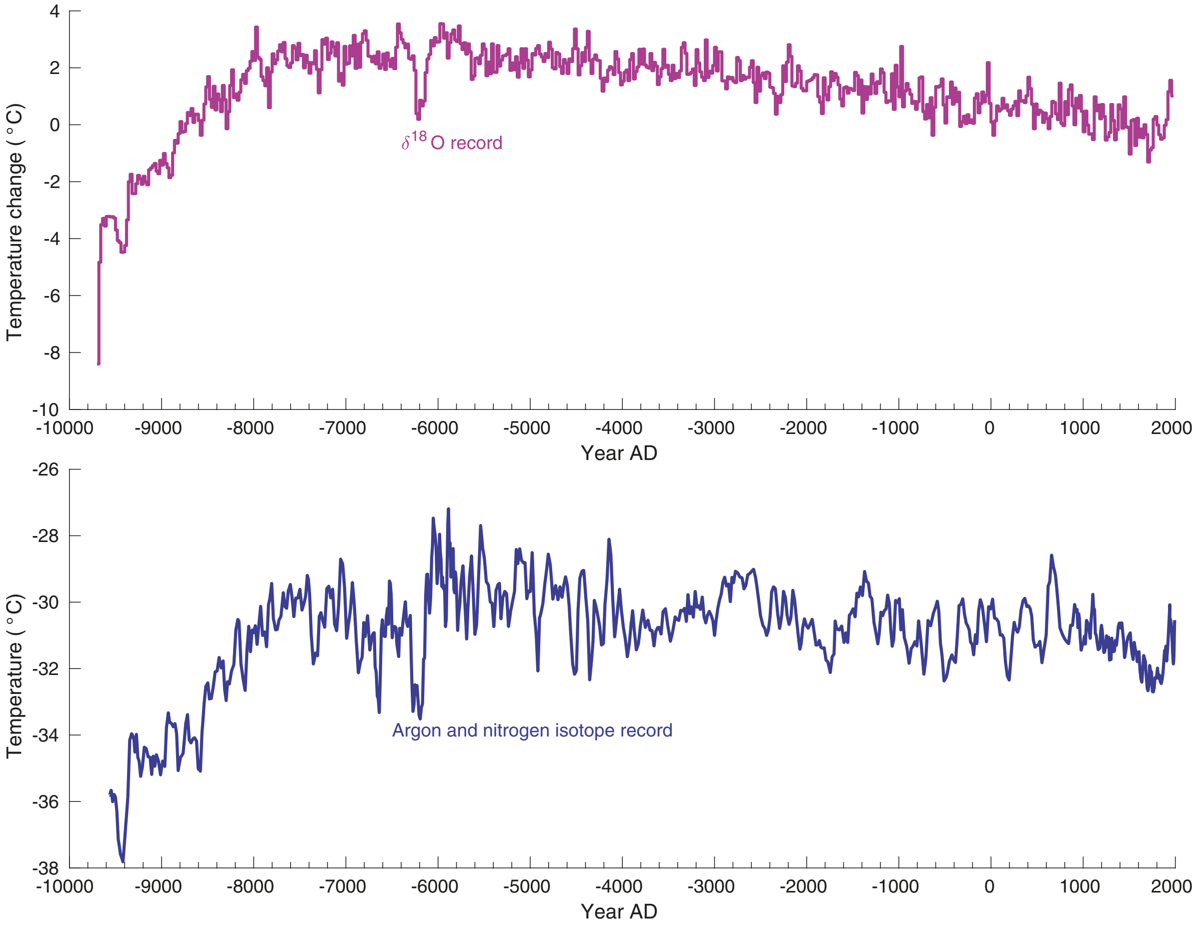

Figure A2-3. *Holocene MAAT change relative to 2000 AD based on the proxy ice-core records of d^{18}O (Vinther et al. 2009) (top) and Holocene MAAT for Summit based on the proxy ice-core record of argon and nitrogen isotopes (Kobashi et al. 2017) (bottom).*

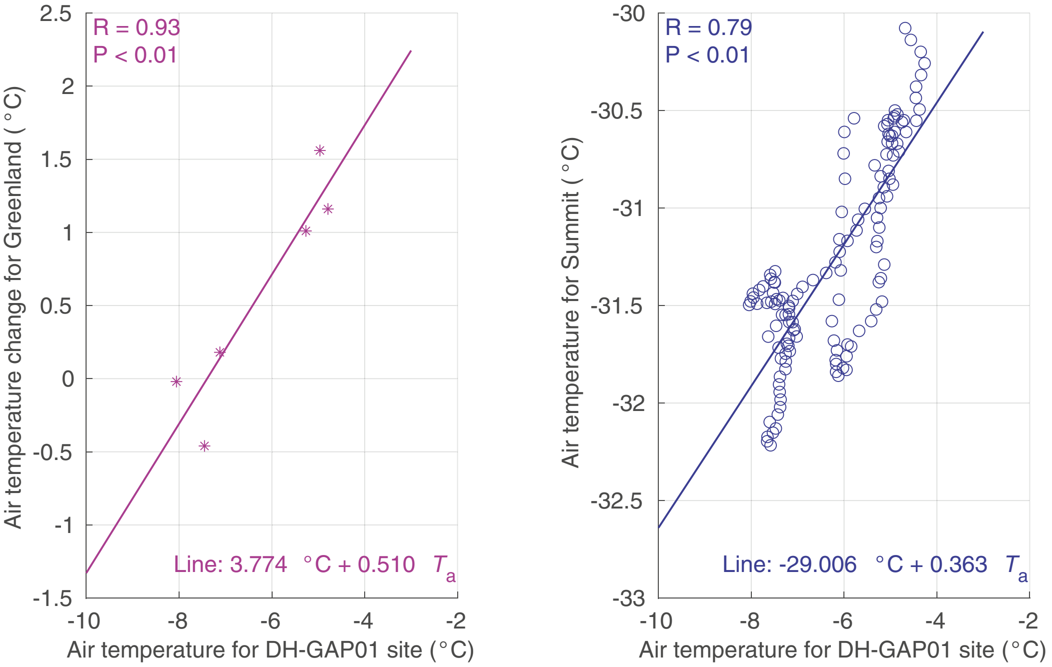

(a) **(b)**

Figure A2-4. *Correlation of MAAT between the meteorological data and the proxy ice-core records of d^{18}O (Vinther et al. 2009) (a) and argon and nitrogen isotopes (Kobashi et al. 2017) (b).*

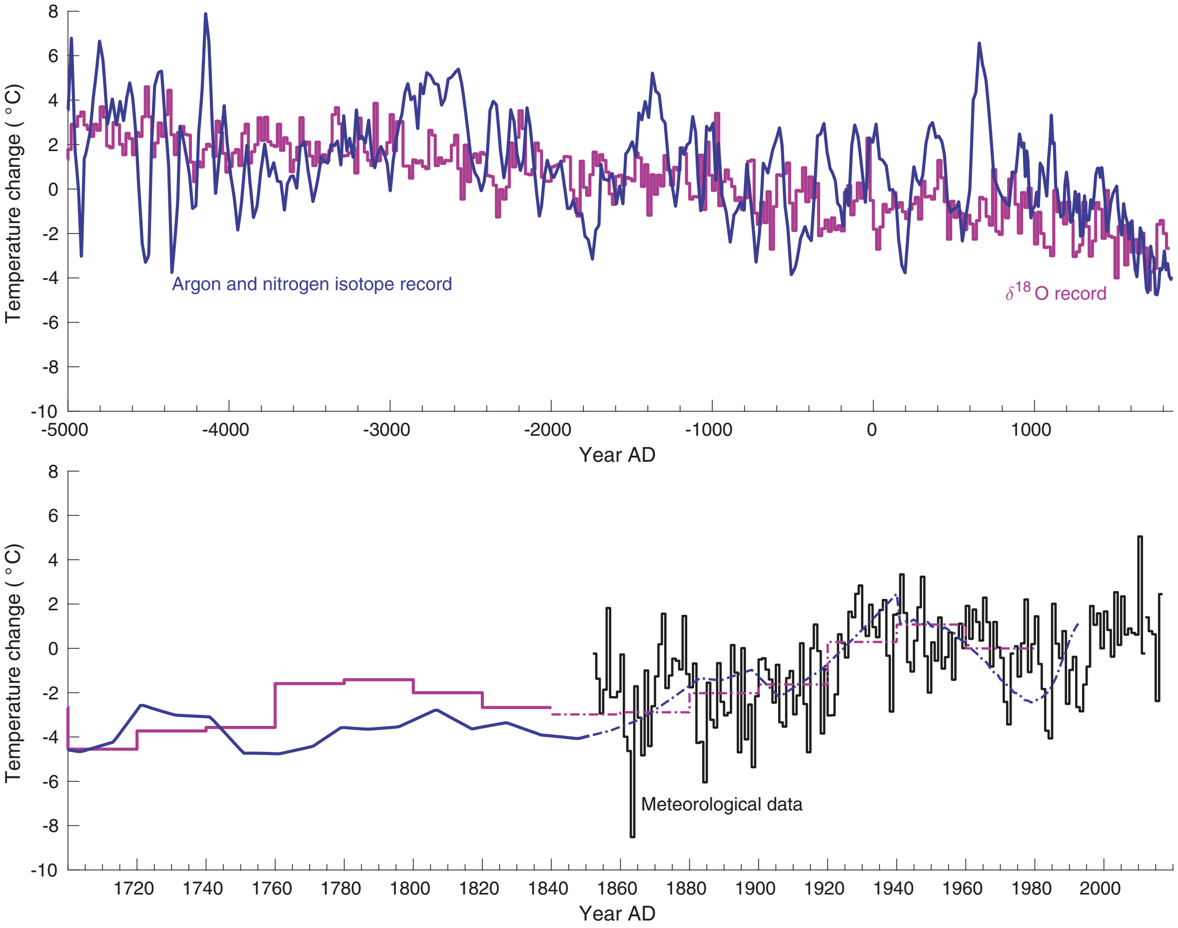

Figure A2-5. *Reconstructed proglacial Holocene MAAT change relative to the 30-year average for 1981–2010 for the DH-GAP01 site based on the meteorological data and the proxy ice-core records (Vinther et al. 2009, Kobashi et al. 2017).*

A2.2 Proglacial surface conditions

For modelling the surface conditions of the proglacial area, the important input data set are the location and extent of water bodies and the topographic wetness index.

A2.2.1 Location and extent of water bodies GAP (soil map)

The location and extent of water bodies in the model domain were extracted from the soil map, see Section A3.3 and Figure A3-9 (Petrone 2018).

A2.2.2 Topographic Wetness Index (TWI) GAP model

Ground surface humidity conditions are determined through the Topographical Wetness Index (TWI). This dimensionless quantity is commonly used to quantify topographic control on hydrological processes. The TWI calculations for the model domain were carried out in ArcGIS, where slope, flow direction and flow accumulation were calculated from the digital elevation model (DEM) of the area. Schwanghart and Kuhn (2010) describe the multi-direction water flow algorithm used in the TWI calculations. The TWI calculations used an altimeter-registered digital elevation model (ASTER DEM) posted at 30 m (Howat et al. 2014, 2015).

Two TWI models were produced where one model includes the elevation of the ice-sheet surface in the calculation, which results in that all precipitation that falls on the ice-sheet runs off supraglacially (Figure A2-6). This is however not a realistic case since water can percolate through the ice via fractures and moulins.

The other TWI model excludes the ice-sheet from the calculation (Figure A2-7), which allows an estimate of TWI for a situation when the ice-sheet has retreated.

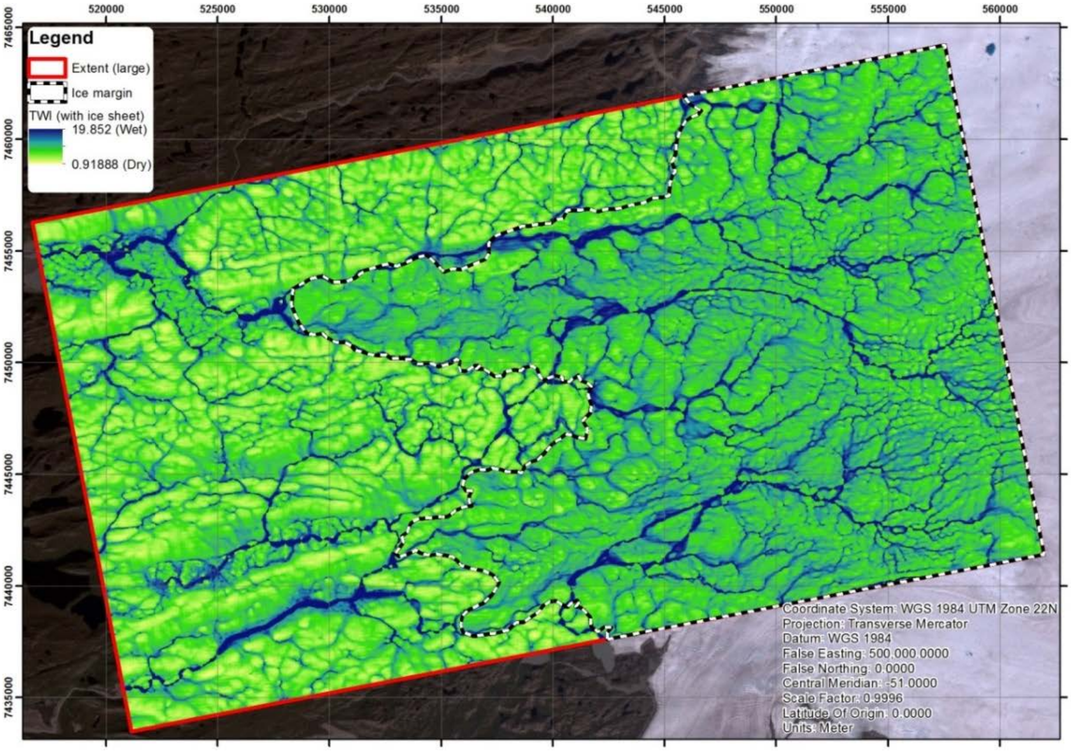

***Figure A2-6.** Topographic Wetness Index (TWI) for the model domain with ice-sheet conditions.*

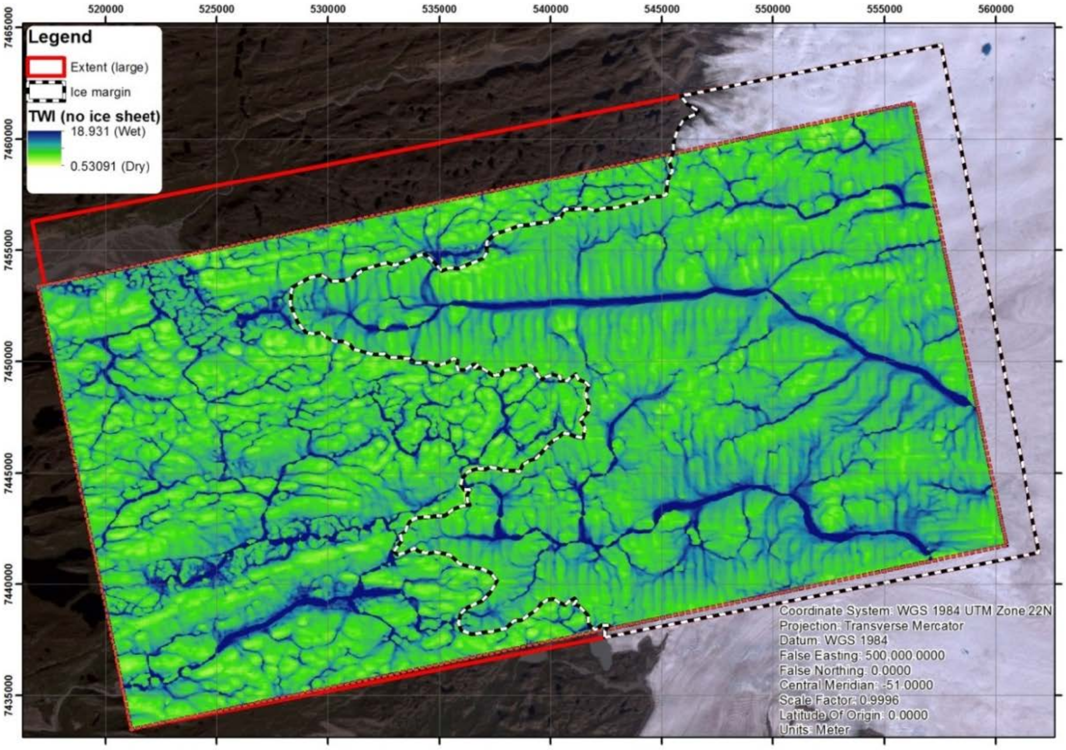

***Figure A2-7.** Topographic Wetness Index (TWI) for the model domain without ice-sheet conditions.*

A2.3 Present-day lapse rate

The present-day lapse rate (vertical air temperature gradient) at the GAP site is approximated by using the 2 m air temperature data from the Kangerlussuaq and KAN_B (DH-GAP01 site) weather stations (Cappelen et al. 2017b, Van As et al. 2011), and 1.6 m air temperature data from the soil temperature monitoring sites at the DH-GAP01 and DH-GAP03 drill sites (Figure A2-8). Using the MAAT from Kangerlussuaq at the elevation of 50 m and from KAN_B at the elevation of 380 m (Figure A2-1) gives a mean lapse rate of −0.9 °C km^{-1}. The monthly mean air temperature time series for the soil temperature monitoring sites (Figure A2-8) covers periods from September 2010 to April 2017 (DH-GAP01 site) and from September 2011 to July 2016 (DH-GAP03 site). Since values for August and September 2014 are missing from the DH-GAP03 site time series, the mean values of −5.4 °C for the DH-GAP01 site and −5.2 °C for the DH-GAP01 site for the years 2012, 2013 and 2015 are used for the lapse rate. Hence, using elevations of 374 m (DH-GAP01) and 484 m (DH-GAP03) yields a lapse rate of −1.5 °C km^{-1} between the sites.

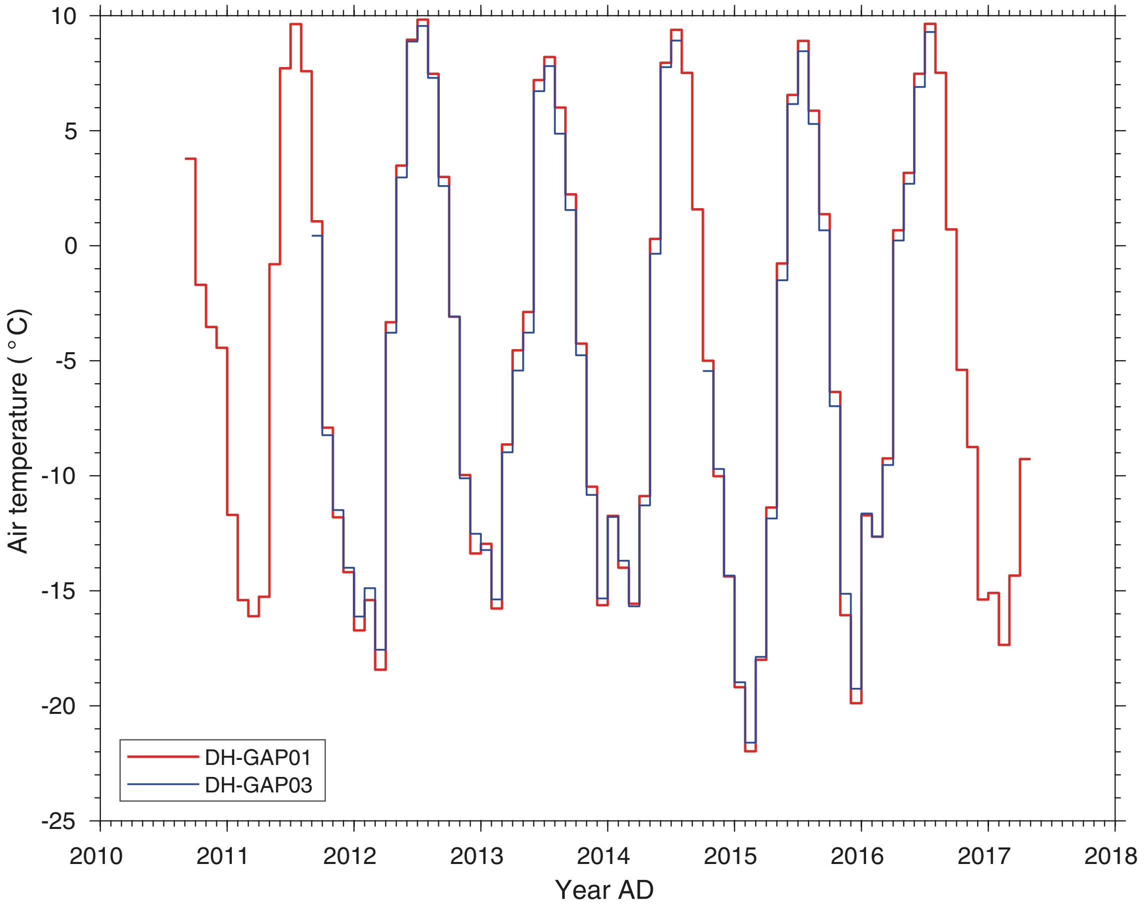

__Figure A2-8.__ Monthly air temperature for the soil temperature monitoring sites at the DH-GAP01 site (red) (September 2010 – April 2017) and DH-GAP03 site (blue) (September 2011 – July 2016). Monthly values for August and September 2014 are missing from the DH-GAP03 time series.

Appendix 3

Subsurface properties and conditions

The data on subsurface conditions and properties for the permafrost simulations consists of surface topography, material properties of bedrock and properties of soil cover. The bedrock data includes bulk density, porosity, thermal conductivity, specific heat capacity and radiogenic heat production and bedrock temperature as well. The soil data consists of soil depth and type. Soil properties and hydraulic conductivity of bedrock are based on the data from the Forsmark site (Hartikainen et Al. 2010).

A3.1 Geometry and topography

The surface topography included in the permafrost simulations is based on a combined resolution digital elevation model (DEM) for the area, utilising the ArcticDEM release 6 mosaic (tiles 15_38 2_2 and 16_38 2_1) (http://data.pgc.umn.edu/elev/dem/setsm/ArcticDEM/) and the GIMP DEM (Howat et al. 2014, 2015) of the area. The GIMP DEM covered areas has a resolution of 30 m and the ArcticDEM covered areas has a resolution of 5 m.

A3.2 Bedrock

A3.2.1 Petrophysical properties

Variation in rock type and rock physical properties have impact on processes studied with thermal modelling such as the growth of permafrost and the development of active layer. The essential parameters required in thermal modelling can be readily measured from rock samples. Measurement of petrophysical properties is best made from fresh, non-weathered rock samples and in sufficient amount to achieve statistical significance over the natural variability within the sample set. Evenly distributed rock samples were retrieved from the cores belonging to DH-GAP03 and DH-GAP04, with the aim to cover the main rock types distinguished by their mineralogical and textural characteristics. Care was taken that the sample was representative of the specific rock unit and did not include fractures or other anomalous features. A total of 18 10 cm long samples were collected from the 39 mm wide DH-GAP03 core with a sample distance of approximately 20 m. From the 50.5 mm wide DH-GAP04 core a total of 71 12–15 cm long samples were collected. Petrophysical determinations were conducted in the Petrophysical Laboratory of the Geological Survey of Finland in Espoo. From all samples the following determinations were done: density (kg m^{-3}), matrix porosity (%) and thermal conductivity (W m^{-1} K^{-1}). In addition to these parameters specific heat capacity (J kg^{-1} K^{-1}) and radiogenic heat production (W m^{-3}) for U, Th and K, respectively were obtained from the samples from DH-GAP04, to support thermal modelling.

A3.2.2 Bulk density (measured)

Densities were measured as the mass per unit volume, expressed in kilograms per cubic meters. The measurements were carried out by weighing the samples in air and water and calculating the dry bulk density (Archimedes' principle). The accuracy of the scale is 0.01 g and the repeatability for weighing of average-size (200 cm^3) specimens is better than 0.01 %.

A3.2.3 Porosity (total) (measured)

Porosities were determined by water saturation method. Water-saturated (seven days at room temperature and pressure) samples are weighed before and after drying (three days at 105 ºC) in oven. The accuracy of the scale used for porosity measurements is 0.01 g.

A3.2.4 Thermal conductivity (measured)

Thermal conductivity was measured with the steady-state divided bar method using an apparatus built at the Geological Survey of Finland. Disks with 7 mm thickness were prepared from the core samples. Thermal conductivity was measured after keeping the samples at least two days in a water bath at room temperature and pressure. Inaccuracies of thermal conductivity values are considered to be smaller than 5 %.

A3.2.5 Specific heat capacity (measured)

Specific heat capacity was measured on the samples from DH-GAP04 using a Phywe calorimeter added by thermometer functioning with AD590 sensor. The measurements were done from the same 7 mm disks as the thermal conductivity measurements. A calorimetric method was used. The sample is heated to a known temperature, then placed into a calorimeter containing a weighed amount of water, and the final equilibrium temperature of the calorimeter-water-sample system is measured. Specific heat is calculated from the initial and final temperatures of the sample and calorimeter, the heat capacity of the calorimeter, and the masses of water and sample. The sample is heated in boiling water, the temperature of which is measured with a Hg-thermometer. The temperature of a sample in the hot bath is about 98.5 °C. Temperatures in the calorimeter are measured electronically with a semiconductive temperature sensor (AD 590) having a nominal resolution of 0.002 K. The specific heat capacity is determined with an inaccuracy of less than 5 %, and a repeatability of 3–5 %. The GTK raw data on specific heat capacity was corrected to room temperature conditions by 7.5 % reduction.

A3.2.6 Radiogenic heat production GAP (measured)

Radiogenic heat production measurements (K, U, Th) were performed on 30 samples from DH-GAP04 using a multichannel analyzer EG&G Ortec ACE™-2K gamma spectrometer equipped with a four-inch NaI/TI detector. Measurements were done on solid pieces cut from the core. The samples were first kept in plastic for one week in order to prevent the escape of radon. Measuring time for samples and standards was 30 minutes and for background 60 minutes. Standard samples were measured 2–3 times, and the results show that the measured values are in good agreement with the expected values. Energy levels (MeV) of gamma spectrum for measured emitters are for K 1.36–1.56, for U 1.66–1.86 and for Th 2.41–2.81. 'Total' gives the net signal of radioelements (ur, unit of radioelement concentration). Radiogenic heat production was calculated from the contents of K, U and Th according to equation: $H = 10^{-5}\rho(9.52c_{U} + 2.56c_{Th} + 3.48c_{K})$, in µW m^{-3} (Balling 1995, Beardsmore and Cull 2001) where ρ is the density of sample.

A3.2.7 Measured GAP bedrock temperature

Bedrock temperature measurements were performed in the DH-GAP04 borehole from 2011 and onwards (Claesson Liljedahl et al. 2016). The mean annual temperature for the year September 2016 – August 2017 is shown in Figure A3-1. The 100–550 metres depth interval of the smoothed curve based on a 10-metre moving average is used for the permafrost model evaluation. The inversion near the top of the borehole is due to the warming of climate from the previous year.

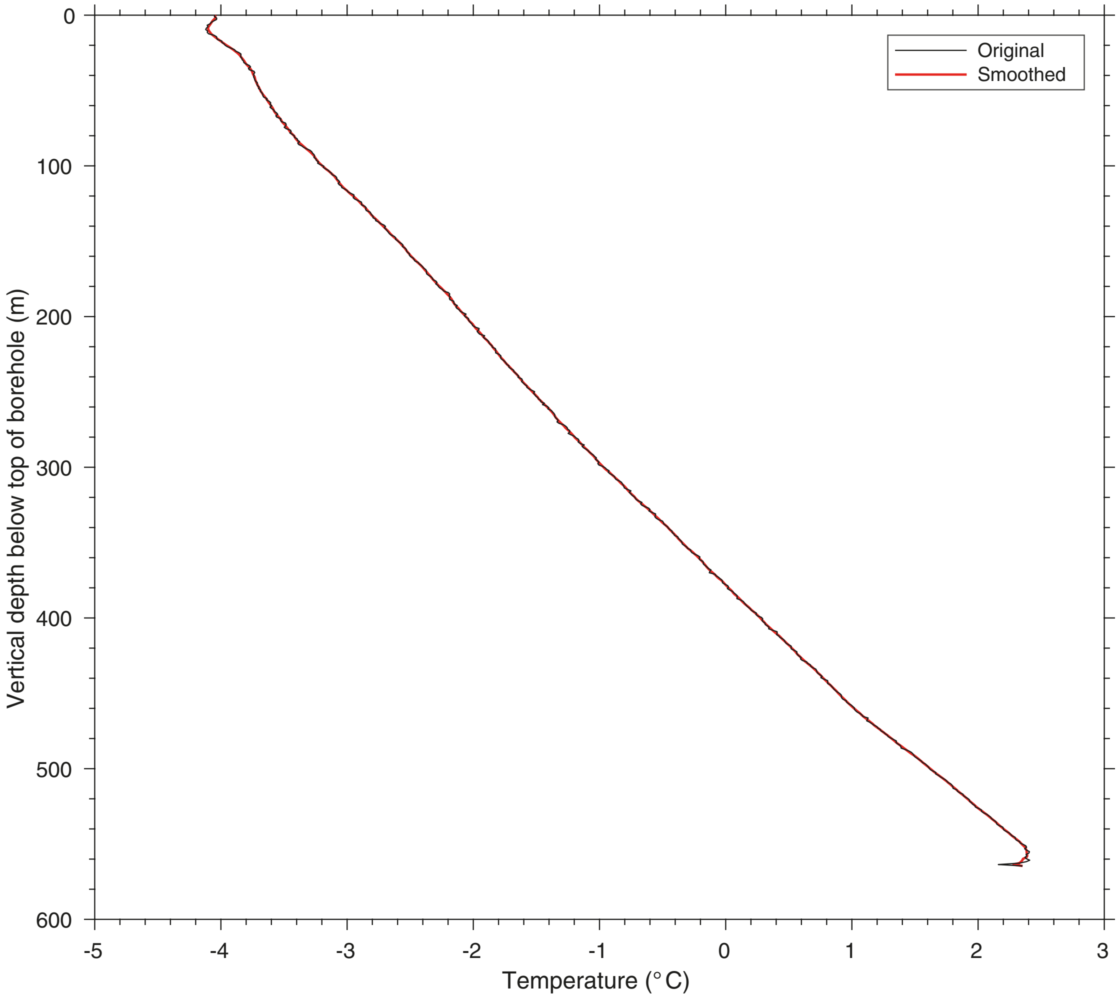

***Figure A3-1.** Measured mean annual bedrock temperature for September 2016 – August 2017 for borehole DH-GAP04. The smoothed curve is a 10 m moving average of the original curve. The inversion near the top of the borehole is due to recent warming of the climate, and the inversion near the bottom of the borehole is due to termination effects of the optical fibre, used to obtain the borehole temperature.*

A3.2.8 Geothermal heat flow (model/calculated)

By combining information from DH-GAP04 borehole temperature profiling from September 2016 – August 2017 with petrophysical data the steady-state heat flow density (HFD) was calculated for DH-GAP04. Moving averages of the temperature gradient and thermal conductivity are used. The average HFD calculated between 100–526 m, is 27.6 ± 1.8 mWm^{-2} (Figure A3-2). The change in the HFD values at 250–300 metres depth is assumed to be due to effects of the ice-sheet and topography together with the tilting of the borehole. The HFD values from DH-GAP04 are corrected for climatic effects, i.e. long term palaeoclimatic variations, in the next section.

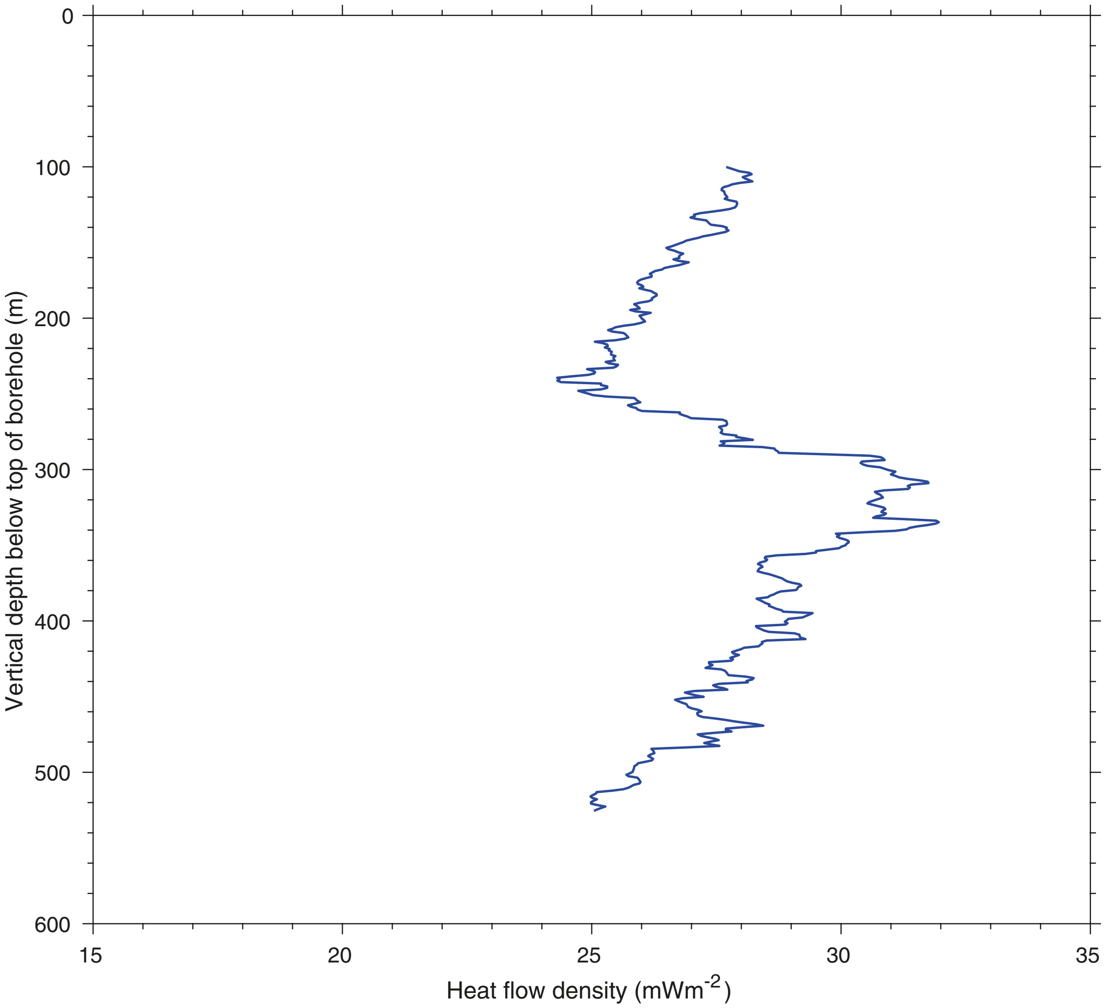

Figure A3-2. *Calculated HFD for borehole DH-GAP04. HFD calculated from 50 m windows moving averages of thermal conductivity and temperature gradient of the borehole temperature profile from September 2016 – August 2017.*

A3.2.9 Palaeoclimatic correction of geothermal heat flow

HFD is not constant with depth. Vertical variation depends on crustal radiogenic heat production, heat flow from the mantle, convective heat transfer due to groundwater flow, heterogeneity of the material, surface topography, uplift, subsidence, erosion, sedimentation, and palaeoclimate, i.e. variations in the past MAGST (cf Benfield 1939, Birch 1948, Kukkonen and Jõeleht 2003).

The measured vertical component of HFD at the DH-GAP04 site is corrected for the influence of the lower MAGST during glacial phases (manifested by the warming when entering the post-glacial ice-free period) to obtain a so-called palaeoclimatically corrected HFD. In the absence of HFD data from several km depths, undisturbed by long-term climate changes at the ground surface, a palaeoclimatically corrected HFD is in the present study needed for the heat flow boundary condition at the lower boundary of the model domain at the 10 km depth. The palaeoclimate correction is done by exploiting the solution of the unidimensional linear heat conduction problem in the semi-infinite homogeneous solid for given constant surface temperature and initial temperature of 0 °C (Carslaw and Jaeger 1959). With given step-wise changes of the past MAGST the resulting average palaeoclimatic correction of HFD for the depth interval $z_1 \leq z \leq z_2$ at time t can be computed by the equation:

$$\Delta q(t) = \frac{k}{z_2 - z_1} \sum_{i=1}^{n} \Delta T_{\mathrm{s}.i} \left[\operatorname{erf} \frac{z_2}{2\sqrt{\kappa(t - t_i)}} - \operatorname{erf} \frac{z_1}{2\sqrt{\kappa(t - t_i)}} \right]$$

where $\Delta T_{\mathrm{s}.i}$ is the MAGST change at time $t_i < t$, k is the thermal conductivity and κ the thermal diffusivity defined by $\kappa = \frac{k}{C}$, where C is the volumetric heat capacity.

For the glaciated period of the last glacial cycle (104–7 ka BP), the past MAGST consists of the basal ice temperature history of the reference and sensitivity SICOPOLIS simulations described in Appendix A1, whereas for the last 7 ka (approximately Middle and Late Holocene), 16 temperature histories have been reconstructed by the permafrost surface models. The MAGST-development between 7 and 0 ka BP are computed based on the two MAAT reconstructions (V, K, see Section A2.1), two precipitation conditions (L, H, see Section 3.3), two timings of the last readvance of the GrIS (500, 800, see Section 3.3) and for both models representing different TOs (Model A and B, see Section 3.1). In order to account for the effects of topography and lateral variations of the surface conditions, MAGST is averaged over a 20-km wide region extending 10 km in both directions from the borehole. The resulting MAGST anomalies with respected to the mean glacial cycle MAGST of each individual MAGST case are shown in Figure A3-3 (zero TO, Model A) and in Figure A3-4 (nonzero TO, Model B).

Using an average thermal conductivity of $k = 2.3$ $\mathrm{Wm^{-1}K^{-1}}$, a volumetric heat capacity of $C = 1.98$ $\mathrm{MJm^{-3}K^{-1}}$ and the step-wise changes of MAGST shown in Figure A3-5 (zero TO, Model A) and Figure A3-6 (nonzero TO, Model B), Equation (A3-1) yields an average palaeoclimatic correction of HFD for the depth interval $300 \text{ m} \leq z \leq 500 \text{ m}$ that amounts between ~6 and ~13 mW $\mathrm{m^{-2}}$ (Figure A3-7). In addition, the higher air temperature (K) has a positive influence of 1.3 ± 0.3 mW $\mathrm{m^{-2}}$ on the palaeoclimatic correction in comparison to the lower one (V). In the same way, the higher precipitation (H) against the lower one (L) increases the palaeoclimatic correction by 0.5 ± 0.2 mW $\mathrm{m^{-2}}$, whereas the higher basal temperature (Gbh) compared to the lower one (G) decreases the palaeoclimatic correction by 3.24 mW $\mathrm{m^{-2}}$. In addition, the earlier readvance of the GrIS, i.e. the last readvance timing of 800 versus 500 years BP, increases the palaeoclimatic correction by 1.7 ± 0.3 mW $\mathrm{m^{-2}}$. The effect of TO on the palaeoclimatic correction is decreasing, i.e. TO in Model B reduces the palaeoclimatic correction by 0.5 ± 0.2 mW $\mathrm{m^{-2}}$. in comparison to zero TO Model A.

The mean and standard deviation of the 32 cases are 9.8 and 2.0 mW $\mathrm{m^{-2}}$, which yield the palaeoclimatic correction of 9.8 ± 2.0 mW $\mathrm{m^{-2}}$ that is used to deduct the undisturbed thermal boundary condition at the bottom of the model domain for all model simulations in this report. The result is further illustrated by using a cumulative sum in Figure A3-8.

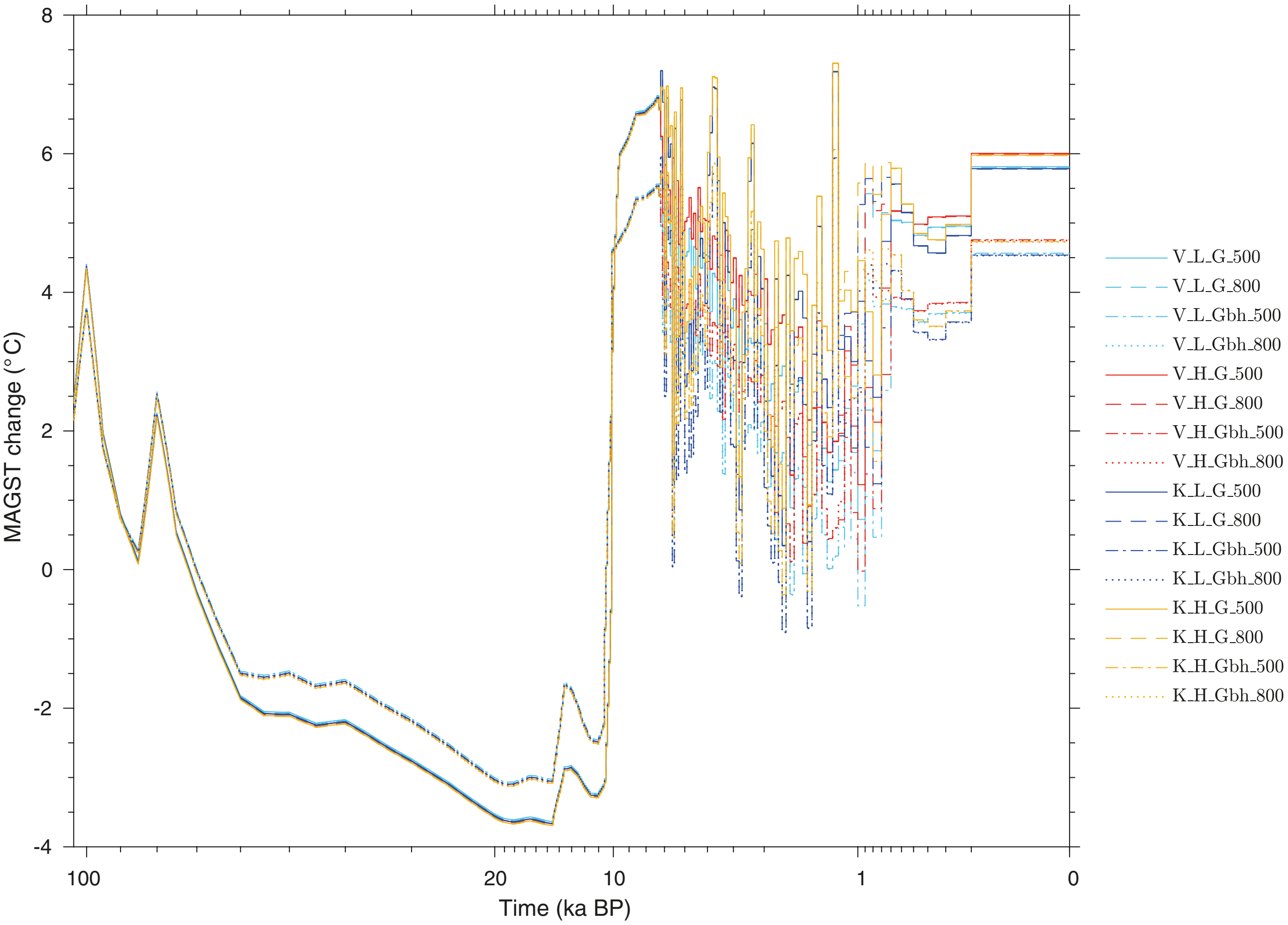

Figure A3-3. *MAGST change from the mean glacial cycle value for the DH-GAP04 site based on the MAAT reconstructions V and K, precipitation conditions L and H, basal ice temperatures G and Gbh and timing cases of the last readvance of the GrIS 500 and 800 and considering zero TO (Model A).*

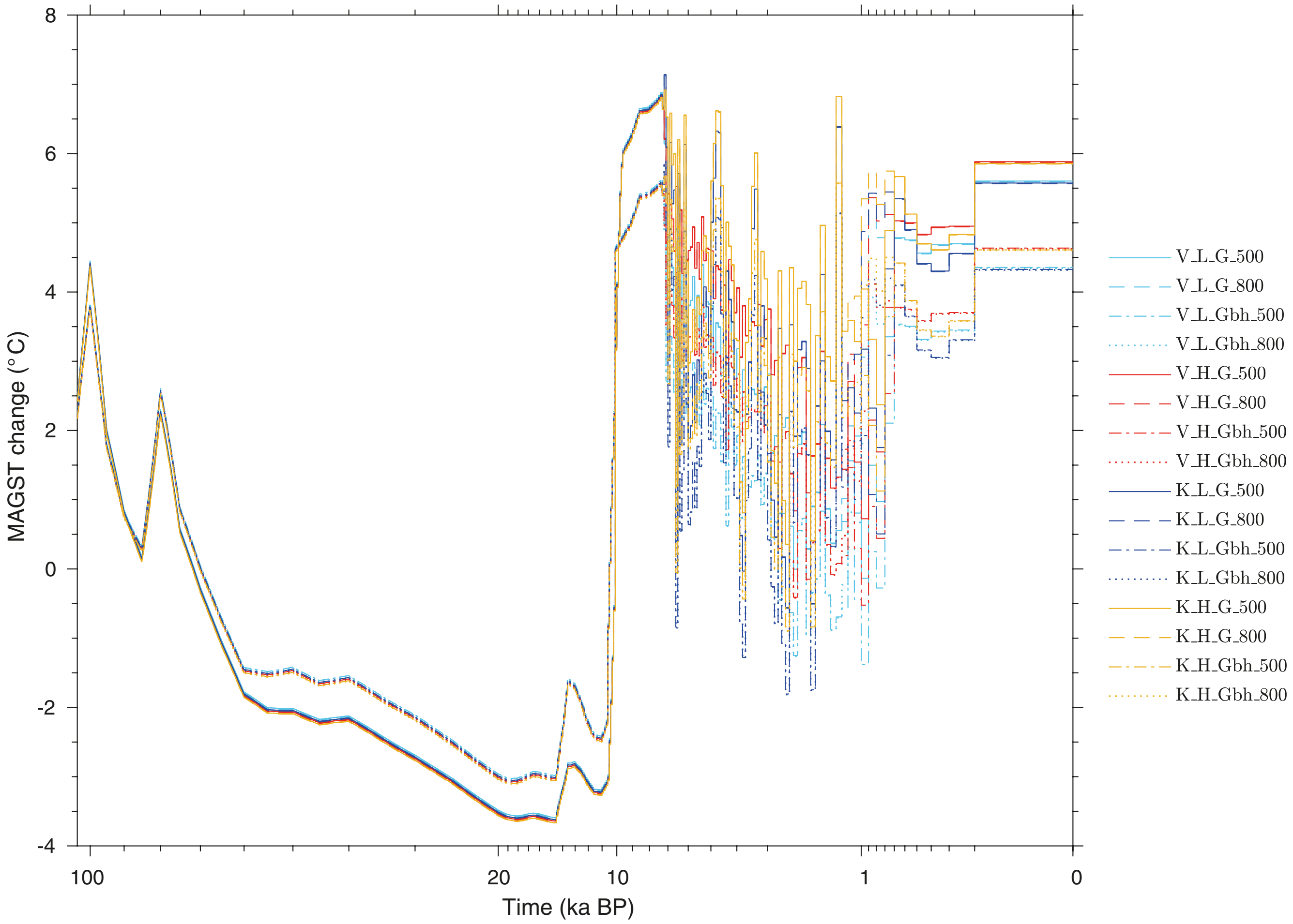

Figure A3-4. *Same as Figure A3-3 but for nonzero TO (Model B).*

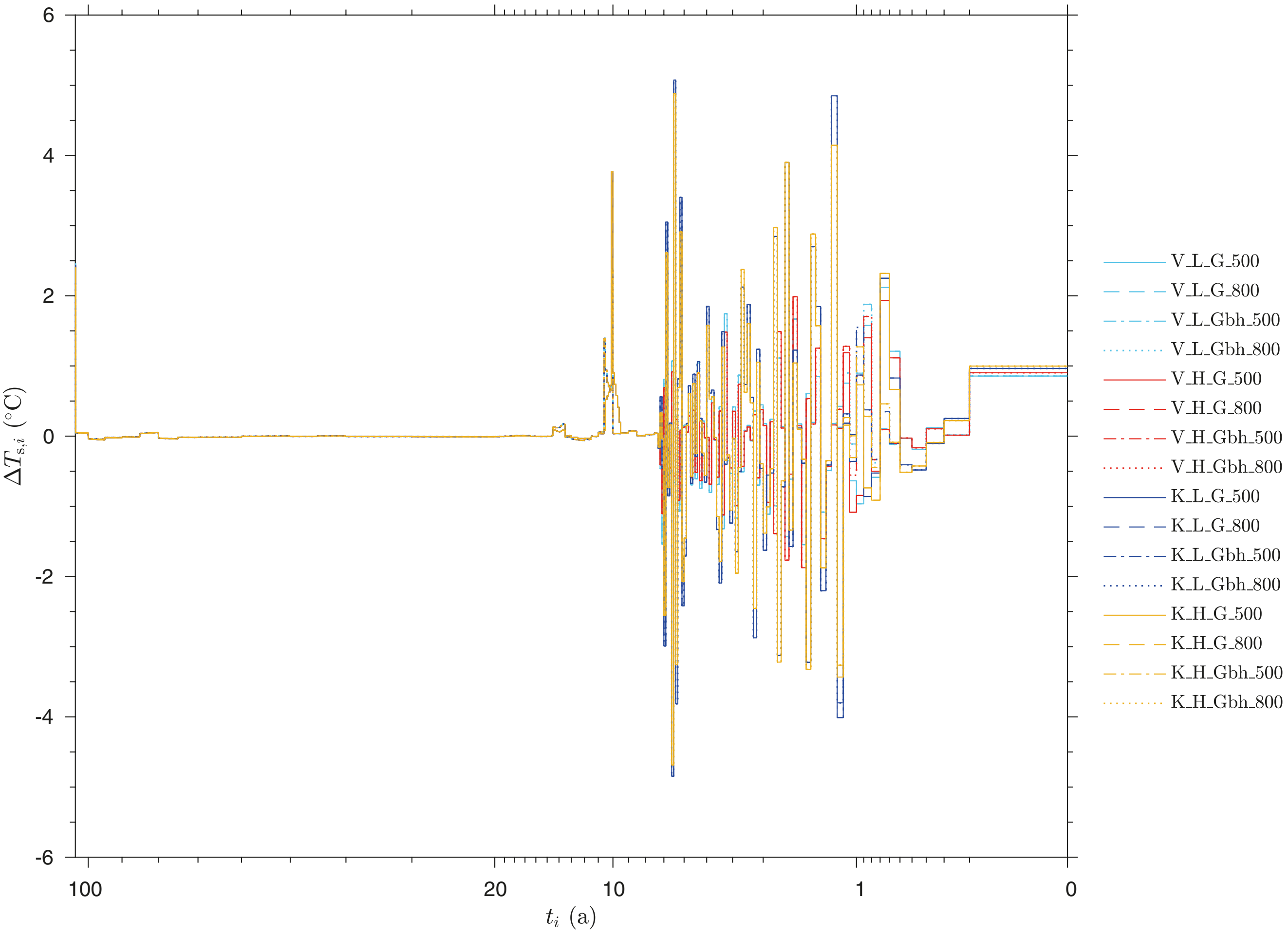

Figure A3-5. *Step-wise change of MAGST based on the MAAT reconstructions V and K, precipitation conditions L and H, basal ice temperatures G and Gbh and timing cases of the last readvance of the GrIS 500 and 800 and considering zero TO (Model A), nonzero TO (Model B).*

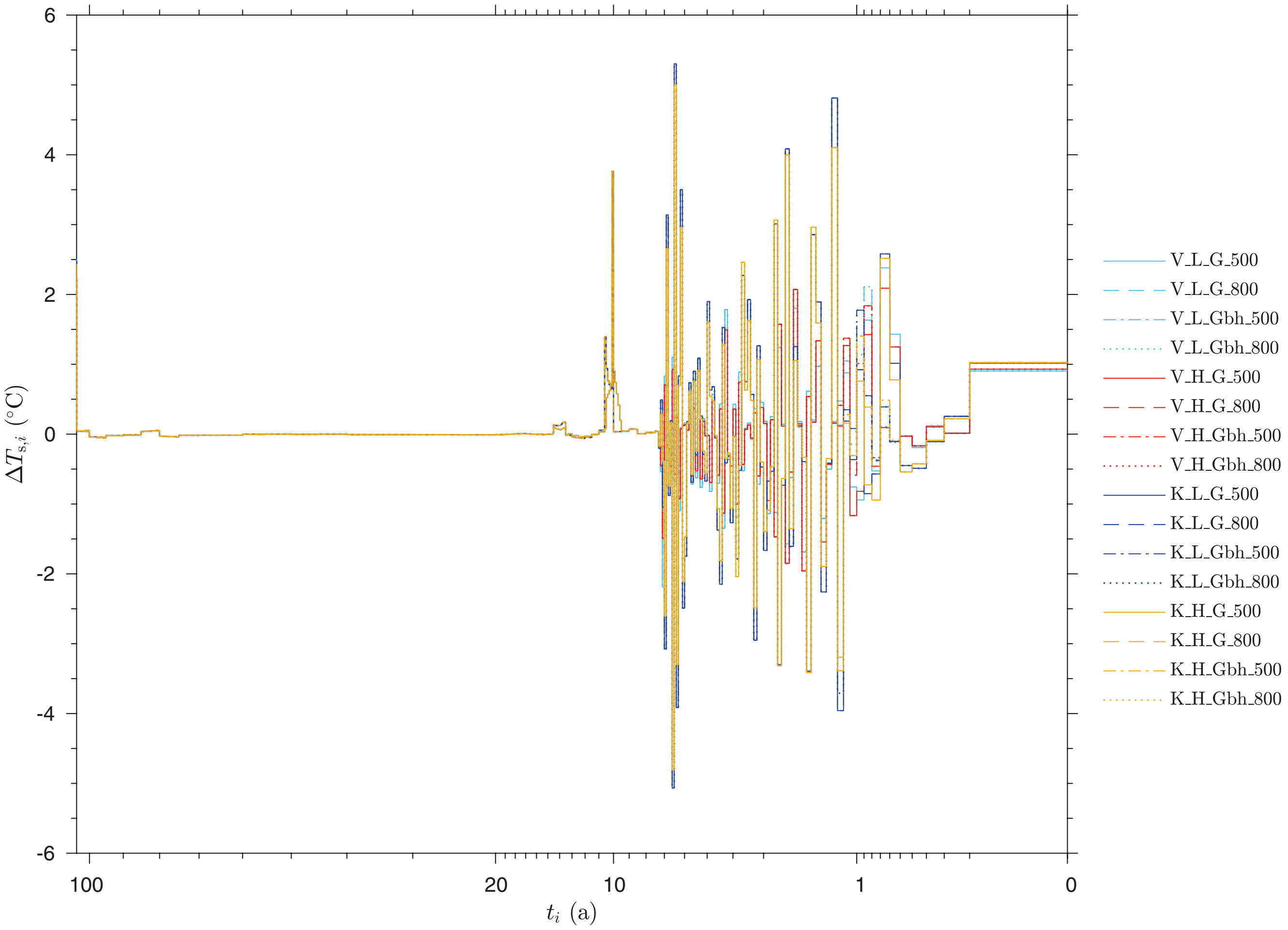

Figure A3-6. *Same as Figure A3-5 but for nonzero TO (ΔT < 0 °C Model B).*

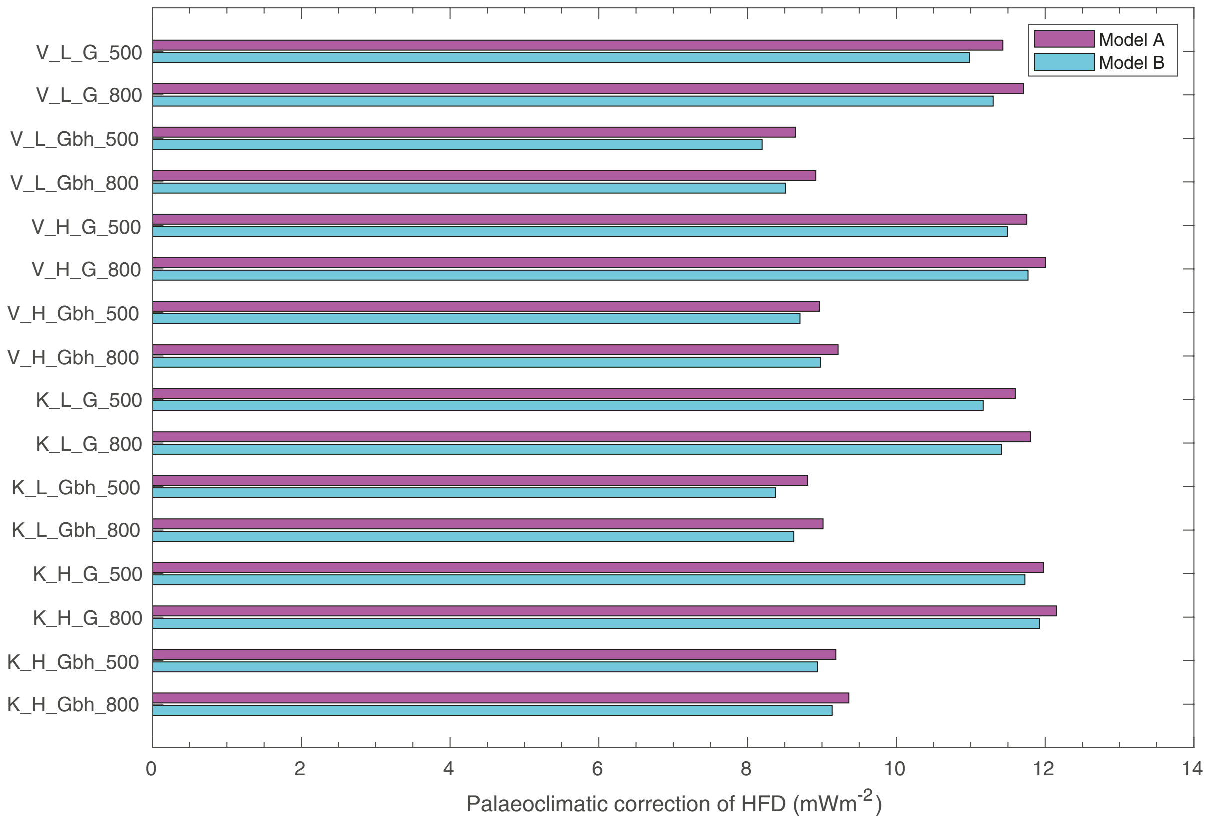

Figure A3-7. *Modelled perturbation of HFD for the 16 test cases consisting of MAAT cases V and K, precipitation cases L and H, basal ice temperatures G and Gbh and two last ice-sheet readvance timing cases 500 and 800 and using zero (Model A) and nonzero (Model B) TO.*

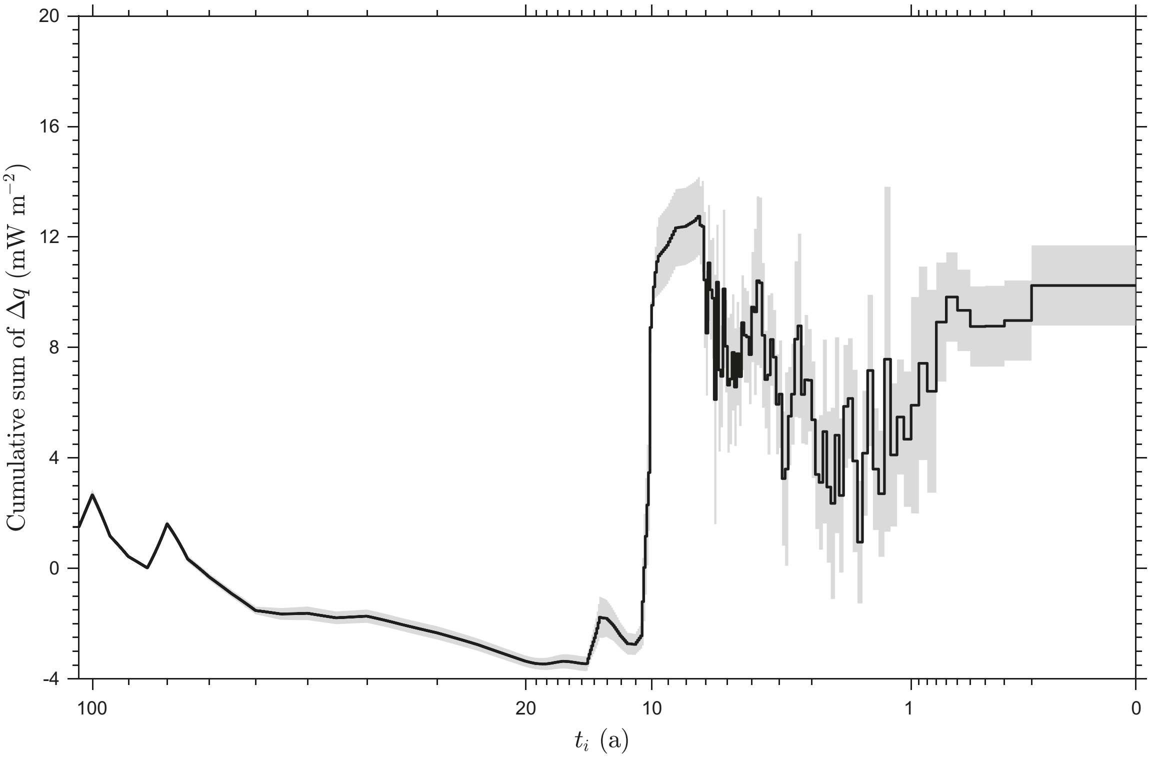

Figure A3-8. *Cumulative sum of the mean value (black line) and the standard deviation (grey area) of palaeoclimatic correction of HFD for the DH-GAP04 site.*

In order to evaluate the validity of this palaeoclimatic correction, the above equation is also applied to the Outokumpu Deep Drill Hole site (Kukkonen et al. 2011) that has been subject to independent estimates of the palaeoclimatic correction. Using the thermal conductivity and volumetric heat capacity (shown in Table A3-1) and MAGST histories of Kukkonen et al. (2011), the average palaeoclimatic correction for the depth interval of 100–1 000 metres is shown in Table A3-2. The results from the independent site agree well with the values from the DH-GAP04 site. In addition, the modelled palaeoclimatic correction for the DH-GAP04 site compares well with the average correction of 15 mWm^{-2} at the 500-m depth for the Fennoscandian Shield proposed by Kukkonen and Jõeleht (2003). Furthermore, the palaeoclimate correction is in line with the palaeoclimate correction of c 10 mWm^{-2} estimated for the Summit site in Greenland (Dahl-Jensen et al. 1998).

Table A3-1. Average thermal properties for the Outokumpu site (Kukkonen et al. 2011).

Thermal conductivity ($W\ m^{-1}\ K^{-1}$)	Heat capacity ($MJ\ m^{-3}\ K^{-1}$)	Comment
2.43	1.89	Average for the 300–500-m depth interval

Table A3-2. Modelled palaeoclimatic correction of HFD and the palaeoclimatically corrected HFD for the Outokumpu site.

Depth interval	Model		Reference value		Comment
	Palaeoclimatic correction	Palaeoclimatically corrected HFD	Palaeoclimatic correction	Palaeoclimatically corrected HFD	
100–1 000 m	9	40	10	42	Reference value concerns the 1-km depth interval

A3.3 Soil type and depth model

A soil cover map (Figure A3-9) and regolith depth model (Figure A3-10) covering the model domain used in the permafrost simulations was produced in 2018 (Petrone 2018). The regolith analysis combined results from analysis and processing of multispectral satellite images with data from several field visits and the general regional understanding of the periglacial landscape.

For the analysis data from the DigitalGlobe's WorldView-2 (WV2) satellite sensor was processed and used. Multispectral satellite images with a resolution of 2.0 m from WV2 included the spectral bands listed in Table A3-1.

Table A3-1. WorldView-2 multispectral specifications.

Band number	Band name	Spectral interval
1	Panchromatic	450–800 nm
2	Coastal	400–450 nm
3	Blue	450–510 nm
4	Yellow	585–625 nm
5	Red	630–690 nm
6	Red edge	705–745 nm
7	Near Infrared	1770–895 nm
8	Near Infrared	2860–1040 nm

As a basis of surface analysis different image data sets from DigitalGlobe were processed and orthorectified (geometrically corrected) using the ArcticDEM Realease 6 (tiles 15_38 2_2 and 16_38 2_1) (http://data.pgc.umn.edu/elev/dem/setsm/ArcticDEM/) and the GIMP DEM (Howat et al. 2014, 2015). Polar Stereographic or WGS 84 UTM Zone 22N was used as the coordinate system for all files used and produced.

Field visits to several sites were made in 2017 to obtain information on depths and to provide correlation points for the soil type/landscape type classification. Petrone (2018) presents a list of sites visited. Even though a few field sites were visited for field checking, the model domain covers a large area and therefore the uncertainty can be quite large in interpolated soil depths.

A3.3.1 Soil types

Several soil type classes were defined based on the spectral signatures and the regional understanding of the area (Table A3-2). A maximum likelihood classification was performed using Spatial Analyst in ArcMap 10.5.1. To remove most of the noise and to smooth out boundaries focal statistics and majority filters were applied.

The soil map is presented as a 2 × 2 m raster with 7 different classes (Table A3-2 and Figure A3-9). Each landscape class and percentage relative of the total surface area, excluding the ice-sheet, is presented in Table A3-3.

Table A3-2. Class division with associated regolith information.

Class number	Class name	Regolith information
2	Glacial meltwater	Glaciofluvial sediments
3	Lake	Gyttja and/or silt
4	Vegetated surface	Silt and/or silty peat
5	Barren	Thin till on bedrock
6	Sand deposits	Eolian sand
12	River sediments and proglacial sediments	Glaciofluvial sediments and proglacial till
13	Glacier	Thin till on bedrock

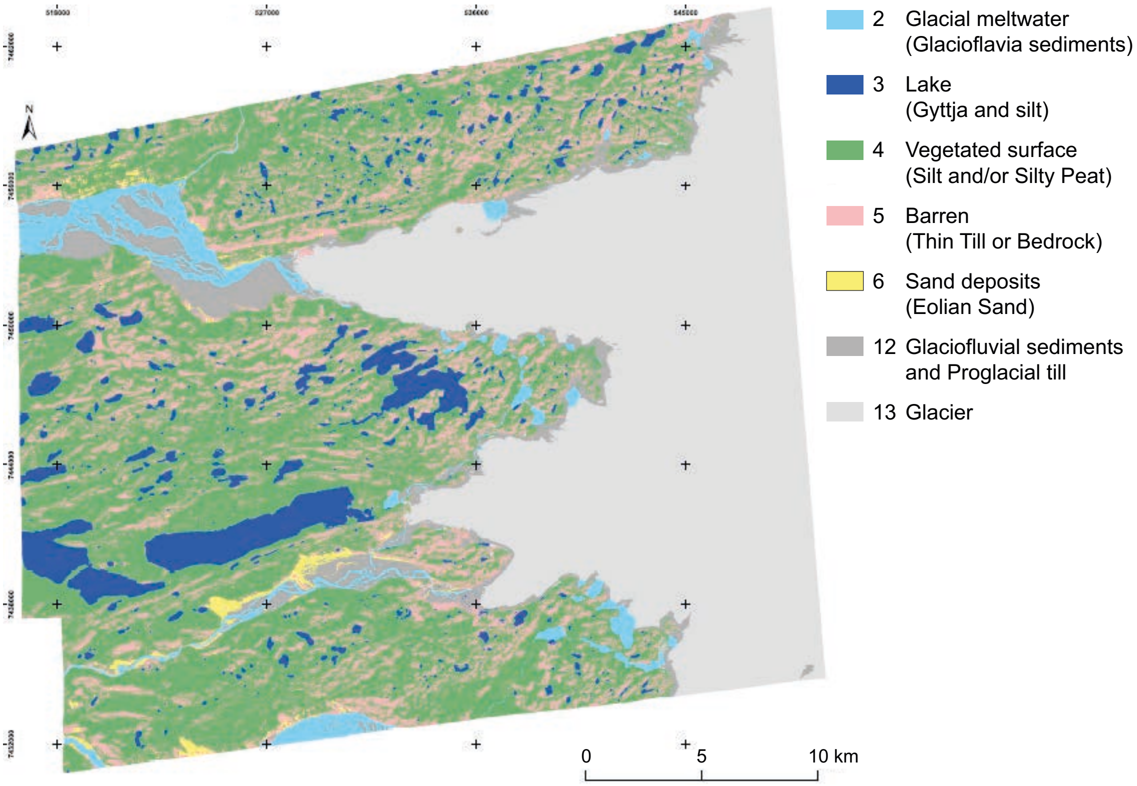

Figure A3-9. *Soil map covering the study area (Petrone 2018).*

Table A3-3. Each landscape class and percentage of total land area.

Class	Percentage of non-ice area
Glacial meltwater	5 %
Lake	8 %
Vegetated surface	58 %
Barren	20 %
Sand deposits	1 %
River sediments and proglacial sediments	8 %

A3.3.2 Average soil thickness (soil map)

The description of the average thickness of soil cover in the model domain area has been provided from Petrone 2018. The soil thickness is presented as a 100 × 100 m depth regolith depth model (Figure A3-10). To create more realistic regolith depth transition between classes a mean filter was applied, and thickness pixels were smoothed using the mean of the neighbouring pixels. Regolith depths were assigned based on field data and scientific references from the area (Storms et al. 2012, Petrone et al. 2016). Table A3-4 presents the landscape classes and regolith depth intervals applied.

As mentioned in Section 3.3.3, it should be noted that the soil thickness model shown in Figure A3-10 overestimates soil thicknesses in certain areas due to interpolation effects. Of specific interest, this is the case for the location of the DH-GAP04 borehole. At this site, soil thicknesses are considerably larger in the model (designated to the regolith depth interval 19–24 m of Table A3-4, see Figure A3-10) than in reality. The correct regolith thickness for this specific location should be 3 m or less. The error introduced by this soil thickness model overestimation have been studied by a dedicated permafrost model sensitivity simulation where regolith thicknesses were reduced by 90 % (Section 3.3.3, test case S10). The result shows that the locally overestimated regolith thickness in the soil model only has a minor influence on modelled bedrock temperatures. The 90 % reduction in regolith thickness only results in a 0.01 ± 0.03 °C decrease in the average bedrock temperature at the DH-GAP04 borehole location (Section 4.2.2).

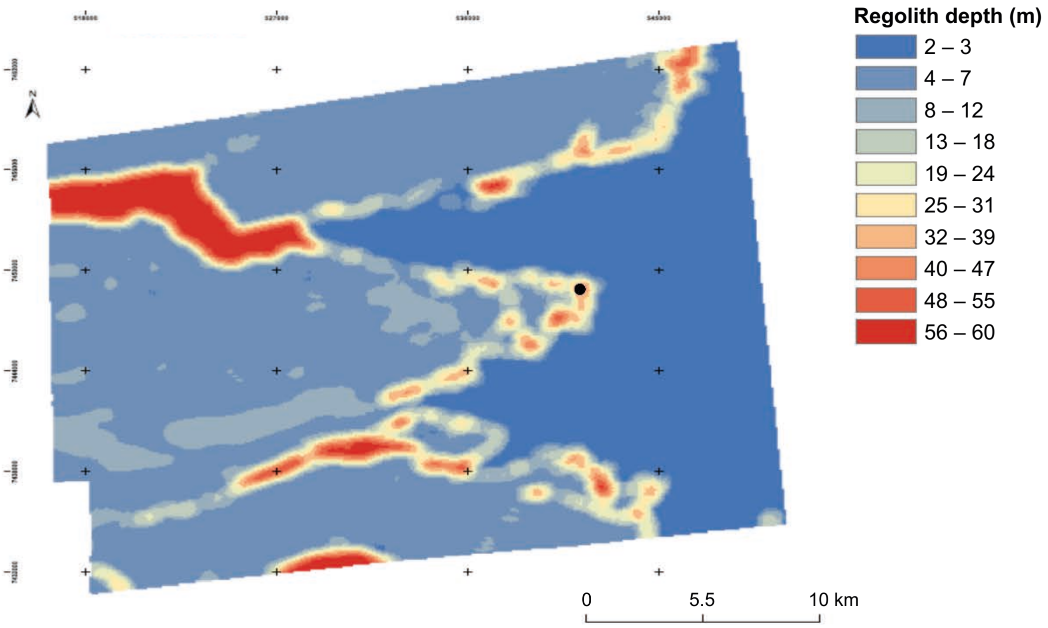

Figure A3-10. Regolith depth model (Petrone 2018). Note that some regolith depths in the model are known to be too large, e.g. around the DH-GAP04 borehole site (see the text). Black circle = DH-GAP04 borehole site.

Table A3-4. Regolith thickness intervals in meters. [1] Storms et al. 2012. [2] Petrone et al. 2016.

Class	Regolith thickness interval (m)
2 – Glaciofluvial sediments	20–60[1]
3 – Gyttja and/or silt	5–10
4 – Silty and/or silty peat	2–5[2]
5 – Thin till on bedrock	0–2
6 – Eolian sand	2–10
12 – Glaciofluvial sediments and proglacial till	20–60[1]
13 – Thin till on bedrock	0–2

A3.3.3 Soil properties

The data from the Forsmark site is used for the thermal and hydraulic properties of soil cover. The assigned properties are presented in Hartikainen et al. (2010).

Appendix 4

Supplementary results

A4.1 Geothermal heat flow

Figure A4-1 shows a 2D cross-sectional heat flow simulation for geothermal heat flow density along the model domain for the K_H_Gbh_500_Mean_S100 test case. First, at around 10 ka (3 kyr before deglaciation), the local basal thermal state of the ice-sheet changes from being cold-based (basal ice temperature ~−8 °C) to warm-based (basal ice temperature at the pressure melting point, ~−1 °C). This results in a very strong decrease in heat flow. At the DH-GAP04 drill site, the heat flow is reduced from 35 ± 3 to 12 ± 1 mW m^{-2} (~65 % decrease). Subsequently, at the time of deglaciation (around 7 ka), the ground surface cools by 2–6 °C, compared to the ice-covered warm-based period, as the area becomes subject to Middle Holocene air temperatures. This cooling lithospheric surface boundary condition increases heat flow to 25 ± 5 mW m^{-2}. At this site, the glacial transitions therefore result in complex changes in heat flow, with values ranging from 11 to 38 mW m^{-2} over the past 100 ka.

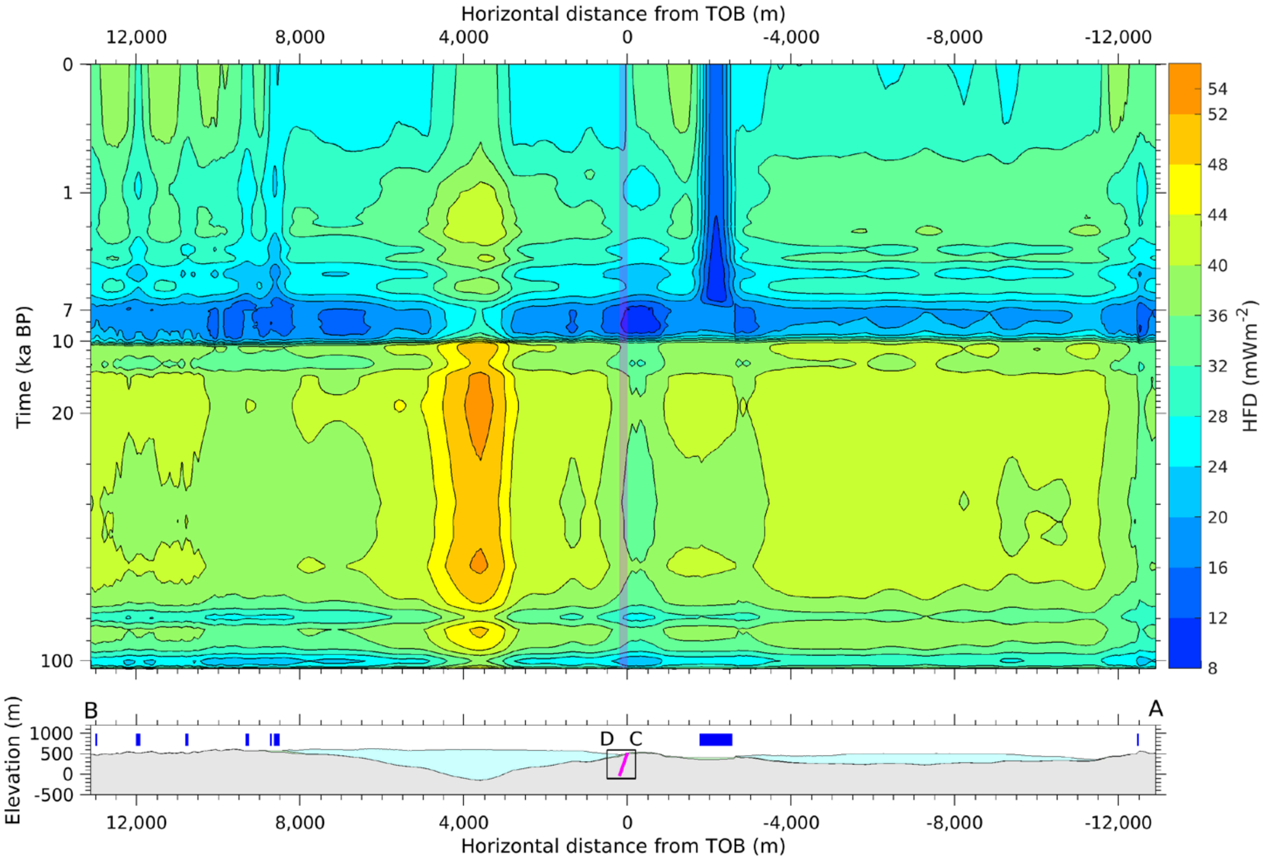

Figure A4-1. *Upper panel: glacial cycle vertical geothermal heat flow density along the model domain for the K_H_Gbh_500_Mean_S100 test case. Note the logarithmic scale on the y-axis. Lower panel: surface topography along the 2D model domain. The inclined >500 m deep DH-GAP04 borehole is shown in pink. Present-day lake locations are denoted by blue bars. Modified from Colgan et al. (2022).*

Input data files

Table A5-1 summarises the input data files described in the previous appendices, used for the permafrost simulations.

Table A5-1. Input data files used for the permafrost model simulations.

Section in previous appendices	Type of data	Name of data file
A2.2.1	Location and extent of water bodies GAP (soil map)	WGR_REG_LCLASS_2018-02-15/WGR_REG_LCLASS_2018-02-15.tif
A2.2.2	Topographic Wetness Index (TWI)	Twi_esri_ascii/twi_30m_withice.txt
A3.3.1	Surface elevation	ArcticDEM_AsterDEM_5m_22n/ArcticDEM_AsterDEM_5m_22n.tif
A3.2	Bedrock physical properties	Input_data_GAP_permafrost_modelling_GTK.xlsx
A3.2	Bedrock temperatures	Heat flow density.xlsx
A3.3.1	Soil types (soil map)	WGR_REG_LCLASS_2018-02-15 /WGR_REG_LCLASS_2018-02-15.tif
A3.3.2	Average soil thickness	WGR_REG_RDM_2018-02-15.tif

Arkitektkopia AB, Bromma, 2022

SKB is responsible for managing spent nuclear fuel and radioactive waste produced by the Swedish nuclear power plants such that man and the environment are protected in the near and distant future.

skb.se